

REPORT DOCUMENT PAGE			Form Approved OMB No. 0704-0188
<p>Public reporting burden for this collection of information is estimated to average 1 hour per response, including the time for reviewing instructions, searching existing data sources, gathering and maintaining the data needed, and completing and reviewing the collection of information. Send comments regarding this burden estimate or any other aspect of this collection of information, including suggestions for reducing this burden, to Washington Headquarters Services, Directorate for Information Operations and Reports, 1215 Jefferson Davis Highway, Suite 1204, Arlington, VA 22202-4302, and to the Office of Management and Budget, Paperwork Reduction Project (0704-0188), Washington, DC 20503.</p>			
1. AGENCY USE ONLY (Leave blank)	2. REPORT DATE	3. REPORT TYPE AND DATES COVERED	
	31 July 2000	Final Technical Report, 1 May 1998 – 30 Apr 2000	
4. TITLE AND SUBTITLE Nonlinear Optics and Nonlinear Dynamics in Semiconductor Lasers Subject to External Optical Injection		5. FUNDING NUMBERS DAAG55-98-C-0038	
6. AUTHOR(S) Dr. Thomas B. Simpson			
7. PERFORMING ORGANIZATION NAME(S) AND ADDRESS(ES) Jaycor, Inc. 9775 Towne Centre Drive San Diego, CA 92121		8. PERFORMING ORGANIZATION REPORT NUMBER J203-00-0083/3081	
9. SPONSORING/MONITORING AGENCY NAME(S) AND ADDRESS(ES) U.S. Army Research Office P.O. Box 12211 Research Triangle Park, NC 27709-2211		10. SPONSORING/MONITORING AGENCY REPORT NUMBER ARO37647-3-EL-SB2	
11. SUPPLEMENTARY NOTES The views, opinions and/or findings contained in this report are those of the author(s) and should not be construed as an official Department of the Army position, policy or decision, unless so designated by other documentation.			
12a. DISTRIBUTION/AVAILABILITY STATEMENT Approved for public release; distribution unlimited		12b. DISTRIBUTION CODE 20001124 024	
13. ABSTRACT (Maximum 200 words) This Phase II SBIR effort investigates novel output characteristics of semiconductor lasers that can be induced by external optical injection. Specific interest is in characteristics relevant to the control of microwave and millimeter-wave electronics through enhanced modulation characteristics, characterization of vertical-cavity surface-emitting laser (VCSEL) arrays, and analysis of chaotic dynamics that can be induced by optical injection. Under external optical injection, all semiconductor lasers tested, conventional edge-emitting Fabry-Perot laser diodes, VCSELs, and distributed feedback (DFB) laser diodes exhibited periodic oscillation of the optical power due to an instability in the coupling between the circulating optical field and the semiconductor gain medium. The instability could be locked to a microwave reference by simultaneously injecting a weak modulation current at the appropriate frequency, i.e., double locking to both microwave and optical references. Phase-locked operation with sub-Hz linewidth and -125 dBc/Hz residual phase noise was measured, values that compare favorably with other published reports. A compact configuration using relatively inexpensive optical components was demonstrated. All laser types could be accurately modeled using a lumped-element, coupled-equation model for the circulating optical field and free-carrier density. The model showed good agreement with a mapping of the types of nonlinear dynamics observed experimentally.			
14. SUBJECT TERMS: Chaos Injection Locking Laser Diodes			15. NUMBER OF PAGES
Numerical Integration of Stochastic Nonlinear Differential Equations			
Nonlinear Dynamics Optical Phase-Locked Loop RF Photonics			16. PRICE CODE
17. SECURITY CLASSIFICATION OR REPORT Unclassified	18. SECURITY CLASSIFICATION OF THIS PAGE Unclassified	19. SECURITY CLASSIFICATION OF ABSTRACT Unclassified	20. LIMITATION OF ABSTRACT Unclassified

DTIC QUALITY INSPECTED 4

SECURITY CLASSIFICATION OF THIS PAGE

CLASSIFIED BY:

DECLASSIFY ON:

SECURITY CLASSIFICATION OF THIS PAGE

ACKNOWLEDGEMENTS

This program has been influenced by the expertise of many individuals. First, we would like to thank Dr. Mitra Dutta of the Army Research Office. Her support and encouragement made this program possible.

Dr. Eva Strzelecka of Honeywell Technology Center, Dr. Wei Jian Sha of SDL, and Dr. James Foresi of MODE, Inc. were the principal points of contact with their respective organizations. All were very helpful with information and tips about the lasers produced by their organizations that were investigated in this program. Dr. Chad Noddings of New Century Consulting produced specialized mounting circuits for high-speed modulation of the laser arrays. Dr. George Simonis, Dr. Wayne Chang, and Dr. Jiang Liu of the Army Research Laboratory also produced specialized mounting circuits for the laser arrays that allowed us to perform the device characterization reported here. Dr. Liu also provided additional characterization data that was especially useful. The collaboration, support and encouragement of Dr. Simonis and his coworkers was very much appreciated.

The theoretical modeling and numerical calculations work benefited from discussions with Dr. Tom Gavrielides of the Air Force Research Laboratory, Prof. Bernd Krauskopf of the University of Bristol, and Mr. Sebastian Wieczorek and Prof. Daan Lenstra of the Vrije Universiteit of Amsterdam. Prof. Jia-ming Liu and his group at UCLA provided not only helpful comments in discussions, but also collaborated on some of the modeling work undertaken during the program.

At Jaycor, Mr. Frank Doft most ably assisted in the experimental work that formed the bulk of the program. Mr. Greg Niederhaus performed the specialized machining tasks to produce custom optical mounts described in this report. Ms. Susie Rettig was most helpful with the contractual details. The phase noise test measurements were performed at the suggestion of Dr. Steve Pappert of SPAWAR, and in collaboration with Prof. Paul Yu and Mr. Dongsoo Shin of UCSD.

Finally, I would like to thank my wife, Eve Kornfeld, for all of her sacrifices and encouragement that allowed me to concentrate on this work. This program has been a wonderful research opportunity for me, one for which I will always be grateful.

TABLE OF CONTENTS

	PAGE
ACKNOWLEDGEMENTS	iii
LIST OF FIGURES	v
LIST OF TABLES	ix
INTRODUCTION	1
MODEL OF THE INTERACTION	3
EXPERIMENTAL APPARATUS	14
SEMICONDUCTOR LASER CHARACTERIZATION	22
A. High-Speed, Edge-emitting, Fabry-Perot Laser Diodes	22
B. Micro-optical Devices VCSEL Arrays	30
C. Honeywell VCSEL Array	40
D. DFB Lasers	44
E. Characterization Summary	46
NONLINEAR DYNAMICS	47
A. High-Speed SDL Lasers	48
B. MODE VCSEL	54
C. Honeywell VCSEL	57
D. DFB Lasers	59
DOUBLE-LOCKED LASER OPERATION	73
A. SDL Lasers – Double-Locked Laser Implementation	73
B. SDL Lasers – Double-Locked Laser Low Frequency Phase Noise	88
C. SDL Lasers – Double-Locked Laser Modulation Characteristics	94
D. Honeywell and MODE VCSELs	104
E. DFB Lasers – Compact Double-Locked Laser Implementation	106
CONCLUSIONS	109
REFERENCES	112

LIST OF FIGURES

FIGURE		PAGE
1	Schematic of the key elements of the nonlinear interaction in a semiconductor laser under external optical injection.....	2
2	The optical spectra of the modulation sidebands produced by a weak modulation current.....	9
3	Plots of the regenerative amplification (a) and the four-wave mixing (b) spectra.....	9
4	The maximum ratio of the optical sidebands that are generated when a weak current modulation is imposed	10
5	Noise spectra from a single-mode semiconductor laser biased at 1.6 times the threshold for laser oscillation.....	13
6	Bifurcation diagram showing extrema of the field amplitude as a function of the normalized amplitude of the injected optical field. of the photodetected signal	13
7	A schematic of the experimental apparatus used for optical injection, optical probing, and current modulation.	15
8	Picture of the free-space configuration used to measure the characteristics of the edge-emitting Fabry-Perot laser diodes and the VCSELs.	16
9	Picture of the fiber-coupled apparatus us used to measure the characteristics of the DFB lasers.	17
10	Schematic of the basic experimental apparatus for the double-locked laser.	18
11	Schematic of the experimental apparatus used to measure the range of double-locked operation and the implementation of an optical phase-locked loop.....	19
12	Schematic of the configuration used for phase noise measurements.	20
13	Variant of the experimental apparatus used when simultaneous inputs from the microwave frequency synthesizer and the microwave network analyzer were applied to the slave laser.	21

14	Characterization of the parasitic losses of an SDL-5411-G1.	24
15	Picture of the adapter mount built for the high-speed laser	25
16	Measured detector signal of the output power from the high-speed SDL laser as a function of bias current.	25
17	Spectra of the amplitude (power) modulation due to a weak optical probe	27
18	Spectra of the regeneratively amplified sideband due to a weak optical probe at two different bias currents	27
19	Spectra of the amplitude (power) modulation due to a weak, sinusoidal current injected into the high-speed laser diode along with the dc bias current.	28
20	Comparison between the predicted and observed asymmetry of the sidebands in the optical spectra under current modulation.	29
21	Pictures of the wire bonds used to contact the 1 x 12 MODE VCSEL array.	30
22	Picture of the ceramic substrate designed by New Century Consulting.	31
23	Picture of the high-speed package for the VCSEL arrays.	31
24	Bias currents to the individual elements of the VCSEL array where the threshold for operation is achieved and where the laser exhibited multifrequency operation indicative of multimode output.	33
25	Wavelength of the optical output of the individual emitters of the VCSEL array at the threshold for laser operation and just before the laser exhibited multifrequency operation indicative of multimode output.	33
26	Bias currents to the individual emitters of the VCSEL array for operation at a wavelength of 850.04 nm	34
27	Output power, and corresponding pump parameter, of the individual emitters of the VCSEL array when biased to emit at 850.04 nm.....	34

28	Output power as a function of bias current for three different lasers in the array showing different threshold currents and power vs. current slopes.	35
29	Regenerative amplification spectra of VCSEL #9 at two different bias currents.	36
30	Regenerative amplification spectra of three different VCSELs	36
31	Relaxation resonance radial frequency, Ω_r , as a function of output power for the 12 VCSELs in the array.	38
32	Overall decay rate, γ_r , as a function of output power for the 12 VCSELs in the array.	38
33	Near field images of one of the MODE VCSELs as the current is increased.	39
34	Regenerative amplification spectra of three different elements of the Honeywell VCSEL array	41
35	Regenerative amplification spectra of one Honeywell VCSEL biased at 0.4 mA	42
36	Asymmetry of the sidebands, given as the ratio of the positive to negative offset sideband, of a Honeywell VCSEL	43
37	Output power of the Alcatel Model 1915 LMO DFB laser diode ...	44
38	Key frequencies measured from the spectra of the 1915 LMO as a function of the current level above threshold.	45
39	Mapping of the experimentally observed dynamic regions for a conventional edge-emitting semiconductor laser.	47
40	Spectra of the slave laser output and the regenerative amplification of a weak optical probe under various injection levels.	50
41	Spectra of the slave laser output under various injection levels.	51
42	Spectra of the slave laser under optical excitation at the free-running optical frequency with an injection level approximately 70x the Hopf bifurcation level.	52

43	Calculated results when the laser model is modified to include a weak side mode.	53
44	Spectra under strong optical injection.	55
45	Resonance frequency of the laser under optical injection as a function of injected optical power.	56
46	Size of the injection peak and the resonance peak as a function of injected optical power in the region of periodic dynamics above chaotic dynamics.	56
47	Optical spectra of the output of the Honeywell VCSEL under optical excitation at the free-running optical frequency.	58
48	Spectra with injection at the free-running optical frequency showing the transition from stable to limit cycle dynamics.	60
49	Spectra with injection at an offset of 2 GHz from the free-running optical frequency showing the transition from unlocked to limit cycle dynamics.	62
50	Spectra with injection at an offset of 2 GHz from the free-running optical frequency showing the transition from limit cycle to chaotic dynamics.	63
51	Spectra with injection at an offset of 2 GHz from the free-running optical frequency showing the transition from chaotic to limit cycle dynamics.	64
52	Spectra with injection at an offset of -6.1 GHz from the free-running optical frequency showing the transition to quasiperiodic dynamics.	66
53	Continuation of Figure 52, with injection at an offset of -6.1 GHz from the free-running optical frequency, showing the transition stable injection locking.	67
54	Mapping of the observed dynamics based on the experimentally measured spectra of the DFB laser under optical injection when biased at twice the threshold current.	68
55	Bifurcation diagrams showing extrema of the optical field as a function of the injection parameter using the experimentally measured values of the Alcatel DFB laser for the dynamic parameters.	70

56	Bifurcation diagrams showing extrema of the optical field as a function of the injection parameter using the experimentally measured values of the Alcatel DFB laser for the dynamic parameters	71
57	Bifurcation diagrams showing extrema of the optical field as a function of the injection parameter using the experimentally measured values of the Alcatel DFB laser for the dynamic parameters	72
58	Optical spectra of the slave laser diode measured with the scanning Fabry-Perot optical spectrum analyzer	74
59	Spectrum of the amplified photodetector signal for the laser under the same external optical injection that yielded the optical spectrum in Figure 58.	75
60	Tuning range of the locked modulation signal when the dc bias to the master laser is varied along with the frequency of the locking current modulation to the slave laser.	75
61	Optical spectra of the slave laser diode measured with the scanning Fabry-Perot optical spectrum analyzer	77
62	Shift of the resonance frequency offset as the incident optical power from the master laser is increased.	77
63	Locking characteristics of the laser under simultaneous external optical injection inducing limit-cycle dynamics and current modulation at 8 GHz.	78
64	Locking characteristics of the laser under simultaneous external optical injection inducing period-doubling dynamics and current modulation at 4.355 GHz.	79
65	Scans showing the region of double locked operation as the operating point of the slave laser is varied by changing the bias current for three different modulation current power levels.	80
66	Scans showing the region of double locked operation as the operating point of the slave laser is varied by changing the bias current for three different modulation current power levels.	81
67	Locking range as a function of the modulation power for modulation frequencies of 7.055 and 14.11 GHz.	82

68	Double-Locked laser characteristics near the Hopf bifurcation.	84
69	Sampling oscilloscope traces of the locked resonance signals from the two photodiodes.	86
70	Spectra of the double-locked resonance feature of slave laser #1. ...	86
71	Spectra of the double-locked resonance feature of slave lasers with weak optical feedback.	87
72	Measured signals used in the slow modulation experiments to determine the stability of the locked microwave resonance.	89
73	Fourier transforms of the low frequency modulation data.	90
74	Absolute phase noise of the HP 8673C that is used as the reference oscillator for the double-locked laser diode.	92
75	Phase noise of the photodetected signal of the optical output from the double locked laser diode.	92
76	Microwave spectrum of the photodetected signal in the frequency region near the microwave carrier frequency of 13.8 GHz.	93
77	Spectrum of an optically-induced resonance feature which is locked to an 8 GHz current modulation.	94
78	Optical spectra of the slave laser under optical injection and signal modulation.	96
79	Calibration curves used for the modulation spectrata.	97
80	Network analyzer measurement of the photodetected signal component at the modulation frequency for several different operating points.	99
81	Network Analyzer measurement of the photodetected signal component at the modulation frequency for several different operating points.....	99
82	Maximum measured temporal shift of the 14.01 GHz sub-carrier.	100
83	Network analyzer measurement of the phase of the photodetected signal component that is imposed on the sub-carrier and then demodulated at the mixer.	102

84	Network analyzer measurement of the amplitude of the photodetected signal component that is imposed on the sub-carrier and then demodulated at the mixer.	102
85	Phase of the received modulation signal, relative to the phase of the received signal when the laser is operated at the center of the locking range, at the two extrema of the locking range.	103
86	Microwave spectra of the Honeywell VCSEL, comparing the double-locked output with the free running output and the output under optical injection alone	104
87	Phase noise of the photodetected signal of the optical output from the double locked laser diode.	105
88	Microwave spectrum of the photodetected signal in the frequency region near the microwave carrier frequency	106
89	Compact demonstration package of the double locked laser using DFB lasers and miniature optical components available in the 1.55 μm spectral region.	107
90	Noise characteristics of the compact, double-locked DFB laser configuration.	108
91	Resonance frequency signal of the compact, double-locked DFB laser configuration.	108

LIST OF TABLES

	PAGE
1 Comparison of device dynamic parameters.	46

NONLINEAR OPTICS AND NONLINEAR DYNAMICS IN SEMICONDUCTOR LASERS SUBJECT TO EXTERNAL OPTICAL INJECTION

1. INTRODUCTION

This final report provides a detailed summary of the results achieved under the Phase II Small Business Innovation (SBIR) Research Contract DAAG-55-98-C-0038, Emitting Lasers, performed for the U.S. Army Research Office. This Phase II SBIR effort has as its goals the experimental demonstration and modeling of novel output characteristics of semiconductor lasers that can be induced by external optical injection. Specific interest is in characteristics that can be applied to the areas of optical control of radio frequency (RF), microwave, and millimeter-wave electronics, sometimes called RF Photonics. There is also specific interest in characterizing the dynamic properties of vertical-cavity surface-emitting lasers (VCSELs), a relatively new semiconductor laser cavity configuration that is well suited to fabrication in high density, two-dimensional arrays. Further, the chaotic dynamics that can be generated by appropriate external optical injection has possible applications in secure communications and efficient spectral utilization in communications through the control of chaotic dynamics in laser diodes under optical injection. This investigation builds upon previous work that demonstrated that the output characteristics of semiconductor lasers was quite sensitive to external optical injection and that the modulation bandwidth and noise characteristics of laser diodes could be simultaneously improved through the use of external optical injection.¹⁻³

Lasers made with a semiconductor gain medium are among the most important and widely used today. Their importance lies not only in their many applications, from telecommunications and data/information processing to environmental sensors and laser pumping, but also in their usefulness as a system for understanding the fundamental characteristics of lasers. The semiconductor laser is a stochastic, nonlinear system where quantitative comparisons can be made between experiment and theory. In particular, the response of semiconductor lasers to external optical signals has proven to be a very interesting test-bed to examine the nonlinear dynamics of an optical system. Figure 1 shows the key elements of the nonlinear interaction schematically. An injection current pumps energy into the semiconductor gain medium. While the details vary with the particular semiconductor material used in the laser, semiconductor lasers are formed with a p-n semiconductor junction as the gain medium and a mechanism/mechanisms for providing feedback of light generated in the gain medium. In a p-n junction, a forward bias causes the free electrons from donor atoms in the n-type material to migrate to the vacant electron states, holes, of acceptor atoms in the p-type material. The energy that is liberated in this process can be emitted as a photon. The gain medium has been configured to produce spatial confinement of the optical fields. It is bounded by reflectors that provide feedback. Above the threshold for oscillation, stimulated emission produces a coherent circulating optical field in the cavity. The field is coupled to external fields plus, directly and indirectly, a variety of optical and electronic noise sources.

It is well established that a variety of external perturbations, external optical feedback from a distant reflector, external optical injection from an optical source, and modulation of the pumping current, can cause the output of the laser to become unstable and yield oscillatory or

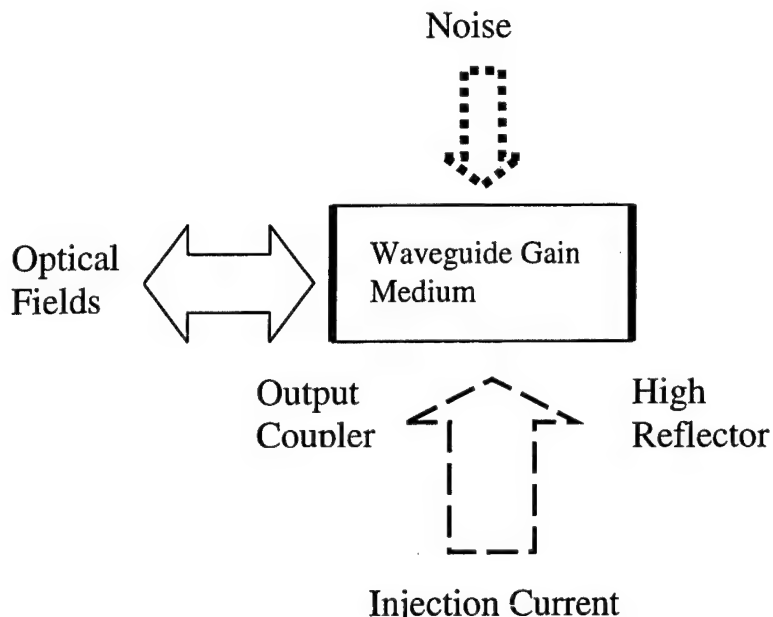


Figure 1. Schematic of the key elements of the nonlinear interaction in a semiconductor laser under external optical injection.

chaotic output.⁴ Of the three perturbation mechanisms, external optical injection allows the greatest degree of control and most direct access to the fundamental mechanisms that lead to the instability. With external feedback, one is limited to perturbing the laser with its own output and cannot control the optical characteristics of the external field. Current modulation can be limited by the fact that semiconductor lasers are circuit elements with inherent capacitance, inductance and resistance. Additional parasitic electronic effects arise when the gain medium is connected into an electronic circuit. The determination of the mechanisms controlling laser performance can involve a deconvolving of the circuit effects with the underlying processes within the laser cavity and gain medium. External optical injection allows one to perturb the laser with an independent optical field. The optical injection bypasses the electronic connections and yields direct information about the laser cavity and gain medium.

In this program, we have exploited the perturbing effects of an external optical field on a semiconductor laser to demonstrate a photonic frequency synthesizer that generates a tunable, high purity microwave-frequency modulation of the optical power.^{5,6} The synthesizer uses optical injection to destabilize the output characteristic of a semiconductor laser and produce a periodic modulation of the optical power. The depth of modulation and the modulation frequency can be controlled by adjusting the constant bias current to the laser. The oscillation of the optical power can then be locked to a microwave reference by adding a weak, near-resonant modulation current to the bias. Characteristics of this double-locked laser configuration, where the semiconductor laser is locked to both the optical injection and microwave current modulation, have been carefully measured. We have produced a laboratory apparatus to show that we can implement the photonic synthesizer in a compact optical package using relatively inexpensive, commercially available optical components.

The double-locked laser configuration has been implemented using all three types of semiconductor laser investigated, conventional edge-emitting Fabry-Perot cavity laser diodes, VCSELs, and distributed feedback (DFB) laser diodes. We have also used our optical techniques to characterize the dynamic parameters governing the modulation characteristics of these lasers. These techniques⁷ have been augmented by new procedures in this program. Our experimental results confirm theoretical predictions of the critical importance of the dependence of the refractive index, as well as the gain, on the free carrier density of the semiconductor laser gain medium. We have mapped the various dynamics displayed by the semiconductor lasers as a function of the amplitude and frequency detuning of the injection frequency.

This final report is organized as follows. Following this introductory section, we first describe the model of a nearly single-mode semiconductor laser subject to external optical injection and highlight a few new analytical results as well as some numerical results from computer implementations of the model. Next, the experimental apparatus is described. A section describing the characterization results on the different semiconductor laser systems investigated during this program follows this. This is followed by a section describing the nonlinear dynamics, including a new, more complete mapping of the dynamics observed. The next section summarizes the key findings of measurements of the lasers operated under external optical injection and current modulation, including noise and modulation characteristics. This section includes a description of an implementation of the double-locked laser in a compact configuration using relatively inexpensive, commercially available components, that was constructed to demonstrate the applicability of the beyond the laboratory. We conclude with a brief summary of key results.

2. MODEL OF THE INTERACTION

To model the system one can start with the wave equation within the optical cavity.

$$\frac{\partial^2 \vec{E}(\vec{r}, t)}{\partial t^2} + \frac{\sigma(\vec{r}, t)}{\epsilon(\vec{r}, t)} \frac{\partial \vec{E}(\vec{r}, t)}{\partial t} - \frac{1}{\mu_0 \epsilon(\vec{r}, t)} \nabla^2 \vec{E}(\vec{r}, t) = -\frac{1}{\epsilon(\vec{r}, t)} \frac{\partial^2 \vec{P}(\vec{r}, t)}{\partial t^2} \quad (1)$$

Here \vec{E} is the complex optical field at a point in the cavity, \vec{P} is the complex polarization in the medium induced by the field, ϵ is the nonresonant dielectric constant and σ is a phenomenological damping constant that describes the decay of the circulating fields due to distributed and output coupling loss mechanisms.

In the simplest description of the electron dynamics of the semiconductor laser, the electrons and holes are viewed as two homogeneously broadened ensembles that can be described via a two-band model, much like a two level model of an atomic resonance. The electron and hole populations of a forward-biased p-n junction are very high. Two key lifetimes describe the populations in the simplest picture. One lifetime describes the dephasing of the polarization of the medium and an applied optical field due to carrier-carrier collisions. This is a very short lifetime, typically sub-picosecond in duration. In the semiconductor lasers that will be discussed here, this lifetime is short compared to the other key time scales, except for the optical period. Due to this short lifetime, the polarization of the medium adiabatically follows the optical fields and can be modeled by the equation

$$\vec{P}(\vec{r}, t) = \frac{\epsilon}{\omega_0} g[N(\vec{r}, t), |\vec{E}(\vec{r}, t)|] \vec{E}(\vec{r}, t) \quad (2)$$

where g is the complex gain of the medium and is a function of the density of free carriers, N , and the amplitude of the circulating optical field. The second key lifetime of the electron and hole population describes the depopulation of the bands due to spontaneous emission and other relaxation processes. It is typically on the order of hundreds of picoseconds to nanoseconds.

There is a third lifetime that determines the dynamics of the optical output, the photon cavity lifetime. The fundamental linewidth of light emitted from a semiconductor laser is related to the gain, size of the gain medium, and photon escape rate from the cavity. Because semiconductor laser cavities are so small and the photon escape rate can be high, the semiconductor laser linewidth is often dominated by the fundamental spontaneous emission noise process. For the semiconductor lasers I will be describing the photon lifetime is typically on the order of a few picoseconds. The fact that semiconductor lasers can be readily operated in regimes where their basic output characteristics can be related back to basic physical parameters and noise sources makes them an especially attractive dynamic system for probing the details of nonlinear systems perturbed by both deterministic and stochastic sources.

The very different time scales of the problem allow several key simplifications to be made in the electromagnetic field equations and the material equations that describe the physics of the problem. First the period of the optical oscillation is sufficiently short that all other significant processes do not see significant change over an optical period. This allows us to make the rotating wave and slowly varying amplitude approximations that take the optical carrier out of the problem. Second, as already pointed out, the dephasing of the carriers with respect to the optical field is so fast that the polarizability of the medium adiabatically follows any imposed optical field amplitude. This simplifies the modeling of the relation between the free carrier density and the optical field. Further, because the free carriers are mobile, any standing waves due to counter-propagating optical fields are washed out over the length of an optical period. The circulating electric field can then be rewritten as, $\vec{E}(\vec{r}, t) \equiv A(t)\vec{u}(\vec{r}) \exp(-i\omega_0 t)$, with $A(t)$ being

the scalar field amplitude, $\left| \frac{\partial A}{\partial t} \right| \ll |\omega_0 A|$, and \vec{u} describing the spatial characteristics imposed by the waveguiding configuration. If we further restrict our interest to laser structures that can only oscillate in one spatial mode, and assume that spatial variations along the optical axis are small, we can make the lumped element approximation that takes the spatial coordinates out of the problem.

With these approximations, we are left with two equations that describe the interaction between the injected and circulating fields in a semiconductor laser and the gain medium of the laser. The basic set of coupled equations for the complex optical field, A , of the semiconductor laser that is oscillating at free-running optical frequency ω_0 , subject to an injected optical field, A_i , at optical frequency ω_i , and is coupled to a carrier density, N , can be written:

$$\frac{dA}{dt} = [-\gamma_c + i(\omega_0 - \omega_c)]A + \frac{\Gamma}{2} g(N, A)A + \eta A_i \exp[-i(\omega_i - \omega_0)t] \quad (3)$$

$$\frac{dN}{dt} = \frac{J}{ed} - \gamma_s N - \frac{2\epsilon_0 n^2}{\hbar\omega_0} \bar{g}(N, A) |A|^2 \quad (4)$$

$$\bar{g}(N, |A|) \equiv \text{Re}[g(N, |A|)] \quad (5)$$

Here, γ_c is the photon decay rate from the laser cavity, ω_c is the cold cavity resonance frequency, Γ is the confinement factor that relates the overlap of the oscillating mode with the gain medium, J/ed is carrier density injection rate due to the injection current density J , γ_s is the carrier spontaneous decay rate and $\epsilon_0 n^2$ is the nonresonant (real) dielectric constant of the semiconductor gain medium. The complex gain, $g(N, A)$, is assumed to vary about the free-running, steady-state operating point as a linear function of the carrier density and circulating intensity:

$$g(N, |A|) = (1 + ib) g(N_0, A_0) + (1 + ib) \left. \frac{\partial g}{\partial N} \right|_{N_0, A_0} (N - N_0) + (1 + ib') \left. \frac{\partial g}{\partial |A|^2} \right|_{N_0, A_0} (|A|^2 - A_0^2) \quad (6)$$

Here, b is the linewidth enhancement factor, the ratio of the imaginary to real parts of the complex gain due to carrier density changes, and b' is the ratio due to saturation effects. In a simple two-level system $b' = b$, and on resonance $b = 0$. However, the two-level model is, at best, an approximation for the two-band interaction of the semiconductor laser. Theoretical work has suggested that the two b parameters should be different.⁸ As we show below, two different parameters for the linewidth enhancement factor allow us to match details of our experiment with the model, details that cannot be otherwise readily accounted for. Therefore, this is a key modification to the model that we have previously used.³

Equations 5 and 6 can be recast in a convenient form, making use of some change of variables and introducing some useful parameters. Because our primary interest is in how external optical injection modifies the optical field, we use the steady-state, free-running condition of a semiconductor laser under dc bias above threshold as our starting point. The laser oscillates at an optical frequency ω_o with a steady-state field amplitude A_0 and a steady-state carrier density N_0 . The optical injection field, which has a field amplitude A_i and an optical frequency ω_i , is characterized by the frequency detuning $f = \Omega/2\pi = (\omega_i - \omega_o)/2\pi$ and the normalized dimensionless injection parameter $\xi = \eta|A_i|/\gamma_c|A_0|$, where η is the injection coupling rate and γ_c is the cavity decay rate of the injected laser. Direct current modulation with a modulation amplitude J_m at a modulation frequency $f_m = \Omega_m/2\pi$ is applied to the laser. Therefore, the total time-dependent current density injected to the laser is $J(t) = J_0(1 + m\cos(\Omega_m t))$, where $m = J_m/J_0$ is defined as the modulation index.

The modeling results presented here are obtained from analytical and numerical simulations using a generalized extension of a well established model of the laser that is formulated around experimentally determined laser parameters.⁷ By expressing the field amplitude and the carrier density of the injection-locked semiconductor laser as $A = A_0(1 + a)e^{i\phi}$ and $N = N_0(1 + \bar{n})$,

respectively, the characteristics of its modulation response can be numerically simulated using the following coupled equations:

$$\frac{da}{dt} = \frac{\gamma_c}{2} \left[\frac{\gamma_n}{\gamma_s \tilde{J}} \tilde{n} - \frac{\gamma_p}{\gamma_c} (2a + a^2) \right] (1+a) + \gamma_c \xi \cos[\Omega t + \phi(t)] + F_a \quad (7)$$

$$\frac{d\phi}{dt} = -\frac{b\gamma_c}{2} \left[\frac{\gamma_n}{\gamma_s \tilde{J}} \tilde{n} - \frac{b'}{b} \frac{\gamma_p}{\gamma_c} (2a + a^2) \right] - \frac{\gamma_c \xi}{1+a} \sin[\Omega t + \phi(t)] + \frac{F_\phi}{1+a} \quad (8)$$

$$\frac{d\tilde{n}}{dt} = -\gamma_s \tilde{J} \left\{ m \frac{\tilde{J}+1}{\tilde{J}} \cos(\Omega_m t) + \left[\frac{1}{\tilde{J}} + \frac{\gamma_n}{\gamma_s \tilde{J}} (1+a)^2 \right] \tilde{n} + \left[1 - \frac{\gamma_p}{\gamma_c} (1+a)^2 \right] (2a + a^2) \right\} \quad (9)$$

where γ_s is the spontaneous carrier relaxation rate, γ_n is the differential carrier relaxation rate, γ_p is the nonlinear carrier relaxation rate, and b is the linewidth enhancement factor. The parameter $\tilde{J} = (J/e d - \gamma_s N_o)/\gamma_s N_o$, where e is the electronic charge and d is the active layer thickness of the laser, is the differential injection current density above threshold, normalized to the threshold current density. It is often referred to as the pump parameter. F_a and F_ϕ are normalized, complex noise-source parameters related to the spontaneous emission rate R_{sp} of the laser.

$$\langle F_x(t) F_y^*(\tau) \rangle = \frac{R_{sp}}{A_0^2} \delta_{xy} \delta(t - \tau) \quad (10)$$

We have found that this model reproduces our key findings for laser diodes that operate in a single spatial and polarization mode. In some instances, however, the optical excitation and current modulation induced the laser to operate with a significant fraction of its output in a different mode. Details of these conditions will be given in the descriptions of the different lasers under study. However, in all cases, direct optical field coupling between the principal mode under excitation and the secondary mode that crossed threshold was not an important factor in determining the laser properties. In some instances, the secondary mode was considerably offset in frequency, in others it was of orthogonal polarization. Therefore, the secondary mode can be included by using the following first-order nonlinear stochastic differential equations:

$$\frac{da}{dt} = \frac{\gamma_c}{2} \left[\frac{\gamma_n}{\gamma_s \tilde{J}} \tilde{n} - \frac{\gamma_p}{\gamma_c} (2a + a^2 + w^2) \right] (1+a) + \gamma_c \xi \cos[\Omega t + \phi(t)] + F_a \quad (11)$$

$$\frac{d\phi}{dt} = -\frac{b\gamma_c}{2} \left[\frac{\gamma_n}{\gamma_s \tilde{J}} \tilde{n} - \frac{b'}{b} \frac{\gamma_p}{\gamma_c} (2a + a^2 + w^2) \right] - \frac{\gamma_c \xi}{1+a} \sin[\Omega t + \phi(t)] + \frac{F_\phi}{1+a} \quad (12)$$

$$\frac{d\tilde{n}}{dt} = -\gamma_s \tilde{J} \left\{ m \frac{\tilde{J}+1}{\tilde{J}} \cos(\Omega_m t) + \left[\frac{1}{\tilde{J}} + \frac{\gamma_n}{\gamma_s \tilde{J}} [(1+a)^2 + w^2] \right] \tilde{n} + \left[1 - \frac{\gamma_p}{\gamma_c} [(1+a)^2 + w^2] \right] (2a + a^2 + w^2) \right\} \quad (13)$$

$$\frac{dw}{dt} = \frac{\gamma_c}{2} \left[\frac{\gamma_n}{\gamma_s \tilde{J}} \tilde{n} - \frac{\gamma_p}{\gamma_c} (2a + a^2 + w^2) - \frac{\mu}{\gamma_c} \right] w + F_w \quad (14)$$

In equation 14 the side mode amplitude, w , is modeled with the additional parameters describing the gain defect of the secondary mode, μ , and the spontaneous emission noise source for the mode, F_w . This formulation assumes that the secondary mode is weak under free-running operation due to a small, relative to γ_c , reduction of the steady-state gain or loss rate. Further, the coupling between modes occurs because of the mutual dependence on the gain medium, without any significant coupling of the modal fields.

It is important to note that there are already a fair number of parameters to be determined. Since one of the key goals of this work is a quantitative, or at least, semi-quantitative comparison between modeling and experimental results, care must be taken to limit the number of model parameters that must be determined. Our approach to the model has been to keep it as simple as possible because we essentially use it for data fitting. Additional parameters that help to produce better agreement between experiment and theory are not necessarily justified. In the following sections, Equations 7-9 or 11-14 will be manipulated to highlight certain key features of the experimental observations. They form the basic model of the nonlinear interactions that occur in a semiconductor laser under simultaneous optical injection and current modulation.

Several important features emerge from a linearized analysis of the model equations. In this case, the optical injection is weak, causing only small deviations from the steady-state, free-running condition. The variables a, \tilde{n} , and ϕ are assumed to be and there will be no significant excitation of the a mode small because the external optical injection and/or modulation current are weak. The analysis for the case when $b = b'$ has been published elsewhere.¹ For the case when $b \neq b'$ there is a significant prediction for the optical sidebands generated by a sinusoidal modulation current. The equation for the modulation sidebands is:

$$\frac{|A_m|^2}{|A_0|^2} = \frac{\left\{ \left[1 + (b - b') \frac{\gamma_p}{\Omega} \right]^2 + b^2 \right\}}{\left(-\Omega^2 + \Omega_r^2 \right)^2 + \Omega^2 \gamma_r^2} \frac{\gamma_c^2 \gamma_n^2}{4} \frac{(\tilde{J} + 1)^2}{\tilde{J}^2} m^2 \quad (15)$$

where A_m is the field amplitude of the modulation sideband, Ω is the radial offset frequency, $\Omega_r^2 = \gamma_c \gamma_n + \gamma_s \gamma_p$ and $\gamma_r = \gamma_s + \gamma_n + \gamma_p$. Equation 15 gives the power ratio of the sideband to the central peak under weak injection as would be measured with an optical spectrum analyzer. The effects of $b \neq b'$ are contained in the term in the numerator that disappears when the two parameters are assumed to be equal.¹ Two key modifications to the modulation spectrum due to this term are an asymmetry in the sidebands, with the positively offset sidebands enhanced when $b > b'$, and an Ω^{-2} dependence to the modulation spectra near zero offset frequency. The unphysical divergence of the latter prediction is a consequence of the linearization of the coupled differential equations.

Expressions for the sidebands generated by weak optical injection are also modified when $b \neq b'$.

$$\frac{|A_r|^2}{|A_0|^2} = \frac{\left[-\Omega^2 + \frac{\Omega_r^2}{2} + b' \Omega \gamma_p \right]^2 + \left[\Omega \gamma_r - \frac{\Omega \gamma_p}{2} - \frac{b \Omega_r^2}{2} - \frac{(b'-b)(\gamma_r - \gamma_p)\gamma_p}{2} \right]^2}{(-\Omega^2 + \Omega_r^2)^2 + \Omega^2 \gamma_r^2} \frac{\gamma_c^2}{\Omega^2} \xi^2 \quad (16)$$

$$\frac{|A_f|^2}{|A_0|^2} = \frac{\left[-\Omega_r^2 + b' \Omega \gamma_p \right]^2 + \left[b \Omega_r^2 + \Omega \gamma_p + (b'-b)(\gamma_r - \gamma_p)\gamma_p \right]^2}{(-\Omega^2 + \Omega_r^2)^2 + \Omega^2 \gamma_r^2} \frac{\gamma_c^2}{4\Omega^2} \xi^2 \quad (17)$$

Here, A_r is the field amplitude of the regeneratively amplified signal at the injection frequency, and A_f is the field amplitude of the four-wave mixing signal at the optical frequency equally and oppositely offset from the laser optical frequency.

Figures 2 and 3 plot the predicted changes in the modulation spectra for the case of a conventional, edge-emitting Fabry-Perot laser diode that has been extensively characterized.⁷ In Figure 2, the spectrum due to a weak current modulation is plotted for the case with the old model, $b = b'$, and for the case when $b' = 0$. Also, shown is a curve plotting the ratio of the sideband to its oppositely shifted counterpart for the $b' = 0$ case. While the enhancement is limited to frequencies close to zero offset, the asymmetry is evident over a much broader spectral range. The regenerative amplification and four-wave mixing spectra for weak optical injection are plotted in Figure 3. There is very little difference between the two curves. In Equations 16 and 17 the terms that include b' are relatively small compared to other terms in the numerator, except at large offsets when the denominator grows rapidly and the signal becomes very weak. Therefore, the weak optical injection spectra are relatively insensitive to the value of b' . This explains why our previous investigations, which used weak optical injection to characterize the lasers, did not uncover the differing ratios for the real and imaginary parts of the differential gain and gain saturation terms.

When $b \neq b'$ the spectra predicted by Equation 15 has some very interesting characteristics for determining the parameters that underly the model. First, the ratio of sidebands at a given modulation frequency will be independent of any parasitic effects from the electronic circuit, as long as the small signal assumption holds. Therefore, we can use the modulation spectra to complement the optical injection spectra. Equation 15 has a very interesting feature in terms of determining the parameter b . It predicts that there will be a maximum in the sideband ratio, and that this maximum value will depend only on b . The specific offset frequency of the maximum will also depend on b' and γ_p . The linewidth enhancement factor, b , has been a difficult parameter to determine experimentally. The use of the optical spectrum produced by current modulation in the small signal regime provides a new, relatively simple technique for determining this key parameter. Figure 4 is a plot of the maximum sideband ratio as a function of the value of b . The figure shows that the sensitivity of the technique is improved as the value of b becomes smaller.

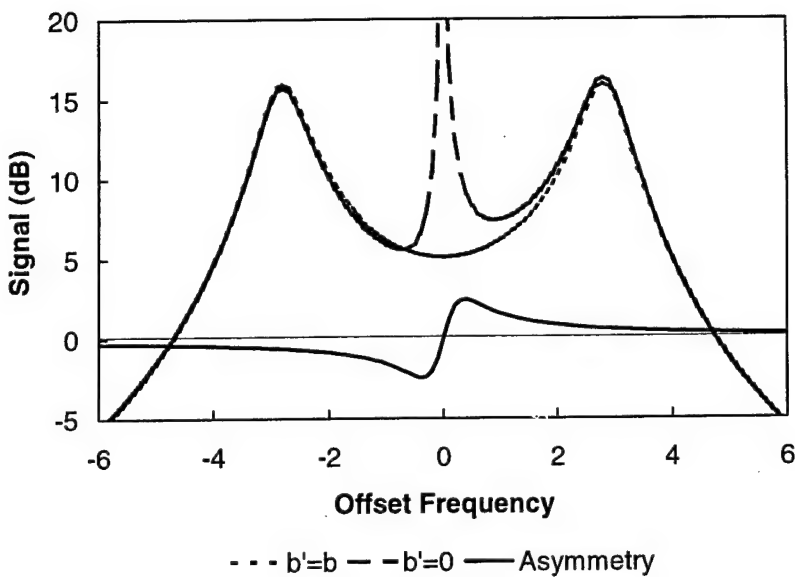


Figure 2. The optical spectra of the modulation sidebands produced by a weak modulation current. Shown are curves comparing the case when the ratio of imaginary to real parts of the gain saturation component is equal to the ratio for the differential gain (short dash) and is equal to zero (long dash). Also shown as a solid curve is a plot of the ratio of the sideband to its oppositely shifted counterpart for the $b' = 0$ case.

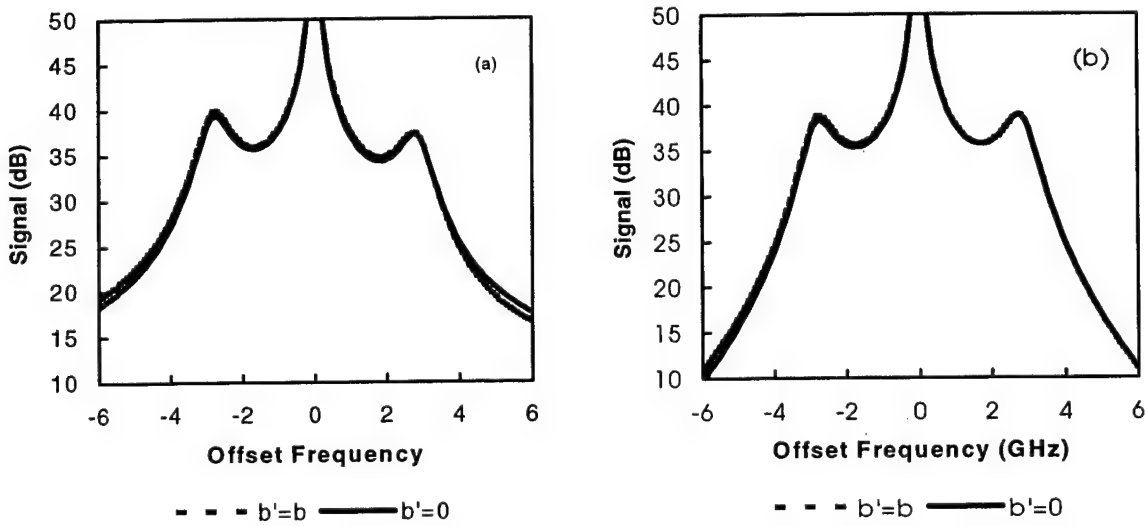


Figure 3. Plots of the regenerative amplification (a) and four-wave mixing (b) spectra comparing the case when the ratio of imaginary to real parts of the gain saturation component is equal to the ratio for the differential gain (dash) and is equal to zero (solid). The spectra are relatively insensitive to the value of b' .

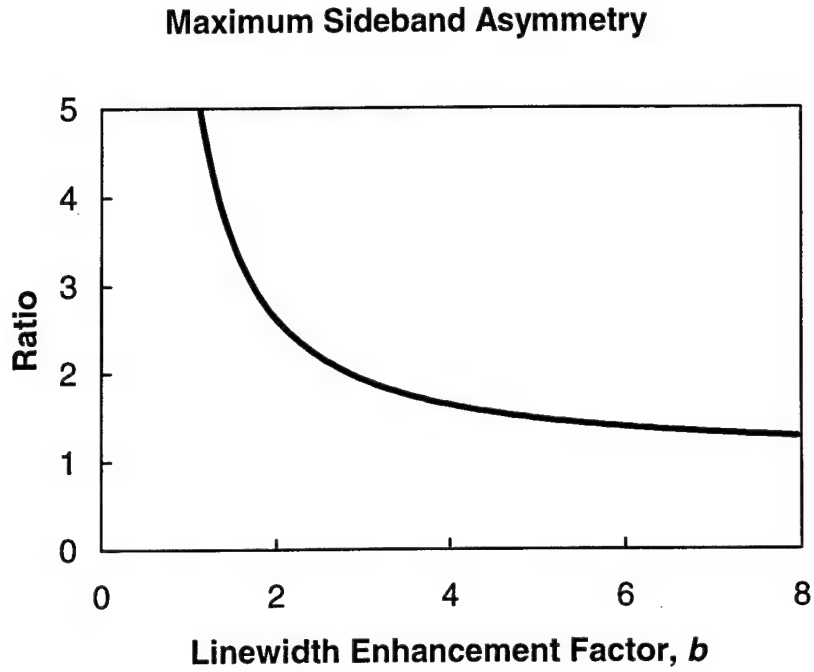


Figure 4. The maximum ratio of the optical sidebands that are generated when a weak current modulation is imposed on a semiconductor laser as a function of the linewidth enhancement factor. For $b > b'$, the plotted ratio is the positive frequency offset relative to the negative frequency offset, for $b < b'$ it is the reverse.

To produce numerical experiments using the full, nonlinear coupled equations, we recast the equations. Instead of using coupled equations based on the amplitude and phase of the optical field, we used the in-phase and quadrature components, $a_x + ia_y \equiv a \exp(i\phi)$. Further, because $\gamma_c \gg \gamma_s$ for most semiconductor lasers, we used the following change of variables to make the equations dimensionless and all of similar magnitude, $\tau \equiv \gamma_c t$, $\omega \equiv \Omega/\gamma_c$, $u \equiv \sqrt{\gamma_c/\gamma_s} \tilde{n}$, and $f_i = F_i/\gamma_c$. With these variable changes, the coupled equations can be recast as:

$$\frac{da_x}{d\tau} = \frac{1}{2} \left[\frac{\gamma_n/\gamma_c}{\sqrt{\gamma_s/\gamma_c} \tilde{J}} u (a_x + ba_y) - \frac{\gamma_p}{\gamma_c} (a_x^2 + a_y^2 + w^2 - 1) (a_x + b'a_y) \right] + \xi [\alpha_x \cos(\omega\tau) + \alpha_y \sin(\omega\tau)] + f_x \quad (18)$$

$$\frac{da_y}{d\tau} = \frac{1}{2} \left[\frac{\gamma_n/\gamma_c}{\sqrt{\gamma_s/\gamma_c} \tilde{J}} u (-ba_x + a_y) - \frac{\gamma_p}{\gamma_c} (a_x^2 + a_y^2 + w^2 - 1) (-b'a_x + a_y) \right] + \xi [-\alpha_x \cos(\omega\tau) + \alpha_y \sin(\omega\tau)] + f_y \quad (19)$$

$$\frac{du}{d\tau} = -\sqrt{\frac{\gamma_s}{\gamma_c}} \tilde{J} \left\{ m \frac{(\tilde{J}+1)}{\tilde{J}} \cos(\omega_m \tau) + \left[\frac{1}{\tilde{J}} \sqrt{\frac{\gamma_s}{\gamma_c}} + \frac{\gamma_n/\gamma_c}{\sqrt{\gamma_s/\gamma_c} \tilde{J}} (a_x^2 + a_y^2 + w^2) \right] u \right\} \\ + \left[1 - \frac{\gamma_p}{\gamma_c} (a_x^2 + a_y^2 + w^2) \right] (a_x^2 + a_y^2 + w^2 - 1) \quad (20)$$

$$\frac{dw}{d\tau} = \frac{1}{2} \left[\frac{\gamma_n/\gamma_c}{\sqrt{\gamma_s/\gamma_c} \tilde{J}} u - \frac{\gamma_p}{\gamma_c} (a_x^2 + a_y^2 + w^2 - 1) - \frac{\mu}{\gamma_c} \right] w + f_w \quad (21)$$

Computer programs were written to numerically integrate the four coupled nonlinear stochastic differential equations. The numerical integration of stochastic terms in the differential equations requires some care. Standard integration routines such as the 4th order Runge-Kutta are designed for equations which only contain deterministic terms.⁹ Much less work has been done on the integration of equations with stochastic terms. We have found three approaches. Most workers in the field do the following, for each time step they perform a 4th order Runge-Kutta integration for the deterministic terms and then a 1st order Euler-type step for the stochastic terms. A second procedure based on the standard 4th order Runge-Kutta formulation has also been identified. In this procedure the stochastic terms are multiplied by a scale factor, which turns out to be 3.6, and then included in the standard formulation.¹⁰ Like the first approach, this procedure is correct to first order in the step size. The third approach abandons the standard Runge-Kutta formulation, but is also based on a Taylor series expansion of the variables.¹¹ It is relatively easy to implement up to second order for both the deterministic and the stochastic terms. Therefore, the last approach is the most rigorously correct but it is the lowest order expansion for the deterministic terms.

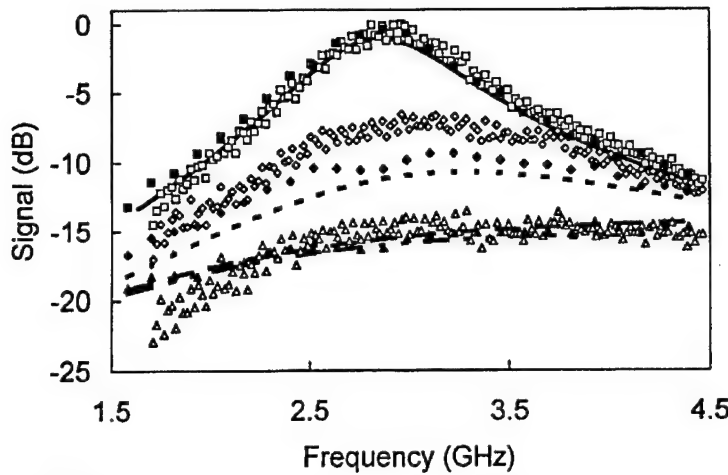
Fortran programs for all three approaches have been written. The current formulations use two real equations for the in-phase and quadrature components of the complex oscillating field. The change from amplitude and phase equations was made because of the stochastic terms. In the phase equation the stochastic term must be divided by a term containing the amplitude variable. This changes the noise from additive noise to multiplicative noise. Most likely this is not a critical change for our purposes. However, the 2nd order formulation has only been rigorously demonstrated for additive noise. Similarly, if noise terms are added to the carrier equation, they also would be multiplicative noise terms. Because our past work has indicated that carrier noise is not important, the carrier equation noise terms have been omitted.³ The equations do include provisions for external optical injection from a source containing noise and current modulation. We can readily include feedback to both the field equations and the carrier equation. The carrier equation feedback is proportional to the delayed optical power and represents either optical feedback which is not reinjected into the oscillating mode but which does modify the carrier density or an optoelectronic feedback of the signal from a photodetector that is added to the bias current. Such a term would be generated by an injection current signal from a photodetector that detects a fraction of the output beam.

Initial tests of the three different formulations compared output spectra for the optical field and optical power. All three formulations gave very similar results over most of the range of

operating parameters that were expected to be used in the program for a properly chosen time step. To achieve consistent results, the time step had to be $(8\gamma_c)^{-1}$, or somewhat shorter. Runs using double precision gave essentially the same results as those using single precision though, of course, specific details changed in the region of chaotic dynamics.

As a test of the routines, we examined some old data on the noise spectra of the laser diode. We had previously become aware that a published comparison¹² between theory and experiment was in error due to an incorrect accounting of the increase in optical power under external injection. The data and calculations are shown in Figure 5. Three different laser conditions are shown, free-running and at two different injection conditions. The experimental data is compared with several different calculations of the noise spectrum. First, the coupled equations were linearized and an analytical solution for the spectra was generated. Because the laser was operated under conditions where its output was stable, the linearized formulation was expected to be quite good. The full nonlinear equations were then numerically integrated with and without the noise from the master laser. Adding noise to the master laser did not appreciably change the calculated spectra, though there is a minor change visible in the highest injection level data. At other frequencies, the master laser noise does cause a significant difference. The agreement between the measured and calculated spectra is good and, as expected, the linearized model does a good job at this operating condition. All three numerical integration routines returned essentially the same spectra.

We also observed that the use of a model with $b \neq b'$ produced one consistent effect when we analyzed the time series generated by numerically integrating the full nonlinear coupled equations. The analysis of the time series was typically done using a bifurcation diagram. Here one parameter, such as the amplitude or the frequency offset of the injected optical signal, is varied. Local maxima and minima of a time series variable are plotted at each value of the parameter. Stable operation produces one value, periodic oscillation produces a small number of values for each maxima and minima in a period. Limit cycle or period-one dynamics yields one maxima and minima per cycle, period-two dynamics produces two maxima and minima, etc. Quasi-periodic or chaotic dynamics produces a complex distribution of values. Figure 6 shows two bifurcation diagrams, plotting the extrema of the normalized field amplitude values as a function of the strength of an external optical signal injected at the free-running oscillation frequency. The left diagram uses the new model, retaining the previous value for b , but setting $b' = 0$, while the right diagram uses the old model. The specific dynamic parameters used in this calculation apply to the MODE VCSELs studied during this program and will be described in detail later in this report. Clearly the dynamics are significantly different. Setting $b' = 0$ significantly reduces the stability of the system. The effect is strongest for intermediate values of the injection parameter and produces a wider range of injection values where unstable dynamics are observed.



REM-34678

Figure 5. Noise spectra from a single-mode semiconductor laser biased at 1.6 times the threshold for laser oscillation. Measured and calculated spectra are shown. The experimental data for the free-running laser (open squares) can be reduced under optical injection at an injection level of 0.06 (open diamonds) and 0.2 (open triangles) with a master laser offset in frequency so that the locked phase of the slave laser is approximately the same as the master laser. Numerical calculations with the full nonlinear equations yield the spectra shown by the filled squares, diamonds and triangles, respectively. Linearized calculations yield the solid line (free-running), dotted line (0.06), dot-dashed line (0.2 with no master laser noise) and dashed line (0.2 with master laser noise included).

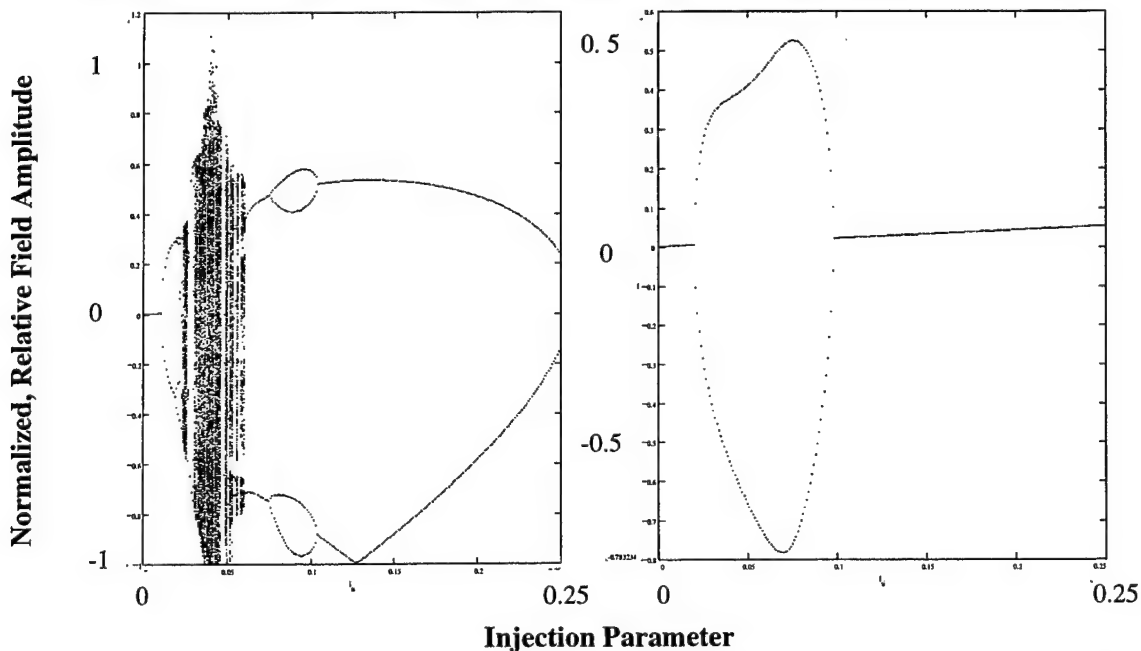


Figure 6. Bifurcation diagram showing extrema of the field amplitude as a function of the normalized amplitude of the injected optical field. The diagram on the left uses $b' = 0$ while the one on the right is calculated with $b' = b$. The laser parameters are appropriate for the high-speed laser operated at an injection current 5.6 times the threshold value.

3. Experimental Apparatus

The experimental characterization of the effects of optical injection on semiconductor laser dynamics is based on detailed observations of the spectral and, where possible, temporal characteristics. Our previous work has established that the predictions of the model described above yield very good agreement with experimental observations. Our procedure has several steps. First, we must determine the dynamic parameters: b , b' , γ_c , γ_s , γ_n , and γ_p , to compare model with experiment. This is done by probing the laser under study with weak optical injection, as described previously. We augment this with a weak current modulation to determine b' . The laser is then subject to strong optical injection to verify that the model predicts dynamic behavior in agreement with what is experimentally observed. Under strong optical injection we can map out the different types of nonlinear dynamics that is experimentally observed. In this program, we have been particularly interested in regimes of oscillatory dynamics where the periodic oscillation of the optical power can be locked to a microwave reference frequency. We have then characterized the noise and locking characteristics of the laser under simultaneous optical and microwave locking.

Figure 7 is a schematic of a free-space configuration for optical injection and optical probing. The configuration consists of three lasers. The master laser, LD1 with an optical frequency v_1 , is optically isolated from the rest of the configuration so that no feedback alters its output characteristics. Output from the master laser passes through a non-polarizing beamsplitter and is injected into slave laser, LD2 with an optical frequency v_0 . The injection is through the output coupler directly into the oscillating mode volume. The output from the slave laser is then partially reflected off of the beamsplitter and through a second optical isolator. This second isolator prevents feedback from the diagnostic optical elements. A third laser with an optical frequency that can be tuned over a range of a few 10s of GHz, labeled TLD with an optical frequency v_t , is used as a probe of the slave laser. The beam injected into LD2 from TLD is always kept sufficiently weak so that it will not modify the operating characteristics of the slave laser. If there is no signal from the master laser, the probe laser interrogates the free-running characteristics of the slave laser. Under optical injection of the slave laser by the master laser, the probe laser measures the output characteristics of the injection-modified system. The output from the TLD is passed through an acousto-optic modulator. Through Bragg scattering, the modulator produces a frequency-shifted replica of the probe laser output that becomes spatially separated from the main beam. This replica is injected into the slave laser while the main beam is passed to the optical detection apparatus where it can be used as a local oscillator. Optical output from the slave laser, LD1 and the probe laser, TLD, is detected by a scanning Fabry-Perot optical spectrum analyzer (OSA) and by a fast photodetector. The OSA is a semi-custom Newport Supercavity Model 240C with a free spectral range of approximately 2 THz and a finesse of greater than 20,000 over the 810-850 nm spectral range. The fast photodetector is a Newport Model D-30 with a bandwidth of approximately 15 GHz (-3 dB voltage point).

All lasers are temperature stabilized and biased with low noise current supplies. Temperature and current tuning are used to bring the laser optical frequencies to near resonance. Tuning of the probe laser is accomplished either by modulating the bias to the laser or, if the TLD is an external cavity laser diode, by applying a modulation voltage to piezo-electric element that controls the pointing of the cavity end mirror. Because of an intracavity grating, a change in the

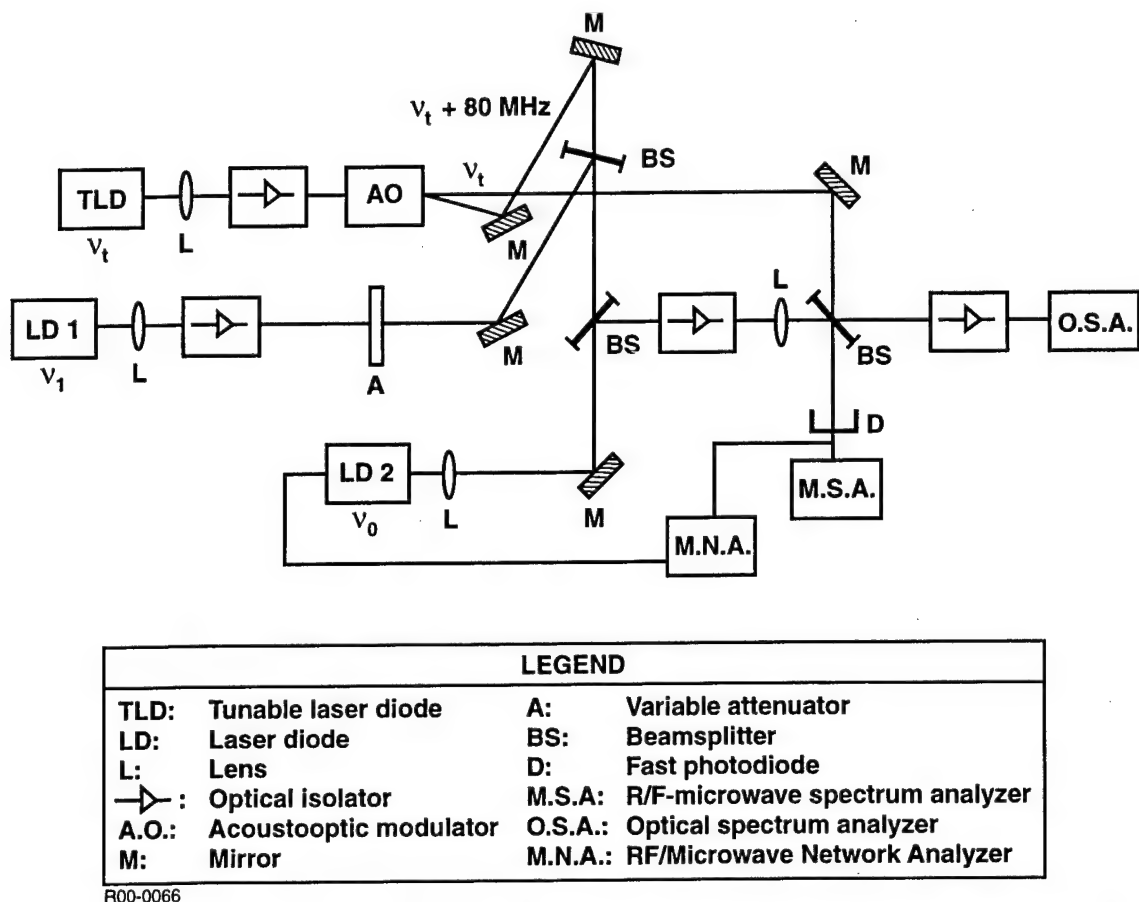


Figure 7. A schematic of the experimental apparatus used for optical injection, optical probing, and current modulation.

pointing of the end mirror causes a change in the optical frequency. A slow, on the order of 1 Hz, triangle modulation is used to generate the TLD frequency sweep. The output from the fast photodiode is amplified by low-noise, high-bandwidth microwave amplifiers and then detected by a microwave spectrum analyzer, a Tektronix Model 492P. When the TLD is being used as a local oscillator, the frequency setting of the microwave spectrum analyzer is set to the offset frequency of the acousto-optic modulator, 80 MHz, to produce a regenerative amplification spectrum of the probe laser as it is scanned in frequency. It can be set to some other appropriate frequency and, when the probe beam to the slave laser is blocked, used strictly as a local oscillator for measuring the optical spectrum of the slave laser. We have found that this combination is actually more sensitive than the OSA. However, the optical spectrum analyzer provides an excellent picture of the optical spectrum for real-time monitoring. In Figure 6, the output from the photodetector is also being measured with a microwave network analyzer, a Hewlett Packard (HP) Model 8753. The network analyzer simultaneously applies a modulation current to the slave laser. Measurement of the optical sidebands produced by the current modulation generates the data for determination of the ratio of b' to b .

With the configuration shown in Figure 7, we can measure the optical and power spectra of the free-running and injection-modified system, the regenerative amplification spectra of a weak

optical probe interrogating the free-running and injection-modified systems, and the current and optical amplitude modulation spectra of the free-running system. This configuration has been implemented in both a free-space format, for use with lasers operating in the near-infrared spectral region in the 800-860 nm range. Measurements on conventional, edge-emitting Fabry-Perot laser diodes and VCSELs were made with the free space apparatus. A picture of the free-space apparatus is shown in Figure 8. We constructed Plexiglas housings to place around the various laser mounts and collimating lenses to isolate the lasers as much as possible from air currents and temperature changes in the room and reduced fluctuations. To accommodate the various apertures and focusing requirements of the optics in the apparatus, the unit occupies approximately 10 square feet on an optical table. A fiber-coupled apparatus with all of the same functions, except the optical spectrum analyzer, has been implemented in the 1550 nm spectral region. The DFB lasers investigated in this program were studied in the fiber-based configuration. A picture of the apparatus is shown in Figure 9. It occupies less than half of the area as the free-space configuration.

Master, tunable probe, and slave lasers and collimating optics in clear plastic enclosure.

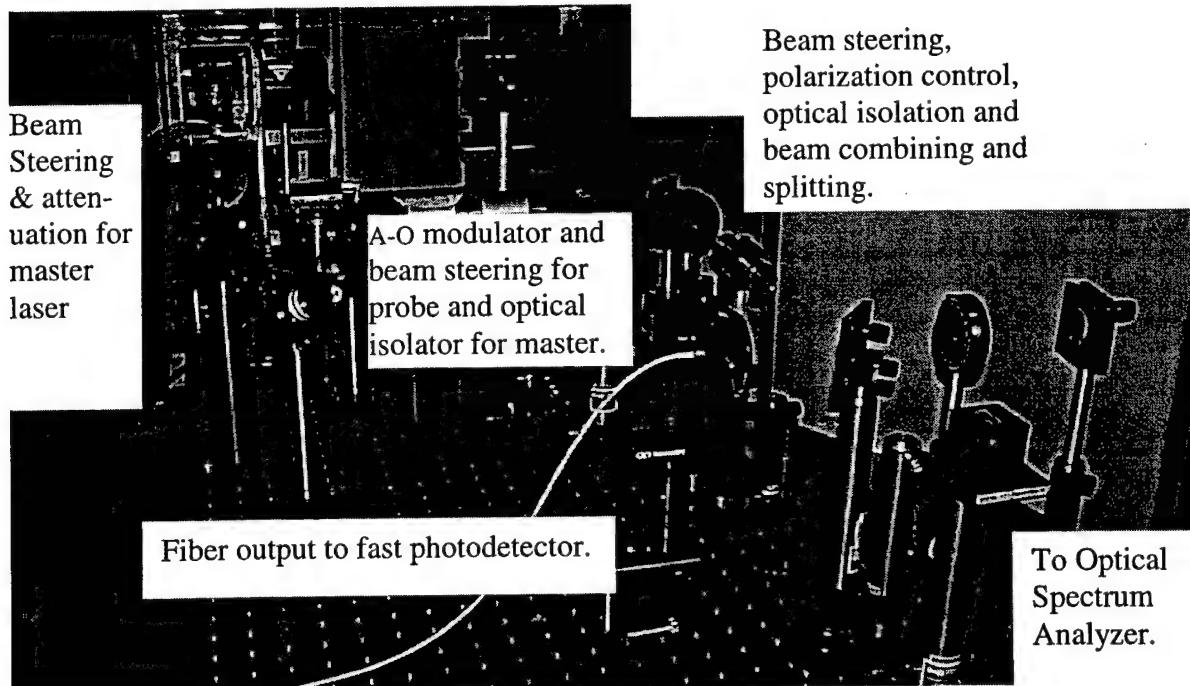


Figure 8. Picture of the free-space configuration used to measure the characteristics of the edge-emitting Fabry-Perot laser diodes and the VCSELs. For scale, the holes on the optical table are on one inch centers.

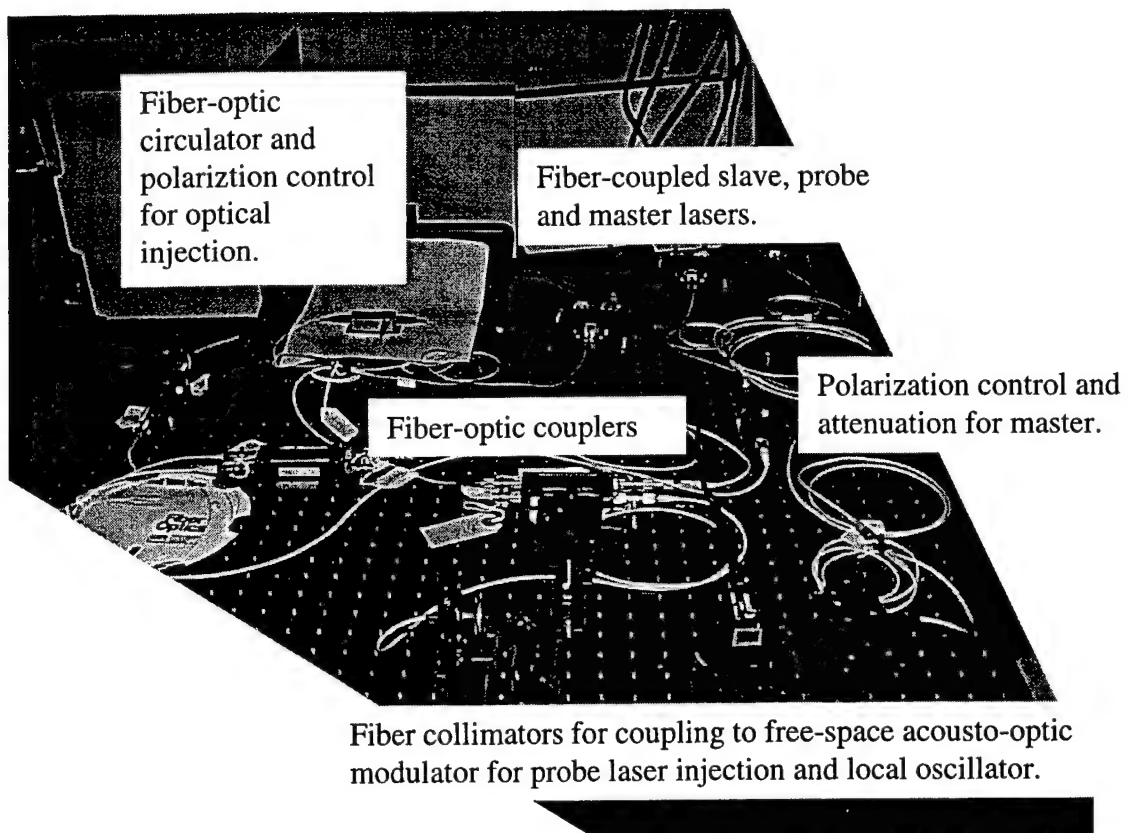


Figure 9. Picture of the fiber-coupled apparatus us used to measure the characteristics of the DFB lasers. For scale, the holes in the optical table are on one inch centers.

The layout for the optical characterization measurements is fairly complicated. To perform the double locking measurements, a simpler configuration could be used. However, the control electronics became more complex. Figure 10 is a schematic of the basic configuration used to simultaneously lock a laser to both optical and microwave laser sources, and measure the resulting output. The double-locked laser is a two-laser configuration, with an optically isolated master injecting a slave laser under independent current control. Coupling of the output from the master to the slave, and then the output of the slave to the diagnostics, is similar to the configuration shown in Figure 7. The slave laser is simultaneously biased with a dc current source and a microwave frequency source, an HP 8673C. The two are coupled to the laser through a broadband bias-T. This basic configuration is augmented as various tests are made on the double-locked laser. Phase locking is achieved and the locking range is established using the added electronics shown schematically in Figure 11. The basic configuration of Figure 10 remains intact.

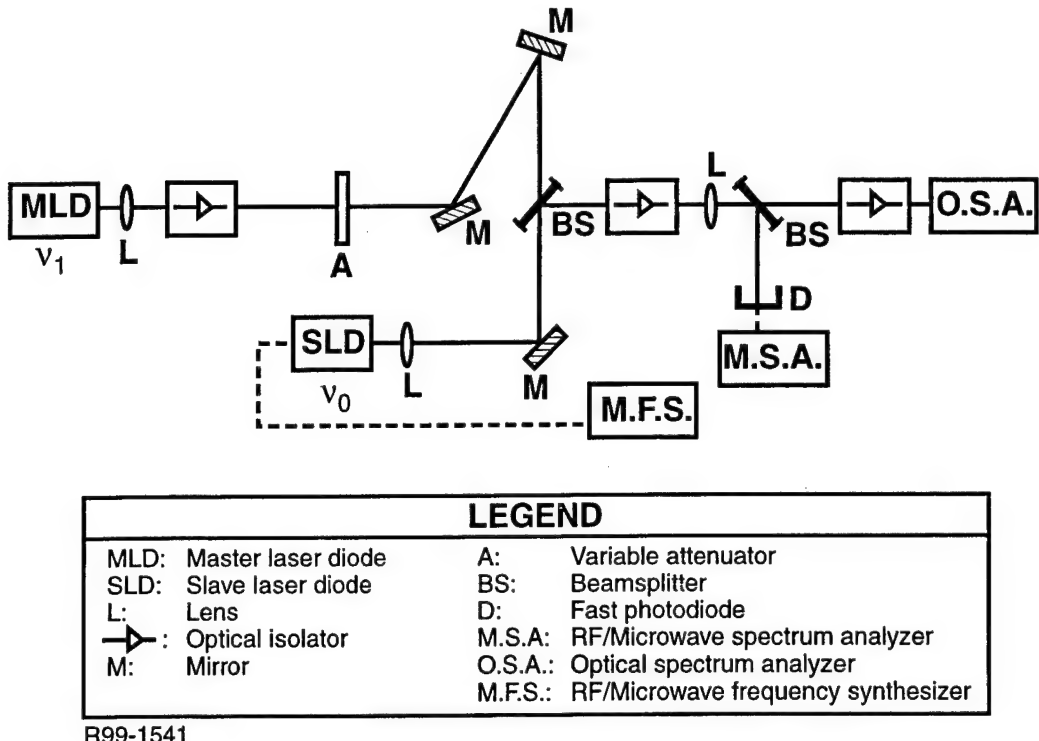
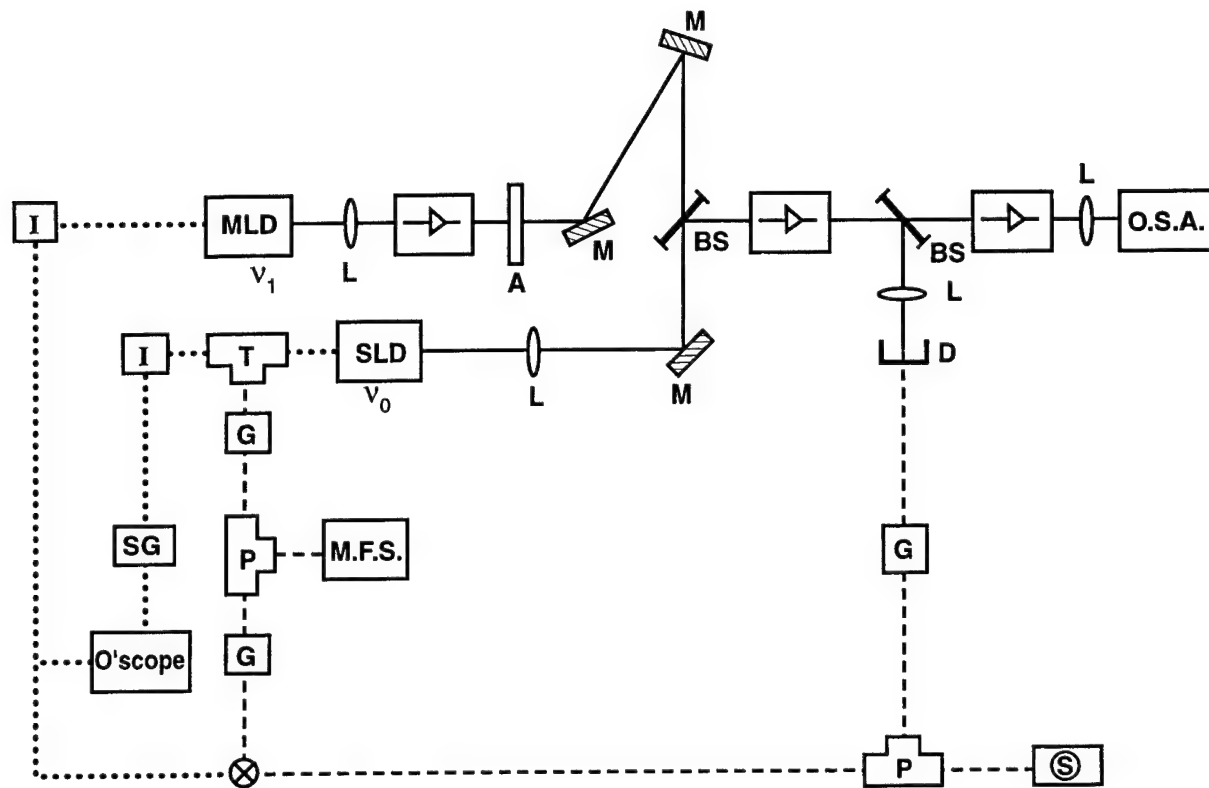


Figure 10. Schematic of the basic experimental apparatus for the double-locked laser.

Figure 11 explicitly shows the dc current sources used to bias the lasers and the microwave gain elements. Part of the amplified signal from the photodetector is sent to a microwave mixer where it is compared with the output of the frequency synthesizer. The resulting intermediate frequency (IF) error signal is a measure of the phase noise between the photodetected signal and the microwave frequency synthesizer when the slave laser is in the double locked configuration. It can be routed back to either the master, shown here, or slave current sources. These sources contain a modulation with a bandwidth of approximately 1 kHz. This feedback completes an optical phase-locked loop (OPLL). The tracking capability of the OPLL can be measured by simultaneously applying a slow modulation to the laser not receiving the feedback, Figure 11 shows the slave laser, that sweeps the bias current through the locking range.

Additional electronics are added to the configuration shown in Figure 10 in order to perform absolute and residual phase noise measurements, as shown in Figure 12. Such measurements provide a figure of merit of significance for the application of optical technology to microwave systems. Here, additional power splitters are added to signals from the microwave frequency synthesizer and the photodiode to allow monitoring by a Hewlett-Packard phase noise test set. Approximately 55 dB of microwave gain follows the photodiode to provide sufficient signal to the phase noise input. In addition, Figure 12 shows the addition of a low frequency, high-gain preamplifier, Princeton Applied Research Model 171, which was used to provide improved response characteristics to the OPLL. The preamplifier has adjustable gain and low pass filters that provide some degree of signal optimization for the error signal that is output from the microwave mixer. Alternatively, the conditioned error signal could be applied to the slave laser instead of the master laser.



LEGEND

MLD: Master laser diode	A: Variable attenuator
SLD: Slave laser diode	BS: Beamsplitter
L: Lens	D: Fast photodiode
→: Optical isolator	O.S.A.: Optical spectrum analyzer
M: Mirror	O'scope: Oscilloscope
G: Microwave gain	I: Laser diode current controller
M.F.S.: Microwave frequency synthesizer	T: Bias-T
⊗: Microwave mixer	P: Power splitter
(S): RF/Microwave spectrum analyzer or sampling oscilloscope	SG: Signal Generator

R00-0038

Figure 11. Schematic of the experimental apparatus used to measure the range of double-locked operation and the implementation of an optical phase-locked loop.

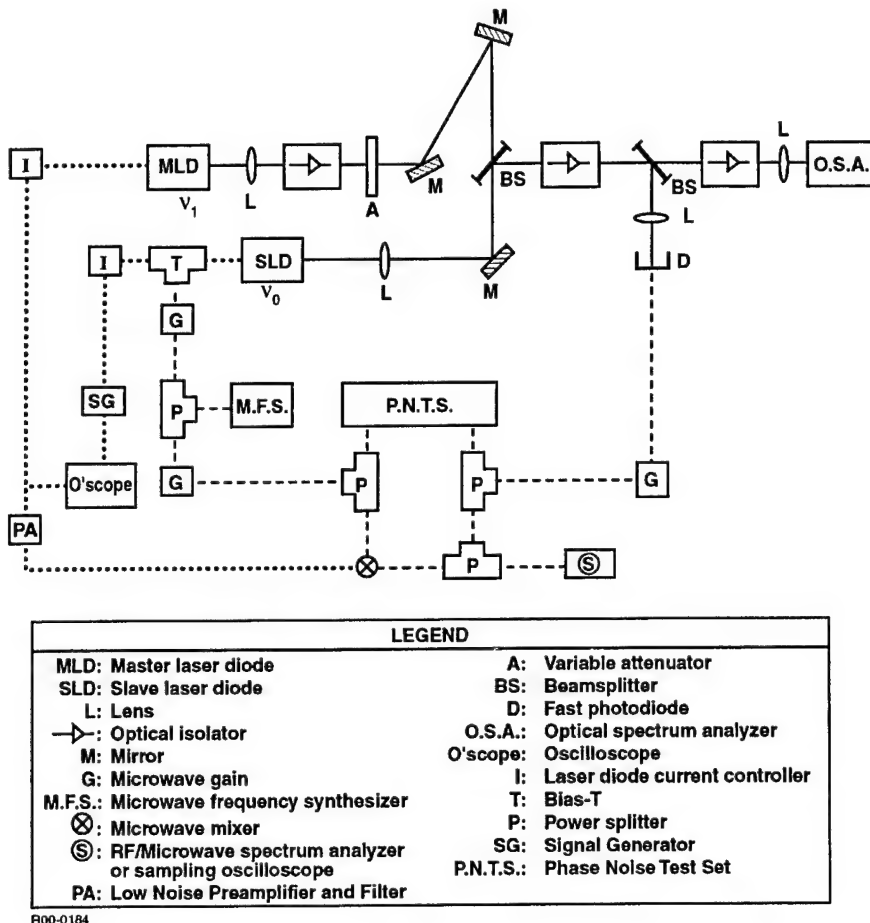
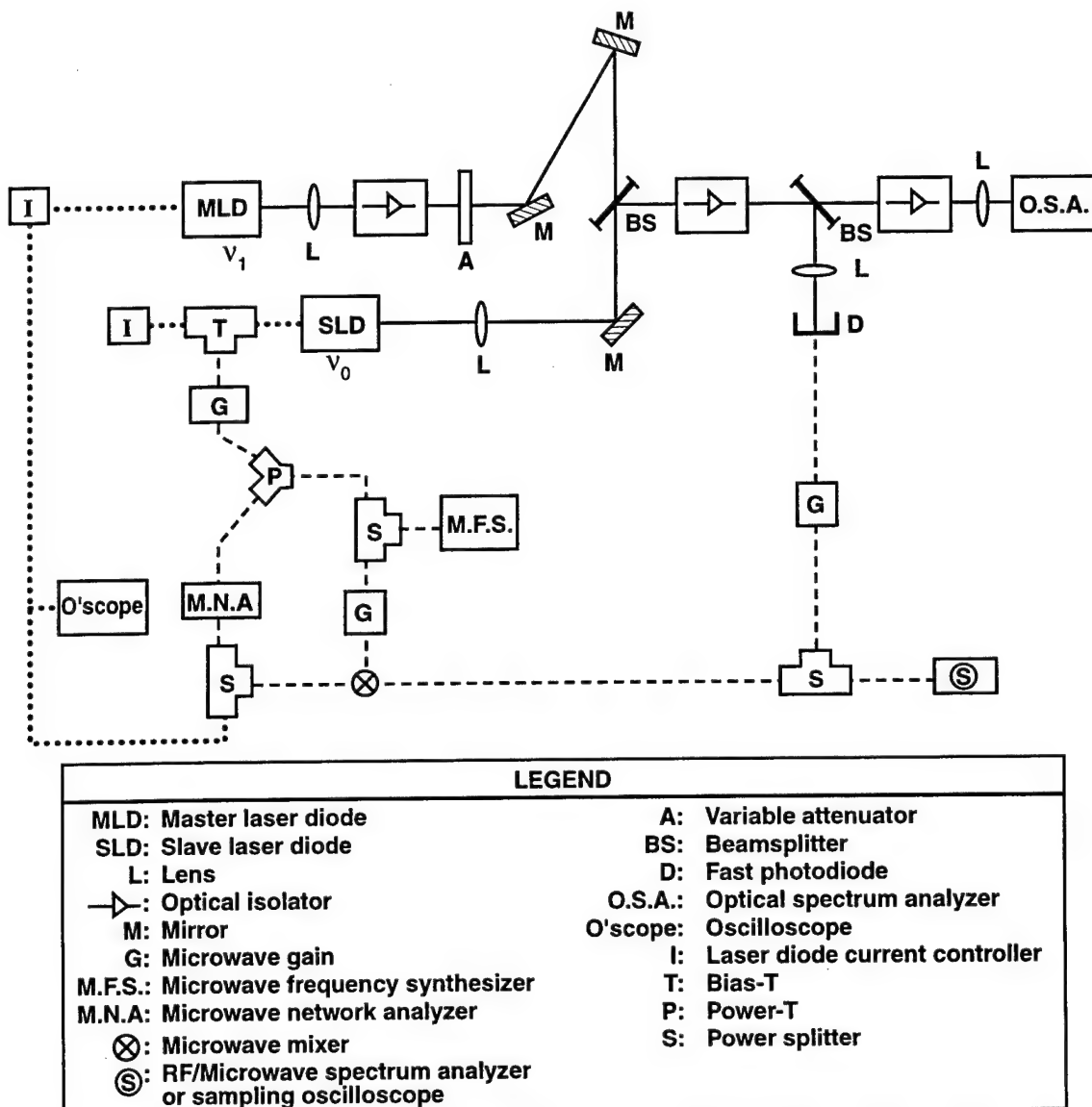


Figure 12. Schematic of the configuration used for phase noise measurements. Relative to the configuration shown in Figure 10, this configuration adds additional power splitters to provide signals to a phase noise test set. Also, the error signal generated at the microwave mixer is conditioned by a low-noise, high-gain preamplifier before being added to the bias of the master laser.

Another variant involved the use of the network analyzer in conjunction with the frequency synthesizer to determine the modulation characteristics of the double-locked laser. Figure 13 shows the configuration used when the modulation was applied to the slave laser. A microwave power-T is used to combine signals from the microwave frequency synthesizer and the microwave network analyzer before injecting into the slave laser. The frequency synthesizer continues to supply the reference signal that is used to lock the resonance of the optical injection induced instability. The microwave network analyzer supplies a weak, lower-frequency signal that is used to represent and information signal that is to be applied to the output. The microwave splitter following the frequency synthesizer supplied sufficient isolation to prevent signals from the network analyzer from corrupting the local oscillator signal to the microwave mixer. The



R00-0037
Figure 13. Variant of the experimental apparatus used when simultaneous inputs from the microwave frequency synthesizer and the microwave network analyzer were applied to the slave laser. The frequency synthesizer supplied the high frequency microwave modulation used as the reference for locking the double-locked laser and the network analyzer supplied a frequency tunable modulation used to represent an information signal.

combined signal is amplified before being added to the dc-bias current at the bias-T and being injected into the gain medium. This configuration could be readily altered so that that network analyzer signal could be combined with the dc-bias of the master laser in a bias-T to approximate a situation where the information signal is applied to the master laser. As we will discuss below, the response characteristics show significant differences based upon whether the network analyzer signal is applied to the master laser or to the slave laser.

4. SEMICONDUCTOR LASER CHARACTERIZATION

Three types of lasers were studied in this program. For historical reasons, the first type was a conventional, edge-emitting Fabry-Perot laser diode that was expected to have similar characteristics to semiconductor lasers that we had studied extensively in previous work.^{2,3,7} Relative to these older lasers, however, this laser had a longer laser cavity and a modified electrical packaging design.¹³ The former enabled the lasers to operate at higher single-mode power levels while the latter improved the electrical modulation characteristics of the device. Both differences were expected to improve capabilities in RF Photonics applications. We investigated two types of VCSELs. Both were expected to operate in a single spatial mode. One was based on an older device design that used ion implantation to provide confinement of the maximum gain region, while the second, experimental design used an oxide-confined structure. We also investigated a commercially available DFB laser that operated in the 1.55- μm spectral region. In the time between the inception and conclusion of this program, DFB lasers have seen solid performance improvement and significant cost reductions. Further, there has been significant reduction in the cost of fiberoptic components designed for the 1.55- μm spectral region. We were able to configure a fiber-coupled apparatus for the DFB lasers.

A. High-Speed, Edge-emitting, Fabry-Perot Laser Diodes

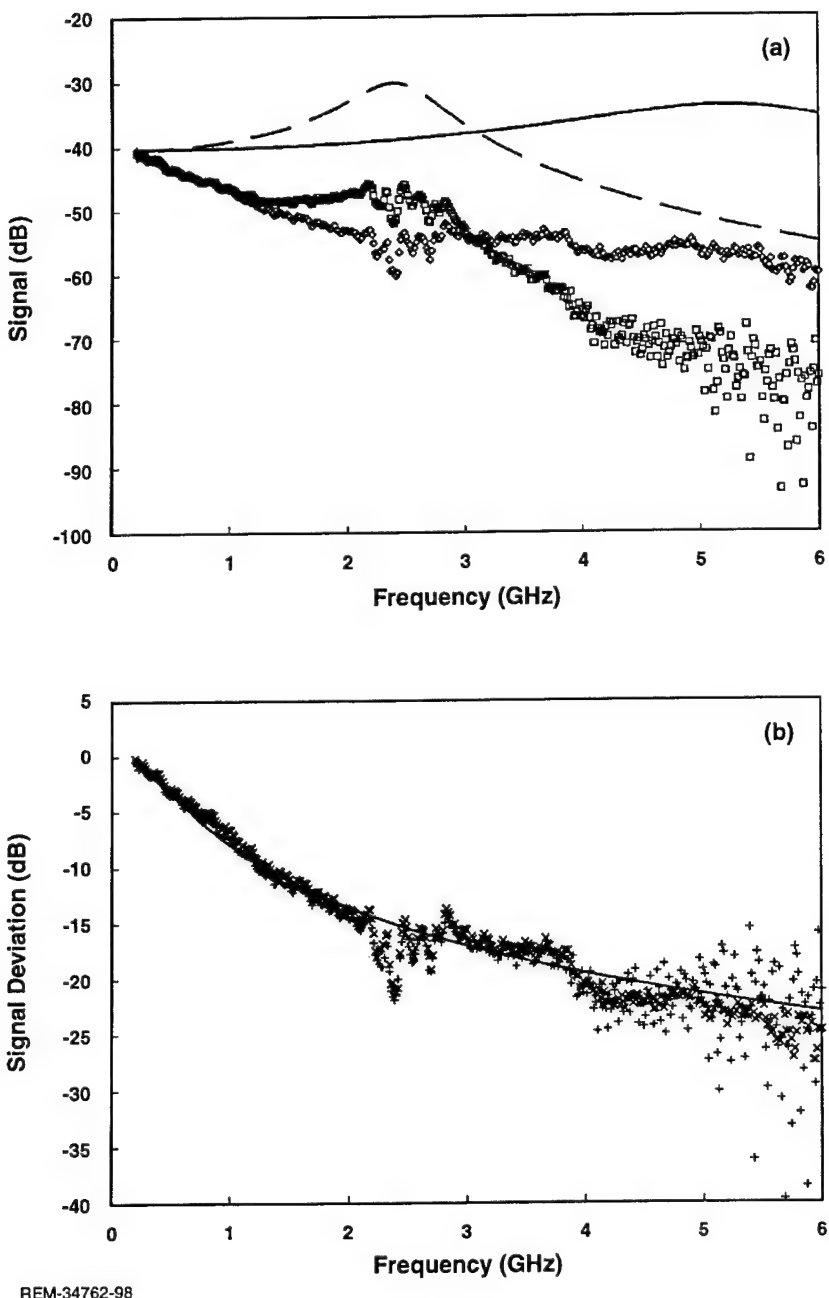
SDL, Inc., of San Jose, CA has been manufacturing the 5400 series, a line of high-power, single transverse mode, and nearly single longitudinal mode laser diodes for well over 10 years. We have been investigating the effects of optical injection on the operating characteristics of these lasers comparing experimental results with the predictions of the model outlined in Section 2. Extending our previous work^{1,7} on the characterization of laser diodes, we used the model to determine the parasitic losses in the laser diode electrical circuit used for the slave laser. This circuit included the packaged laser diode in a 9-mm transistor can as delivered by SDL. The 9-mm can was mounted in a 3-pin transistor socket that was directly soldered to the unterminated end of a short piece of semirigid coaxial cable. The opposite end of the cable had an SMA connector which was connected to a high-bandwidth bias-T. The dc input to the bias-T was connected to the bias current source for the laser diode and the RF input was connected to the output of an HP 8753 Network Analyzer through high-speed coaxial cable. We measured the modulation response characteristic of the laser diode by imposing a weak current modulation from the network analyzer and sweeping the frequency out to the maximum modulation frequency of 6 GHz. The input to the network analyzer is the output from the high-speed photodiode. The measured characteristic was compared to the model generated intrinsic characteristic of the laser diode. The difference between the model characteristic and the measured characteristic gives the frequency dependence of the circuit parasitics. Figure 14(a) compares the calculated intrinsic current modulation characteristic with the measured characteristic at two different bias currents. In Figure 14(b), the differences between the calculated and observed characteristics are plotted for the two current levels. It can be observed that the logarithmic differences between the calculated and measured characteristics are essentially the same for the two currents. This difference reflects the effects of the circuit parasitics. The dominant feature

is the rolloff in the modulation response due to the circuit parasitics. The measured rolloff is compared with a simple low-pass filter response in Figure 14(b). The 3-dB point of the filter is 380 MHz. Most likely, the laser package in the 9-mm can, the transistor socket and the connection to the semirigid coaxial cable are the dominant factors in determining this high-frequency rolloff. This test verifies that we will be able to determine the parasitic characteristics with our test procedure and, therefore, be able to separate the intrinsic current modulation response from the effects of parasitics in our high-speed tests.

Recently, a high-speed variant of the 5400 design has achieved modulation bandwidths in excess of 7 GHz.¹³ In this program we extensively studied these lasers. The laser chips are packaged on a 60-mil by 160-mil submount that must be mounted in a high-speed package for current modulation. SDL had previously used a packaging kit from Hewlett-Packard for high-speed measurements. Unfortunately, this kit is no longer available. We found that we had to design a mount from scratch. The mount had to allow high-speed modulation and, simultaneously, the removal of the excess heat generated by the 200-mW devices. It was determined that the most prudent method for achieving high-speed performance was to design an adapter mount that would allow the p-side contact of the submount to be directly connected to the center pin of an SMA panel mount connector. The n-side contact to be made through the mounting block. Conducting epoxy, as opposed to wire bonding, was used for the electrical contacts. Direct connection minimized the circuit lengths where 50-ohm transmission line performance was not achieved. Because the laser diode is not a 50-ohm device there is significant impedance mismatch. However, for the purposes of this program, this is acceptable, as we will be able to separate the electrical parasitic effects from the true laser cavity effects using our characterization techniques. The mounting block was gold-coated copper for good thermal and electrical conductance. The adapter mounts then fit into commercially available laser diode mounts with thermo-electric coolers for temperature stability.

Figure 15 is a picture of the adapter mount. On the front face of the mount there is a shelf with a small indentation in the center to hold the laser submount without interfering with the optical output. The SMA panel mount is connected to the adapter with two screws on the back face. The center conductor of the SMA passes through a hole in the mount to rest on top of the laser submount at the p-side metallization. The laser showed good power and wavelength stability up to the limit of its stated range of operation. Therefore, the mount displayed good thermal characteristics.

The typical output power of the series of six devices that we received from SDL is shown in Figure 16. Based on previous characterization by SDL, the output power at 200 mA is approximately 160 mW. The SDL devices under study are index guided and optical output is confined to a single transverse mode. However, multiple longitudinal modes can oscillate in the simple Fabry-Perot laser structure. Under free-running operation, we observed single-mode operation as the bias current was raised above 80-95 mA and operation without mode hops over a broad range of injection currents, typically above 130 mA - 140 mA. Following our standard procedure, the dynamic parameters of the slave laser were first determined from weak optical probing measurements.⁷ Based upon



REM-34762-98

Figure 14. Characterization of the parasitic losses of an SDL-5411-G1. In Fig. 5a the model-generated curves of the intrinsic current modulation characteristic are compared with experimentally measured data at two bias currents, 40 mA (dashed curve and square data points) and 115 mA (solid curve and diamond data points). In Fig. 5b, the difference between the logarithmic values of the measured and calculated modulation responses at 40 mA (+) and 115 mA (x) are compared with a simple low-pass filter curve with a 3-dB point of 380 MHz (solid curve). The scatter of the 40-mA data at high-modulation frequencies is due to the weak received signal by the network analyzer.

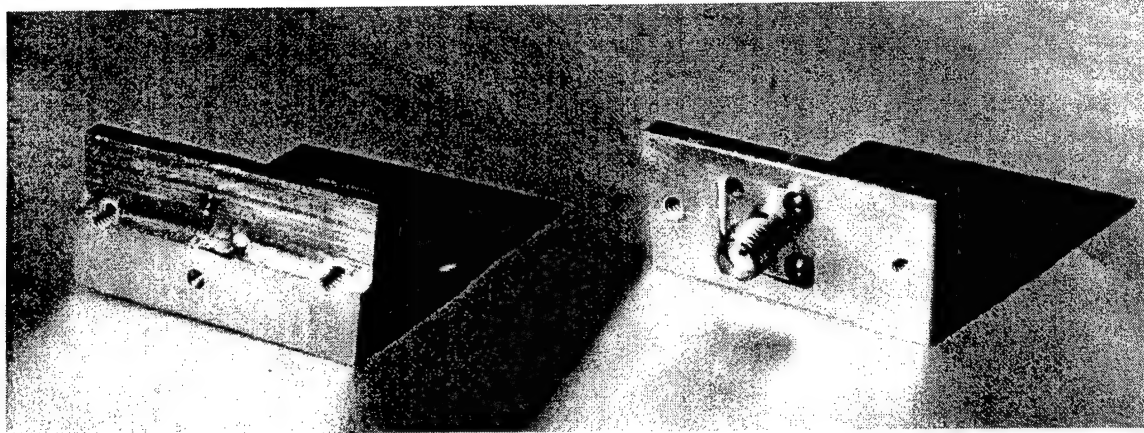


Figure 15. Picture of the adapter mount built for the high-speed laser, front face (left) and rear face (right). The laser submount is epoxied to a gold-coated copper block for good thermal conductivity. The n-side contact of the laser submount is also epoxied to the block for good electrical contact. An SMA panel mount is fastened to the block. The center pin of the SMA is directly epoxied to the p-side contact of the submount. The epoxy is a silver-filled two-part compound widely used for high-speed electrical contacts.

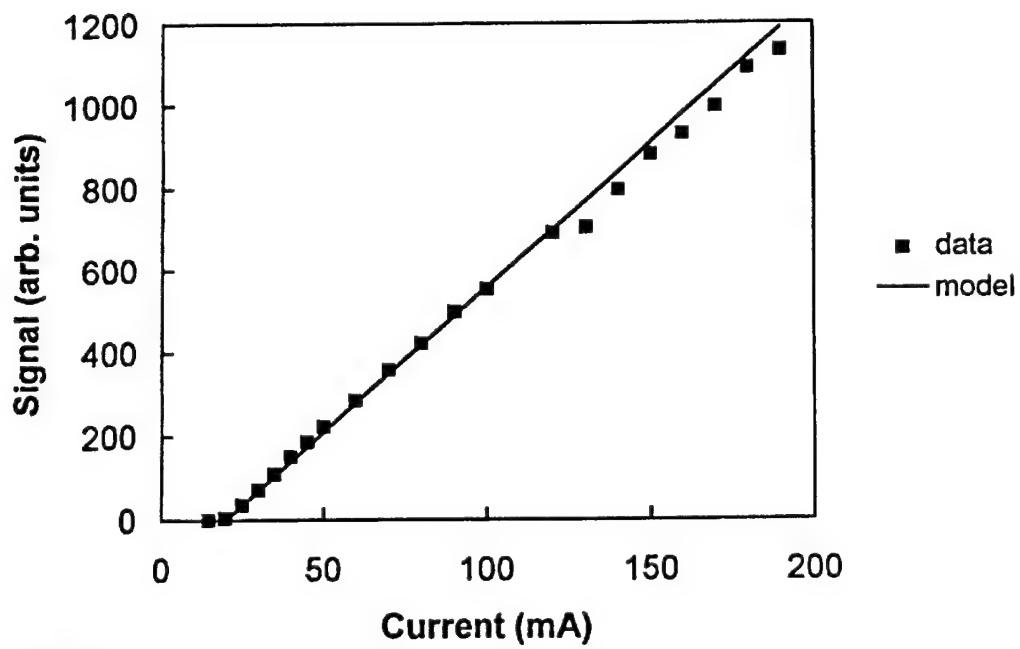


Figure 16. Measured detector signal of the output power from the high-speed SDL laser as a function of bias current. Model curve is for a linear slope.

a series of optical modulation measurements at different bias currents, the following parameters were generated:

1. Linewidth Enhancement Factor (b) = 5
2. Gain Saturation Ratio Factor (b') = 2
3. Cavity Photon Decay Rate (γ_c) = $2.5 \times 10^{11} \text{ s}^{-1}$
4. Carrier Spontaneous Decay Rate (γ_s) = $1.9 \times 10^9 \text{ s}^{-1}$
5. Differential Gain Relaxation Rate (γ_n) = $1.0 \tilde{J} \times 10^9 \text{ s}^{-1}$
6. Nonlinear Gain Relaxation Rate (γ_p) = $2.8 \tilde{J} \times 10^9 \text{ s}^{-1}$
7. Threshold current = 20 mA

In parameters 4 and 5 the symbol \tilde{J} refers to the pump parameter, the difference between the operating and threshold currents, normalized to the threshold current. These values are also quite similar to the lower speed device used for the measurement in Figure 14. Typical variations in the parameters across devices and the accuracy of the measurement are approximately $\pm 20\%$. The nonlinear gain relaxation rate grew consistently larger for devices with higher power ratings. These parameters produced a good fit to the experimentally measured data. In the data shown below, all measurements have been corrected for the frequency response of the measurement apparatus. Figure 17 shows representative amplitude modulation spectra and Figure 18 shows regenerative amplification spectra. The dynamic parameters listed above are determined from these two types of spectra. The model curves are generated from these parameters, except for the curve at 194 mA where deviations of $< 10\%$ were allowed to produce a better fit. These deviations are within the experimental error. Measurements of the optical spectra under strong optical injection will be described in the section on nonlinear dynamics.

These parameters also determine the expected modulation spectra due to a weak current modulation.¹ Like the standard SDL unit, the high-speed lasers showed a high-frequency rolloff due to the RC characteristics of the laser device. Figure 19 shows a comparison between model spectra and experimentally measured spectra that have had the effects of a simple low-pass filter with a 3-dB rolloff frequency of 3 GHz removed. The agreement is, in general, good though there is some deviation, consistent across the three operating currents, from 2 to 5 GHz. This represents an additional parasitic loss that is localized in frequency. The 3-GHz rolloff represents the combined effects of the laser chip resistance and capacitance and any additional effects due to the home-built high-speed mounts. The 3-GHz value is within the range of expected values based on previous tests by SDL, though somewhat lower than expected. The reduction of modulation voltages (currents) by a factor of 3 to 5 over the frequency range from 10 to 15 GHz is acceptable for both the small and large signal modulation tests conducted in this program.

The gain saturation ratio parameter, b' , cannot be readily determined from measurements based on injection of the laser by a weak optical probe. However, this parameter is responsible for asymmetry in the optical spectra of the laser under weak current modulation. In the determination of b' from the data, we fixed all of the dynamic parameters at the values determined from the optical modulation spectra, except for b and

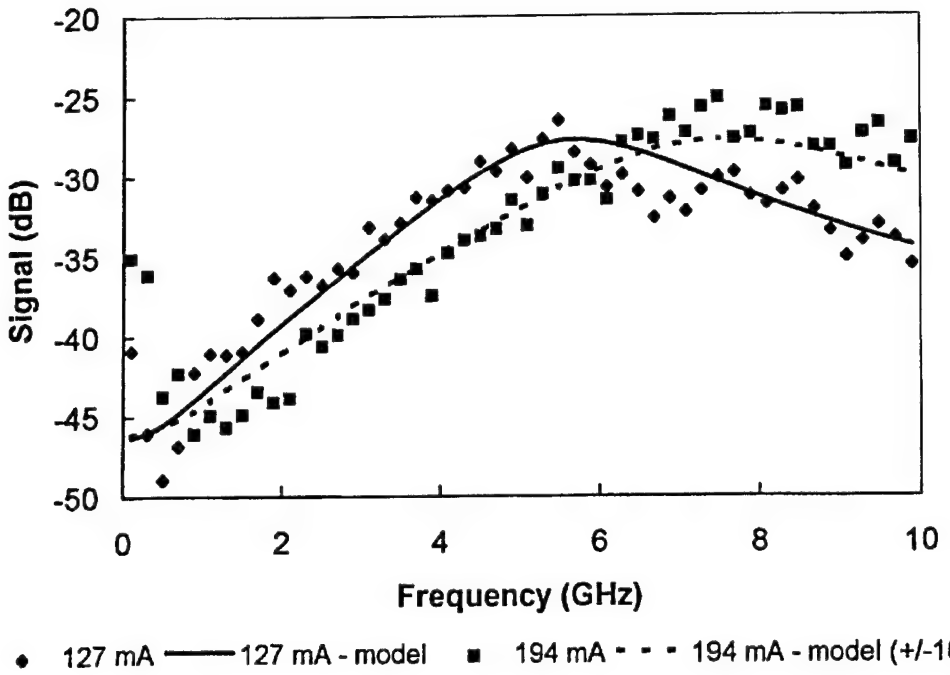


Figure 17. Spectra of the amplitude (power) modulation due to a weak optical probe at two different bias currents near the ends of the hop-free range of single-mode operation. The calculated (model) curve at 194 mA was made with some parameter adjustment, < 10% of the values listed in the text, to produce a better fit.

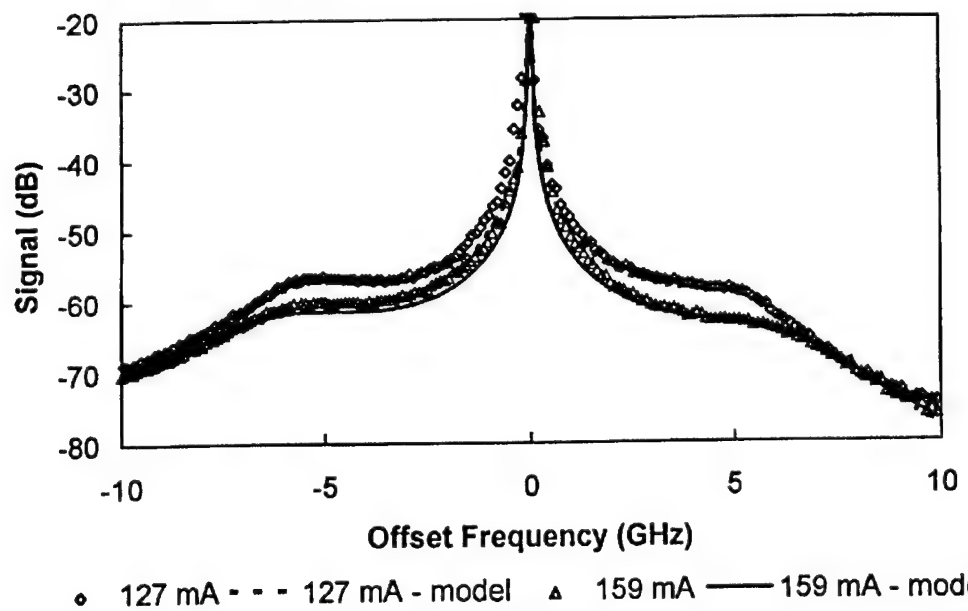
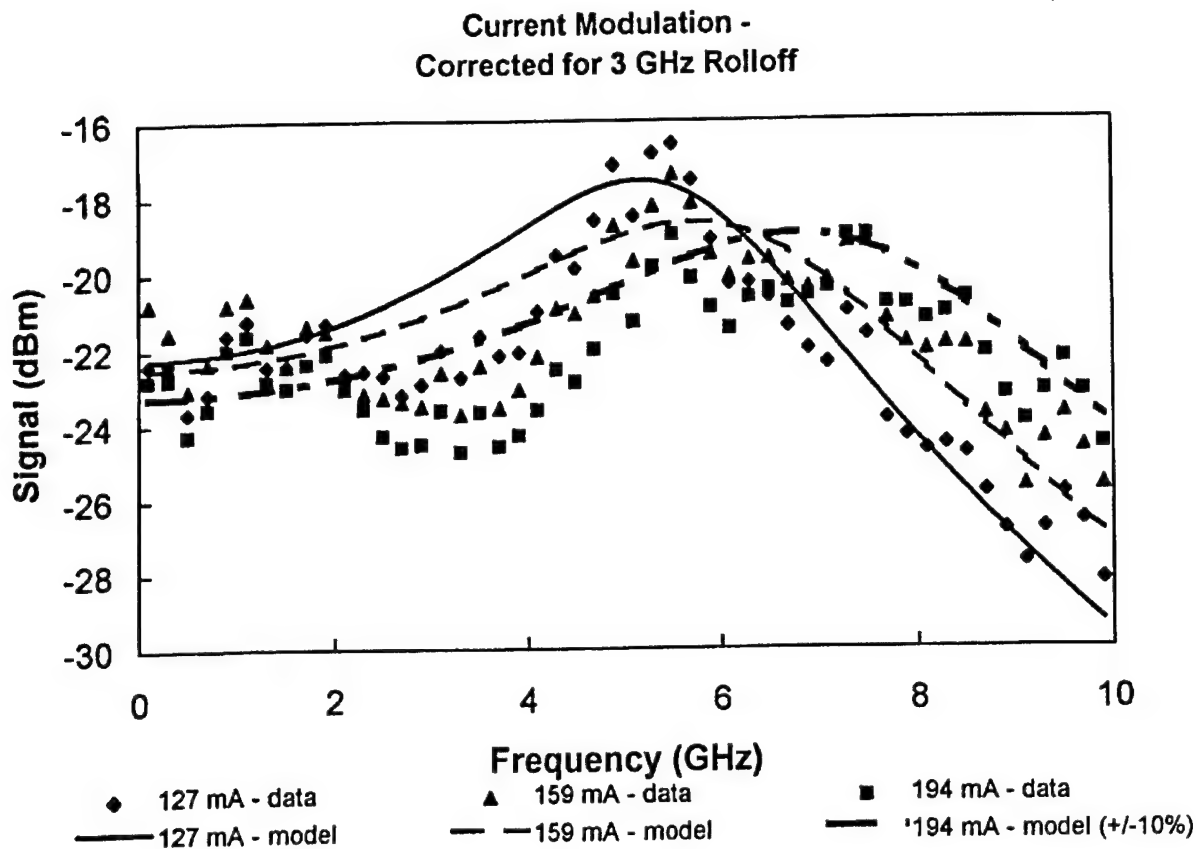


Figure 18. Spectra of the regeneratively amplified sideband due to a weak optical probe at two different bias currents in the hop-free range of single-mode operation. The calculated (model) curves use the parameters listed in the text.



R99-1042

Figure 19. Spectra of the amplitude (power) modulation due to a weak, sinusoidal current injected into the high-speed laser diode along with the dc bias current. The experimental data has been adjusted to eliminate the effects of a simple low-pass filter with a 3-dB frequency of 3 GHz. The calculated (model) curves use the parameters listed in the text except for the 194-mA curve where there was some parameter adjustment, < 10%, to produce a better fit.

b' . There were deviations between the measured data and the model predictions of Equation 15. A comparison of the calculated and observed asymmetry for the high-speed SDL lasers is shown in Figure 20. Data at two different current levels, approximately 6, Figures 20(a) and (b), and 9.5, Figures 20(c) and (d), times the threshold value, are compared with model calculations. The asymmetry value plotted in Figure 20 is the ratio of the positive offset sideband to the negative offset sideband. In 20(a) and (c) the value of b is allowed to vary while $b' = 2$, while in (b) and (d) the value of b' is allowed to vary while $b = 4.5$. From the figures it can be seen that the offset frequency of the maximum asymmetry is largely determined by for a fixed value of γ_p . The comparison limits the value of b' to a range between approximately 30-50% of the value of b . The smaller value of b' will have an impact on the nonlinear dynamics predicted by the model, producing better agreement with observed spectra.

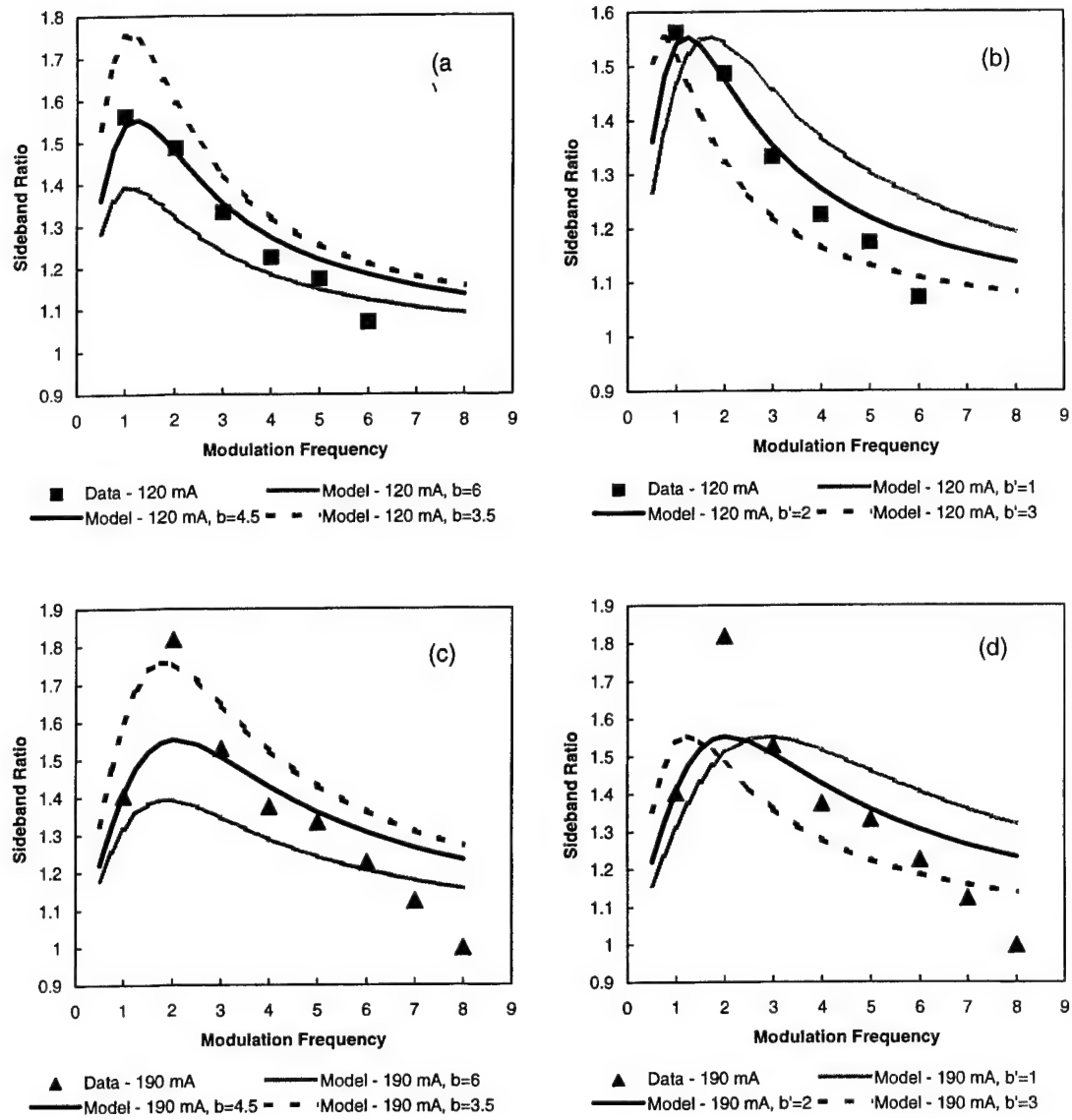


Figure 20. Comparison between the predicted and observed asymmetry of the sidebands in the optical spectra under current modulation. Plotted is the ratio of the positive to negative frequency offset sideband as a function of frequency of the current modulation. Measured data are compared with model calculations.

B. Micro-optical Devices VCSEL Arrays

The laser arrays ordered from Micro-Optical Devices (MODE) contain 12 devices in a linear configuration. Each VCSEL is 8 μm in diameter and device spacing is 250 μm . Gain confinement within the device is maintained by ion implantation. Details of the device structure were withheld by the manufacturer. The array that was extensively characterized was wire bonded and packaged by Microphotonics Branch at the Army Research Laboratory (ARL). Figure 21 is a picture of the devices and the wire bonding. An additional array was packaged in a high-speed ceramic substrate to provide better current modulation characteristics by New Century Consulting. Figure 22 is a picture of the substrate and Figure 23 is a picture of the delivered packaging. A ceramic substrate capable of connecting up to 5 VCSEL was used. The substrates was cut almost in half and then mounted to a Cu/Invar/Cu mounting/ground plate. A connection was hardwired to the lead frame pads in a manner to facilitate some impedance matching reference for the short substrate traces as well as for the wirebonds.

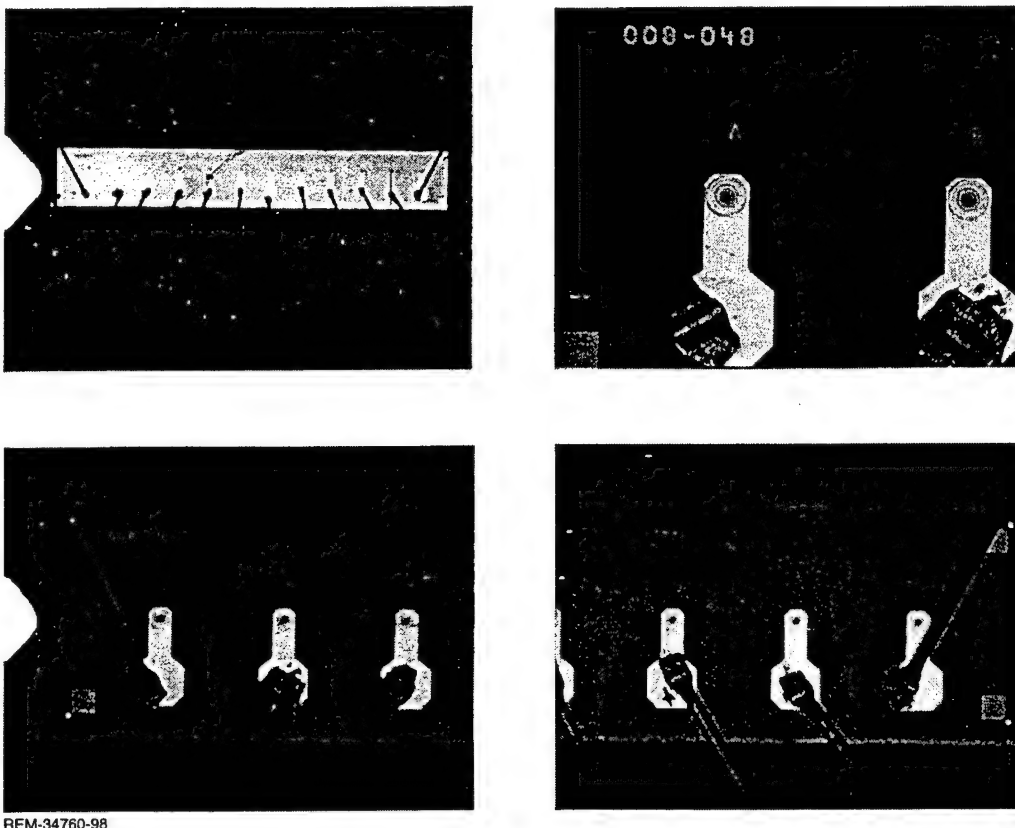


Figure 21. Pictures of the wire bonds used to contact the 1 x 12 MODE VCSEL array. The upper-left photo shows the full 1 x 12 VCSEL array, and the other three are details of parts of the array. The light-colored patterned areas in the detail photos are the metallization pads and the individual VCSELs are visible as dark spots near the end of the thinner part of the pad. Fabrication and photographing of the wire bonds were done by the Microphotonics Branch of ARL.

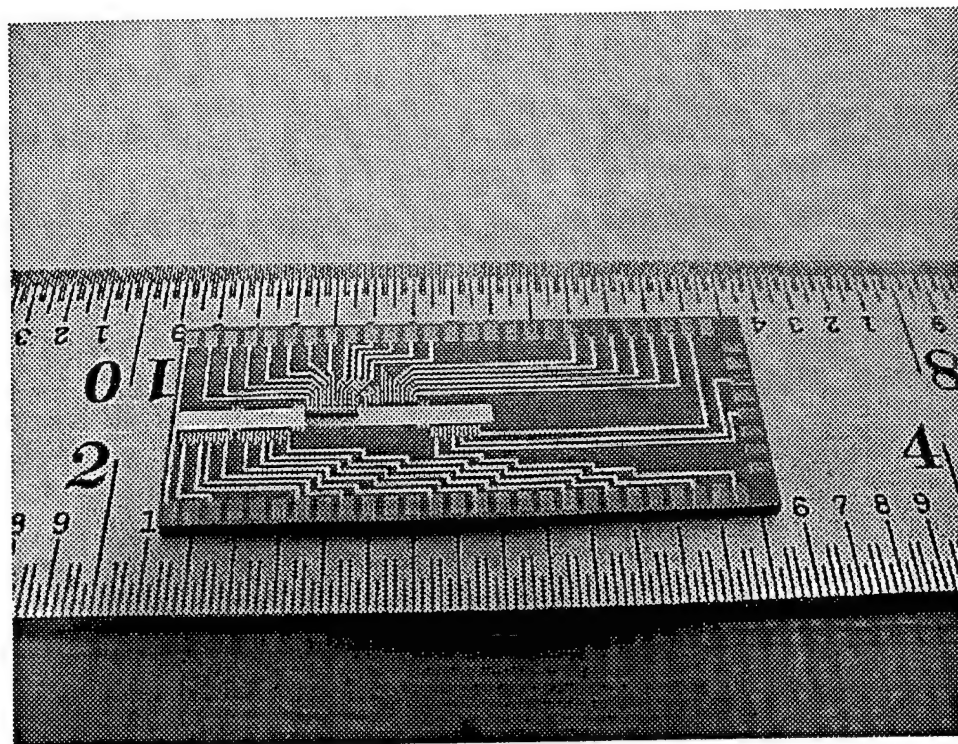


Figure 22. Picture of the ceramic substrate designed by New Century Consulting. The substrate was cut along the horizontal direction near the large gold pad for the current program. Photograph supplied by Dr. Chad Noddings, New Century Consulting.

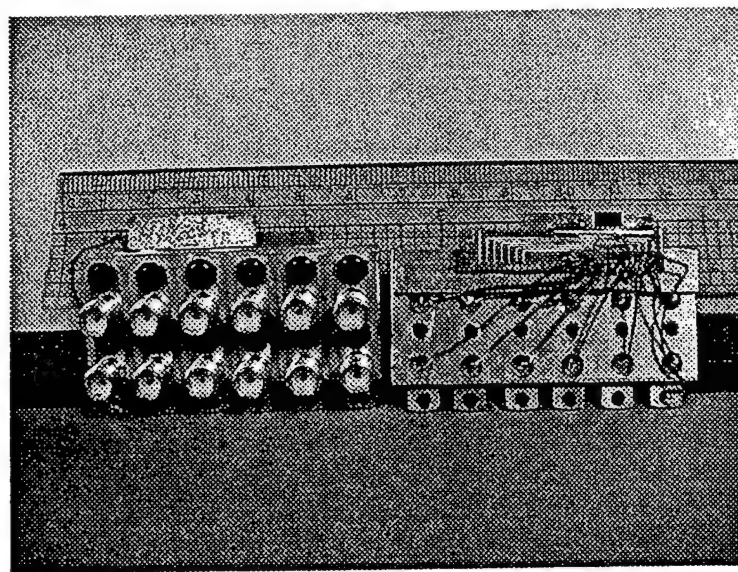
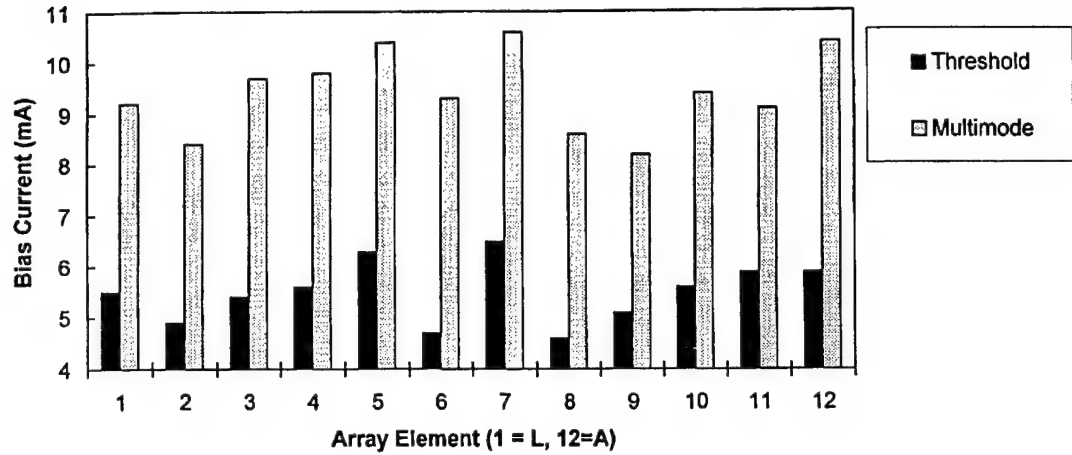


Figure 23. Picture of the high-speed package for the VCSEL arrays. Back view showing SMA connectors is on left. VCSEL array chip and ceramic substrate are at top of front side view on the right. The measuring stick behind is to give the scale. Package manufactured by New Century Consulting.

Characterization of the array addressed uniformity across the array as well as the performance of individual devices. Wavelength measurements were made with a wavemeter and polarization measurements were made with a fixed linear polarizer and a half-wave plate which could be rotated. Because higher order transverse modes of the VCSELs operate at a wavelength which is shifted with respect to the lowest order mode, we could observe the output of the wavemeter to detect the onset of additional modes. For these tests, each VCSEL emitter was individually powered while all other devices were uncoupled from the current source. Though we continued to measure variances between the devices in a variety of parameters, there was also a good degree of uniformity. First, all devices operated with a linear polarization that was uniformly oriented, within ± 10 degrees, across the array. Second, the individual VCSELs all operated in a single optical mode as the bias current was raised above threshold. Figure 24 plots the range of single-mode operation of the 12 individual devices by indicating the threshold currents and the currents where the wavemeter detected the presence of more than one optical frequency. VCSEL #1 is at one end of the array, and the other lasers are numbered sequentially.

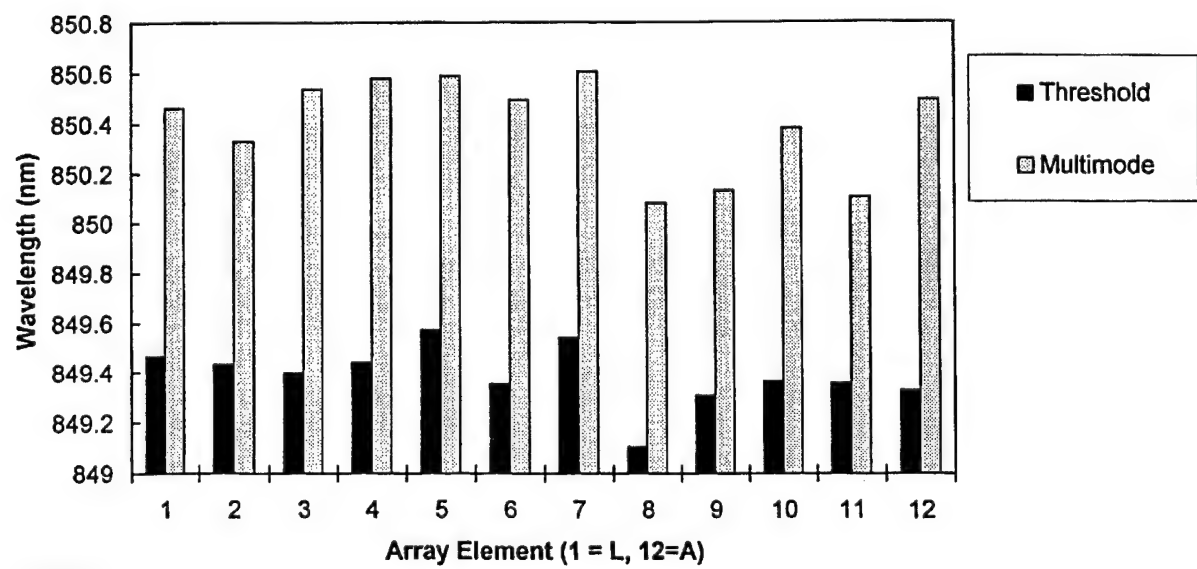
As the current is increased to the individual devices there is a shift in the output wavelength. The VCSELs showed approximately a -100 GHz/mA optical frequency shift with bias current. This shift compares with a shift of approximately -2 to -3 GHz/mA measured for the conventional, edge-emitting lasers. Thermal effects are primarily responsible for the frequency shift. Due to its smaller size, the VCSEL must dissipate heat over a much smaller volume. We also measured a -25 GHz/C shift with temperature. The large shift measured with the VCSELs manifested itself in the free-running operation of the array as a large frequency jitter in the optical frequency. Note that a $1\ \mu\text{A}$ current fluctuation is sufficient to induce a $100\ \text{MHz}$ frequency fluctuation. Commercially available laser diode drivers typically have current jitter specifications of $1\ \mu\text{A}$ or larger. We were able to reduce the actual current jitter delivered to the laser with the use of a voltage divider network where the VCSELs were in series with a 200-ohm resistor and this combination was in parallel with a 23-ohm resistor. This caused fluctuations in the current driver due to either voltage or current fluctuations to be largely dropped across the resistors rather than the VCSELs. The VCSELs have a differential resistance of approximately $40\ \text{ohms}$ when operating. The wavelength shift varied by less than $\pm 10\ %$ across the array. Figure 25 plots the range of wavelengths where single-mode operation was observed. Note that the data indicates that all lasers can be simultaneously operated at the same wavelength.

Choosing the average wavelength at $8\ \text{mA}$ as the possible operating point, the required current for each device was then calculated, Figure 26. Using the output power data from ARL, the spread in output powers across the array was then determined. This is shown in Figure 27. The spread in output power is from 0.5 to $1.5\ \text{mA}$. Also shown in Figure 27 is the associated pump parameter. The pump parameter is defined as the difference between the operating current and the threshold current, normalized to the threshold current. In identical devices, the output power will scale in proportion to the pump parameter. This is clearly not the case for the individual emitters in the array, nor is there consistency between output power and operating current.



R99-1043

Figure 24. Bias currents to the individual elements of the VCSEL array where the threshold for operation is achieved and where the laser exhibited multifrequency operation indicative of multimode output.



R99-1044

Figure 25. Wavelength of the optical output of the individual emitters of the VCSEL array at the threshold for laser operation and just before the laser exhibited multifrequency operation indicative of multimode output.

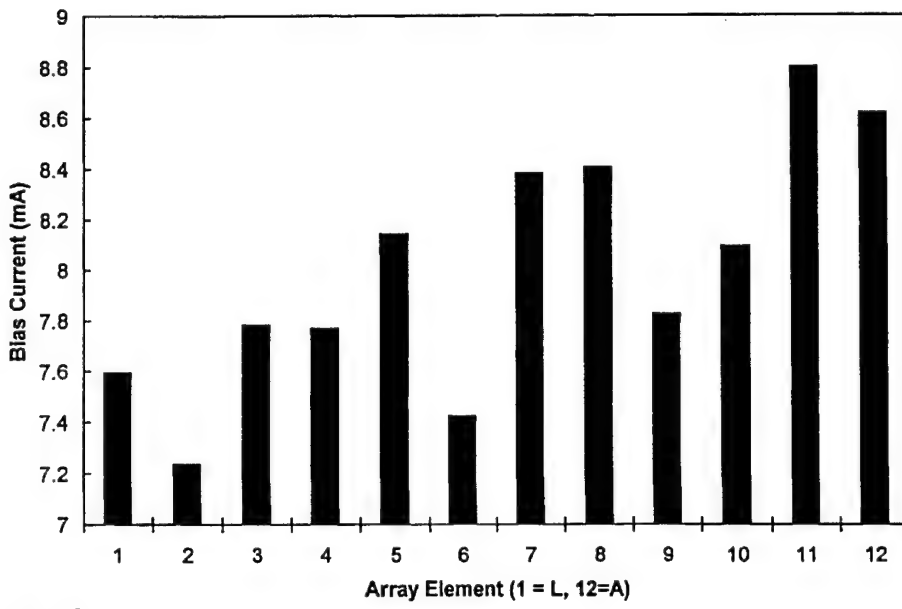


Figure 26. Bias currents to the individual emitters of the VCSEL array for operation at a wavelength of 850.04 nm, the average wavelength of the emitters when uniformly biased at 8 mA, near the upper limit of single-mode operation.

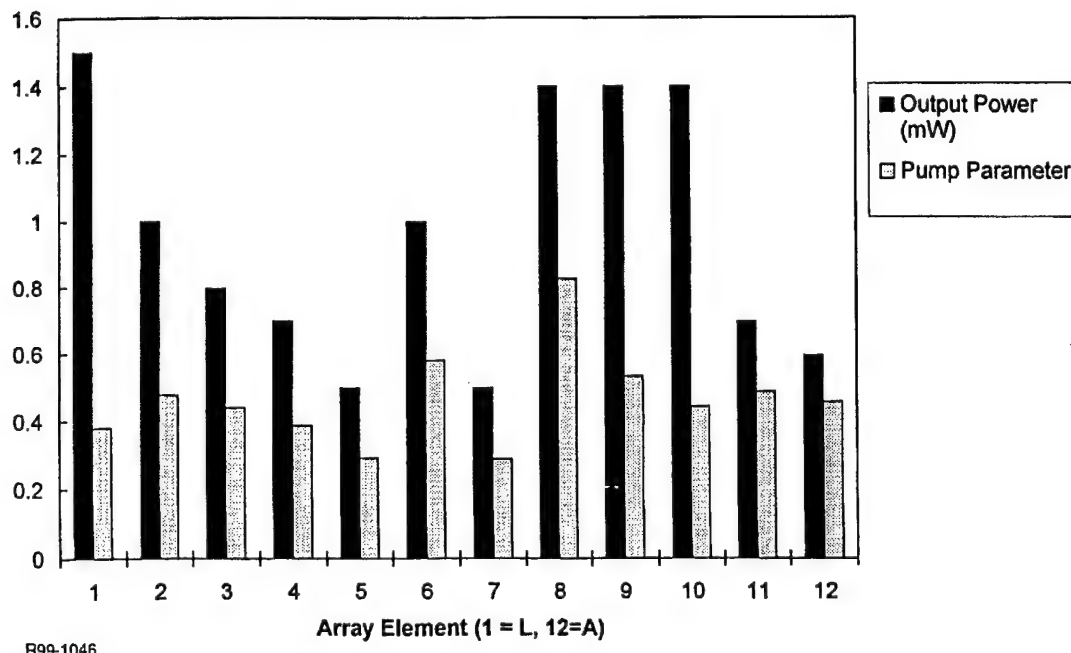


Figure 27. Output power, and corresponding pump parameter, of the individual emitters of the VCSEL array when biased to emit at 850.04 nm. The pump parameter is the difference between the bias current and threshold current of a laser, normalized to the threshold current.

Figure 28 compares the output power of three different lasers in the array as a function of the injection current. In addition to the variances summarized in Figures 24-27, the light vs. current characteristic for each device shows unique kinks and changes in slope, even within the region of nominally single mode operation. Figure 29 shows a typical pair of optical-injection measurements for one VCSEL at two operating points. The data show the regenerative amplification spectra of a weak optical probe. While the optical power versus current measurements showed variation across the array, the spectra generated by optical probing were consistent across the array at a given output power. Figure 30 shows an example of the regenerative amplification signal of a weak optical probe for the three different VCSELs used to plot Figure 28. All are operated at the same output power but different pump parameters. The experimental spectra and the calculated curve are offset to aid the comparison. Within experimental error, all three spectra are identical. Figures 31 and 32 plot Ω_r and γ , as a function of output power for the twelve VCSELs in the MODE array. Two operating points are shown for each laser, three for #7, with the laser number attached as a label. The data appeared to divide into a high power and low power set, but appeared to scale fairly consistently across the array. Such consistent scaling across the array does not occur if the current, current above threshold, or current above threshold scaled to the threshold current is used as a basis for comparison. This will be discussed more thoroughly below. Also shown in Figures 31 and 32 are fits to the data.

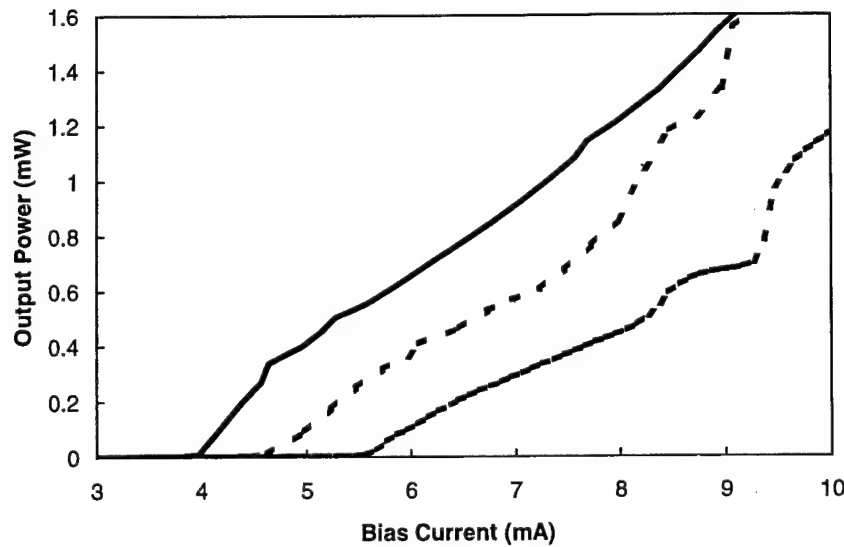


Figure 28. Output power as a function of bias current for three different lasers in the array showing different threshold currents and power vs. current slopes. At 0.9 mW, the lasers had pump parameters of 0.65 (solid curve), 0.81 (long-dash curve), and 0.72 (short-dash curve).

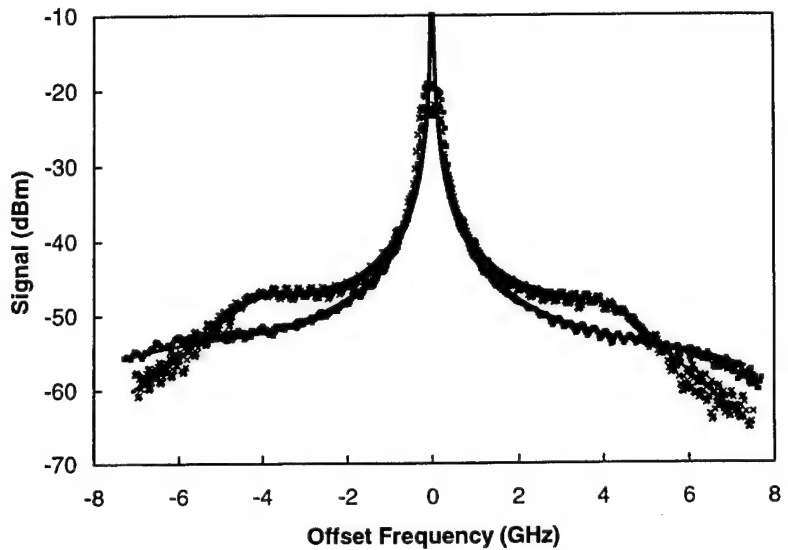


Figure 29. Regenerative amplification spectra of VCSEL #9 at two different bias currents. The data with the narrower but stronger sidebands was taken at a bias current of 6.35 mA, and the other data was taken at a bias current of 7.85 mA. The curves are model calculations using the parameters given in the text.

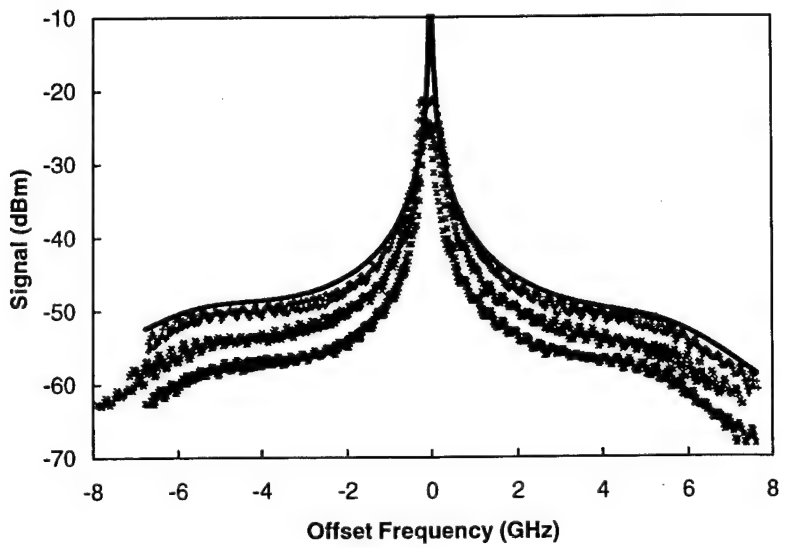


Figure 30. Regenerative amplification spectra of three different VCSELs from a 1×12 array operating at an output power of 0.9 mW and a calculated spectrum. The 300-MHz weak, periodic structure is an experimental artifact. The lasers operated at different bias currents, with pump parameters of 0.65 (top), 0.81 (middle), and 0.72 (bottom).

The single-mode model predicts that five key parameters, b , γ_c , γ_s , γ_n , and γ_p , define the modulation spectra of a free-running laser. The first three parameters are independent of the output power. However, γ_n , and γ_p scale in proportion to the output power. Therefore, the relaxation resonance frequency, Ω_r , should scale with the square root of the output power and the total decay rate, γ_r , should scale in proportion to the optical power. Using this rule, the data appeared to divide into a high-power and low-power set. The calculated lines have a $1/2$ -power slope for the Ω_r data and a linear slope for the γ_r data. Based upon a series of optical modulation measurements at different bias currents, the following parameters were generated for the high power set:

- Linewidth Enhancement Factor = 7 ± 3
- Gain Saturation ratio = 7 ± 4
- Cavity Photon Decay Rate = $4.5(\pm 1.5) \times 10^{11} \text{ s}^{-1}$
- Carrier Spontaneous Decay Rate = $1(\pm 1) \times 10^9 \text{ s}^{-1}$
- Differential Gain Relaxation Rate = $3.4(\pm 1)P \times 10^9 \text{ s}^{-1}$
- Nonlinear Gain Relaxation Rate = $2.4(\pm 0.3)P \times 10^{10} \text{ s}^{-1}$

In parameters 4 and 5 the symbol P refers to the output power in milliwatts. Note that we cannot use a simple \tilde{J} parameter across the array due to the variances from laser to laser. For the low power set, three parameters are changed:

- Cavity Photon Decay Rate = $3.7(\pm 1.2) \times 10^{11} \text{ s}^{-1}$
- Differential Gain Relaxation Rate = $2.2(\pm 0.7)P \times 10^9 \text{ s}^{-1}$
- Nonlinear Gain Relaxation Rate = $1.6(\pm 0.3)P \times 10^{10} \text{ s}^{-1}$

These parameters produced a good fit to the experimentally measured data. Except for the value of the linewidth enhancement factor and gain saturation ratio, they appear to be consistent across the array. The variation in the linewidth enhancement factor and gain saturation ratio arises from both variations between devices and variations with injection current for individual devices. Figures 28 and 29 show examples of the fit of a measured spectrum to the model. The strong injection data narrowed the allowable range of values for the linewidth enhancement factor. Relative to other lasers we have measured, the linewidth enhancement factor is somewhat high, as is the ratio of the nonlinear gain relaxation rate to the differential gain relaxation rate. It is possible that there is some systematic error in these measurements, as the higher values of b and γ_p tend to cancel each other in the spectra.

The division of the data into high-power and low-power sets is not strictly justified using the single-mode model. However, there is other experimental evidence to support such a division. It has been reported that the mode size of a VCSEL can change as the operating power is increased with thermal lensing being used as the most likely mechanism.¹⁴ The change in parameters is consistent with a decrease in the spot size, in agreement with the past measurements. The thermal sensitivity of the VCSELs in the array has already been discussed. The data indicates that different VCSELs change their mode patterns at different power levels and does not show whether the change is abrupt or smooth.

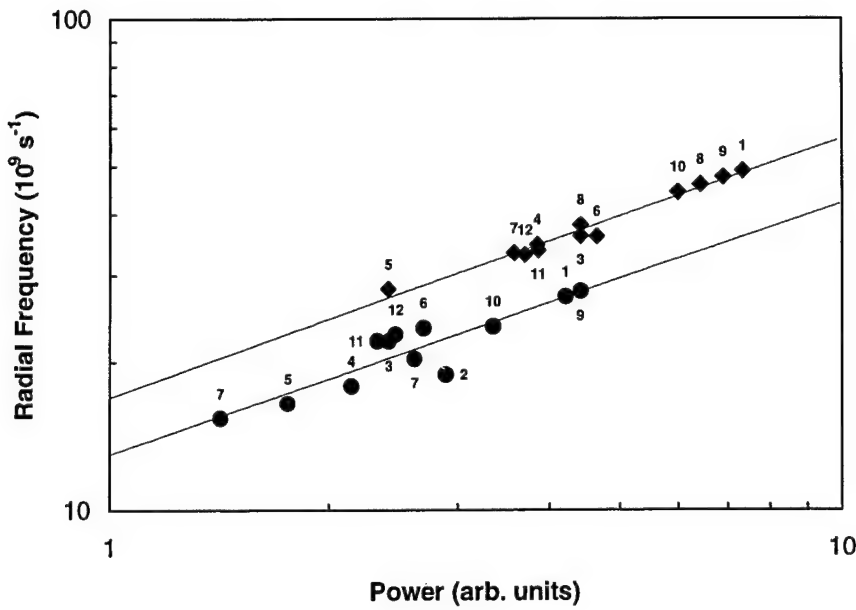


Figure 31. Relaxation resonance radial frequency, Ω_r , as a function of output power for the 12 VCSELs in the array. The numbers refer to the laser element with #1 corresponding to die label L. The curves are best fit curves assuming that Ω_r is proportional to the square root of the output power. The data divides into two sets.

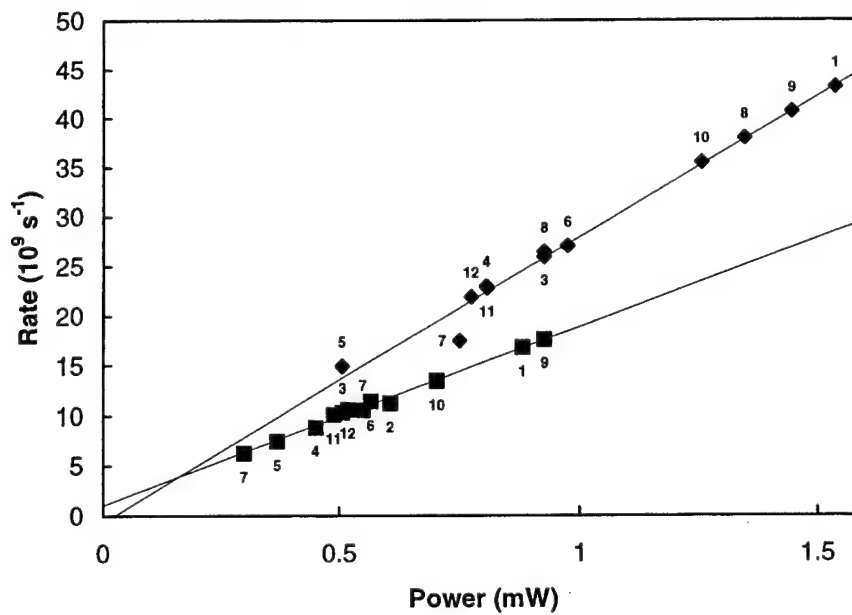


Figure 32. Overall decay rate, γ_r , as a function of output power for the 12 VCSELs in the array. The numbers refer to the laser element with #1 corresponding to die label L. The curves are linear best fit curves assuming that the increase in γ_r is proportional to the output power. The data divides into two sets.

Figure 33 shows near field images of one VCSEL as the current level is increased. Below threshold, at 2 mA, light is emitted over the across the 8 μm structure. The high intensity laser spot appears above threshold, initially centered near the top edge of the structure. The position, shape and size of the high intensity spot show changes as the current is increased in the single spatial mode operating range, until higher order spatial modes are observed in the 10.5 mA picture. These changes are consistent with a jump to a different operating condition, as is observed in the dynamic parameter data. For this laser the change occurs between 6.35 and 7.85 mA. Note that the near field images show that emission at the edge of the VCSEL is still evident at the lower current level but not at the higher level. Qualitatively, the output appeared to be more stable once the lasers were governed by the high-power parameters. However, the lasers that achieved the highest single-mode output powers had the highest transition levels from low-power to high-power operating characteristics.

Near Field Images of VCSEL Emission

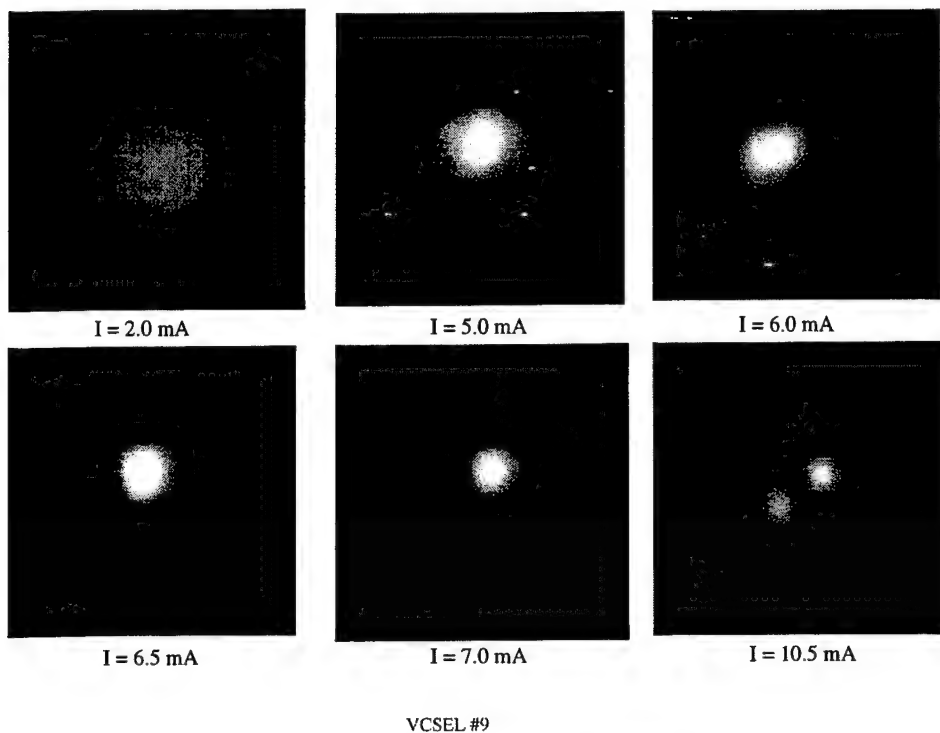


Figure 33. Near field images of one of the MODE VCSELs as the current is increased. Photos taken by Dr. Jiang Liu of the Microphotronics Branch of ARL.

Accepting this division of the data, it is quite significant that all of the VCSELs in the array can be modeled with a common set of parameters, as long as optical power, but not some current-based parameter, is used to compare the data. In the single-mode model that we use, the optical power should be equivalent to the pump parameter. The pump parameter is the ratio of the difference between the operating current and the threshold current and the threshold current. The optical power scales in proportion to the pump

only over small ranges for any of the lasers and the scaling is different from laser to laser. The good agreement with the model when optical power is used to describe the operating point indicates that the intrinsic parameters of the optical cavity and the coupling of the cavity to the gain medium are relatively consistent across the array. Note that, within experimental error, all of the lasers have the same dynamic parameters at the same output power. No additional proportionality is required to get agreement. However, to achieve the same output power, the lasers require a different bias current and have a different optical frequency. Given the temperature sensitivity of the VCSELs, the different optical frequencies could be due to different thermal losses from VCSEL to VCSEL. The key variable appears to be the coupling of the injection current into the gain medium, or perhaps the distribution of the current density across the gain medium. The single-mode laser has a well-defined mode pattern. If the current distribution across the mode pattern varies from laser to laser, this might explain the observed variability. Variation in the output characteristics from laser to laser can be a result of photolithography, implantation, doping profiles and a number of other issues, and the variance observed from laser to laser is still a bit of a puzzle.¹⁵

C. Honeywell VCSEL Array

A second set of laser arrays was fabricated by the Honeywell Technology Center. These laser arrays contain 14 devices in a linear configuration. Each VCSEL is 2 μm in diameter and device spacing is 250 μm . Gain confinement within the device is maintained by oxidation. Details of the device structure were withheld by the manufacturer. The array that was extensively characterized was wire bonded and packaged by Microphotonics Branch at the Army Research Laboratory (ARL). An additional array was packaged in a high-speed ceramic substrate to provide better current modulation characteristics by New Century Consulting.

In comparison with the MODE array, the VCSEL array from Honeywell displayed much greater uniformity in the output power vs. injection current characteristic across the array. The smaller size of the Honeywell VCSELs, along with the oxide confined structure, yielded a sub-milliampere threshold current. The lower threshold current allows single-mode operation of these VCSELs at bias currents that are higher, relative to threshold, than the MODE devices. The lasers oscillated in one spatial, longitudinal and polarization mode up to more than ten times the threshold current, while the MODE arrays went multimode at approximately twice the threshold current. Our model indicates that this should make a difference in the nonlinear phenomena we observe, and in the relative importance of noise characteristics. However, the Honeywell array has a much greater spread in operating wavelengths. Devices within the same array would not oscillate at the same wavelength.

Unlike the MODE VCSELs, the Honeywell VCSELs in the array showed very similar output power vs. injection current characteristics. All had a threshold current close to 0.25 mA and similar slopes of 0.37 mW/mA. This consistency translated over to the dynamic characteristics as well. Figure 34 plots examples of regenerative amplification

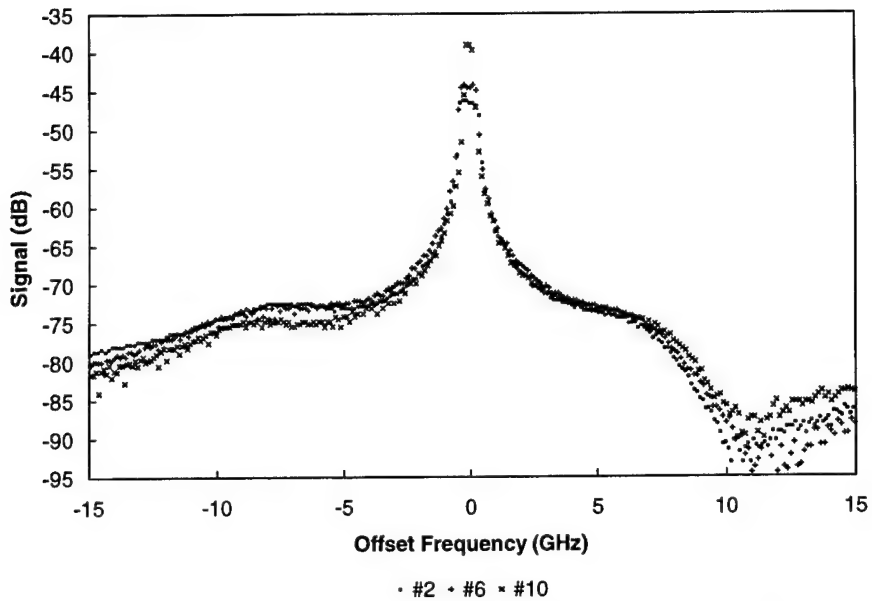


Figure 34. Regenerative amplification spectra of three different elements of the Honeywell VCSEL array with the bias current at 0.52 mA, twice the threshold value.

spectra for three lasers in the array, all biased at twice the threshold current of approximately 0.26 mA. The spectra are fairly consistent, with one laser showing slightly larger relaxation resonance frequencies and a greater asymmetry with respect to positive and negative offsets. The asymmetry variance was due, at least in part, to the presence of a sub-threshold orthogonally polarized mode. This will be discussed further below. The consistency of the Honeywell VCSEL spectra contrasts with the characteristics of the MODE array. That array showed much less consistency when lasers were compared at the same current level, similar consistency when compared at the same output power. The differences in the two arrays are suggestive that the key variation in the MODE array is the coupling of current to the oscillating mode, while for the Honeywell array it is slight differences in the fundamental laser parameters. The key fabrication difference between the two arrays appears to be the use of oxidation as a gain confinement mechanism in the Honeywell array and ion implantation in the MODE array.

While the polarization of the single mode output of the Honeywell VCSEL was linear, we observed that some devices underwent a polarization flip of approximately 90 degrees as the current was increased over the range of single mode operation. Above and below the current level for the flip, the operation is with a single polarization. Accompanying the flip is a small wavelength shift of 10-15 GHz. The presence of a near-resonant, orthogonally-polarized, sub-threshold mode complicated the interpretation of spectra made using optical injection. Figure 35 shows an example of this. Shown are regenerative amplification spectra for one VCSEL biased at 0.4 mA, 1.6 times threshold. The data shown in square boxes is taken with the polarization of the optical injection and detection oriented to be parallel to the polarization of the dominant mode of the free-running VCSEL. The other data is for optical injection and detection to be polarized 45 degrees

with respect to the VCSEL polarization. The curve is a calculated spectra using the parameters to be given below. The 45-degree polarization data shows the presence of the mode that is orthogonally polarized to the dominant mode. It is the peaked feature at an offset of approximately 14 GHz. This feature becomes broader and weaker as the bias current is further raised above threshold.

Subtler, but also evident in the spectra, is a change in the asymmetry of the broad sidebands of the central feature. Our characterization technique uses the asymmetry as a key factor in the determination of the linewidth enhancement factor, b . Figure 35 shows that if there is misalignment of the polarization of the injected or detected signal, the presence of the orthogonal polarization mode will corrupt the spectra. In conventional edge-emitting lasers, or the DFB lasers to be discussed below, the device structure suppresses the orthogonal polarization mode so that this is not an issue. In VCSELs, however, there is symmetry in the output plane so that it is minor imperfections in the device that yield the polarized output. Perturbations, such as the injection of an optical signal, can change the suppression ratio of the strong to weak polarization direction, and influence the modulation characteristics of the laser.

Using the single mode model to determine the dynamic characteristics of the laser relies on a single-mode description of the laser. Therefore, with VCSELs, special care must be taken to match polarization directions if an accurate determination of b and b' is to be made. While we did not observe the influence of weak, orthogonally polarized modes during the characterization of the MODE VCSELs, we did not fully understand the situation with the Honeywell VCSELs until very late in the program, after we had completed the characterization of the MODE VCSELs. As before, we used the asymmetry of the optical sidebands generated by a weak modulation current to determine

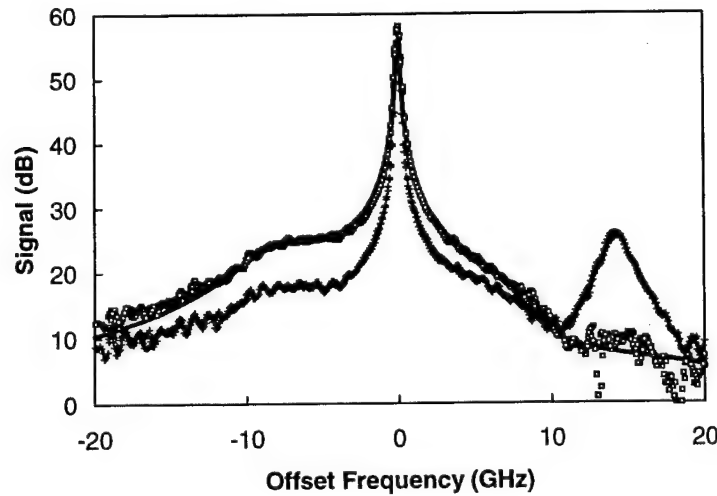


Figure 35. Regenerative amplification spectra of one Honeywell VCSEL biased at 0.4 mA, approximately 1.6 times the threshold current. The data shown in square boxes is for injection and detection polarization in the same direction as the free-running polarization of the VCSEL. The data shown in crosses is for injection and detection polarized 45 degrees with respect to VCSEL polarization.

he value of b' . Figure 36 compares data with calculated curves. A value of $b = 2.3$ was determined from the optical probing data and was used for the calculations.

Based on the experimental data and the coupled-equation model, we determined that the following dynamic parameters best described the VCSELs in the Honeywell array:

1. Linewidth Enhancement Factor (b) = 2.3
2. Ratio Factor for Nonlinear Gain (b') = 1.7
3. Cavity Photon Decay Rate (γ_c) = $2.9 \times 10^{11} \text{ s}^{-1}$
4. Carrier Spontaneous Decay Rate (γ_s) = $4 \times 10^9 \text{ s}^{-1}$
5. Differential Gain Relaxation Rate (γ_n) = $8.8 \tilde{J} \times 10^9 \text{ s}^{-1}$
6. Nonlinear Gain Relaxation Rate (γ_p) = $18 \tilde{J} \times 10^9 \text{ s}^{-1}$
7. Threshold current = 0.25 mA

The calculated curves in Figures 34 and 35 use these values. The threshold current is more than an order of magnitude below the MODE VCSEL and two orders below the high-speed laser diodes. Also, the linewidth enhancement factor, b , is quite small. Previously, we have never measured a value below approximately 4 for this parameter. This small value of b has a profound influence on the nonlinear dynamics that we observe, as will be seen in the next section. We further observed that the linewidth enhancement factor appeared to scale monotonically with wavelength. The array that we characterized had VCSELs emitting in the 838-842 nm spectral region. The linewidth enhancement factor appeared to show a small shift to higher values with increasing wavelength. A second array had lasers that emitted at wavelengths below 830 nm and we measured a value of $b = 1.8$ for a VCSEL operating at 829 nm.

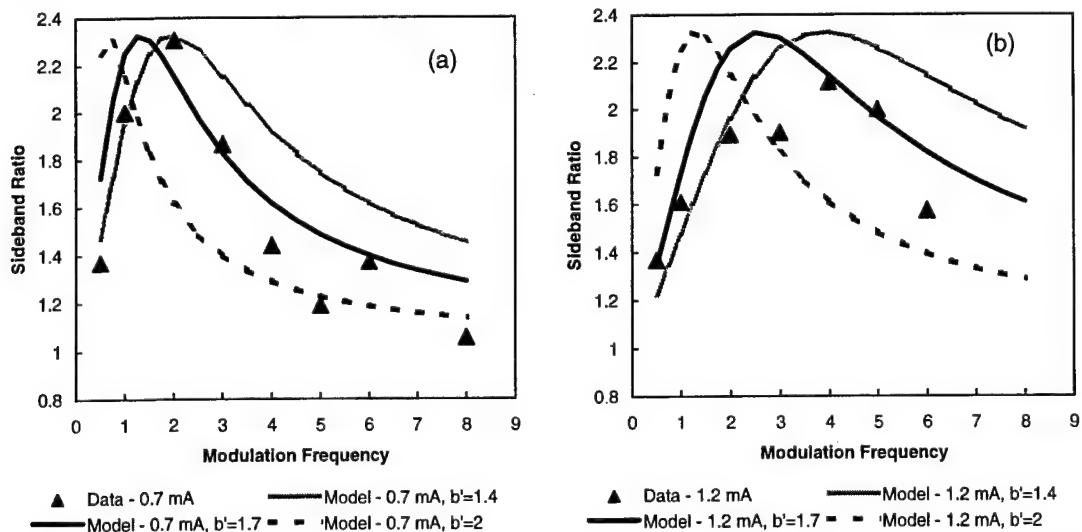


Figure 36. Asymmetry of the sidebands, given as the ratio of the positive to negative offset sideband, of a Honeywell VCSEL at bias currents of (a) 0.7 and (b) 1.2 mA. A value of $b = 2.3$, determined from the weak optical injection data, is used for the calculated curves.

D. DFB Lasers

We also characterized a commercially available DFB laser that emitted light in the 1.55- μm spectral region. The laser is an Alcatel Model 1915 LMO, a fiber coupled device mounted in a standard butterfly package without an optical isolator. This model is now discontinued by Alcatel but another model, the 1902 LMC, appeared to have similar optical characteristics. However, it is mounted in a standard 5.6 mm transistor can and is not fiber coupled. We used the 1902 LMC in our compact implementation of the double-locked laser. The fiber-coupled unit was particularly convenient for characterization, however. Operating at 1.55 μm , the laser could be coupled into various fiber-optic beamsplitters, polarization controllers, isolators and circulators, and attenuators. In the fiber-coupled configuration, we used standard fiber couplers and found that it was necessary to use angled physical contact (APC) type connectors for any connector not isolated from a laser emitter. The -30 to -40 dB losses from the standard physical contact (PC) connectors was not sufficient.

The fiber-coupled configuration was robust and relatively easy to use for characterization. We did not have an optical spectrum analyzer at 1.55 μm so that all measurements were made with the combination fast photodiode and microwave spectrum analyzer, with the probe laser also being used as a local oscillator for optical spectrum measurements. Output power as a function of bias current for the 1915 LMO is summarized in Figure 37. The data is shown along with a linear least squares fit, and the equation corresponding to the fit. From the equation, a threshold current of 5.4 mA is calculated. Dynamic parameters were determined from the optical probing data. Figure 38 plots the data and least squares curves for the relaxation resonance frequency, the relaxation decay rate and the gain damping contribution to the resonance decay rate.

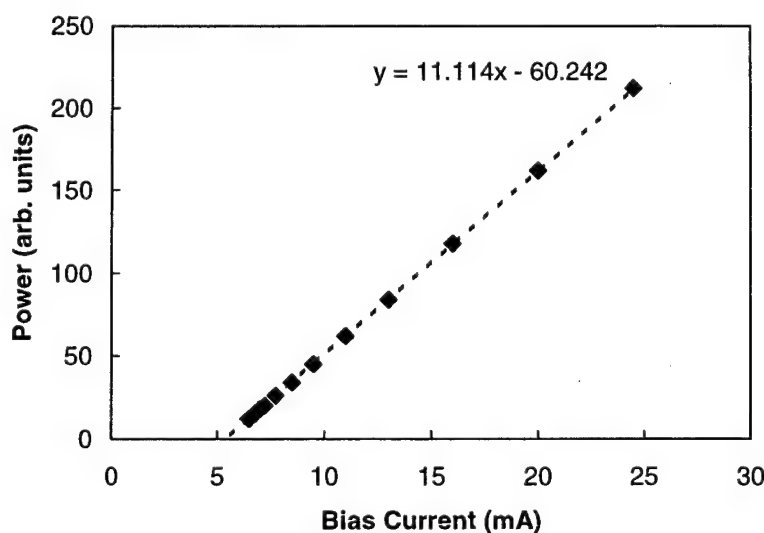


Figure 37. Output power of the Alcatel Model 1915 LMO DFB laser diode. Data is shown along with a linear least squares fit that gives a threshold current of 5.4 mA.

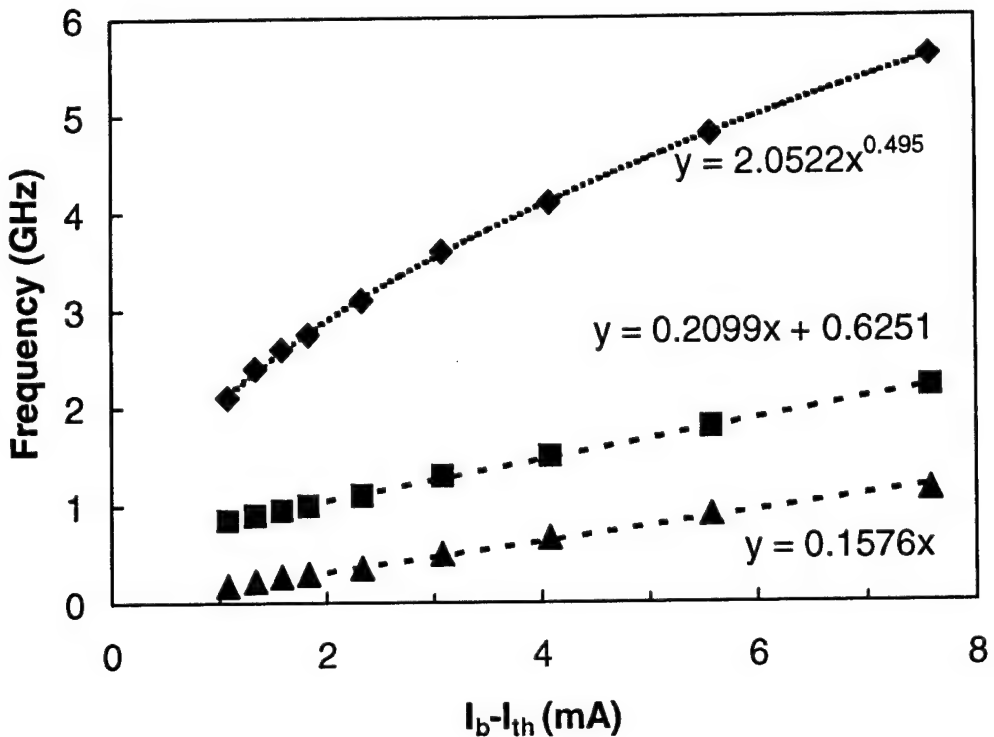


Figure 38. Key frequencies measured from the spectra of the 1915 LMO as a function of the current level above threshold. The relaxation resonance frequency (diamonds) is plotted along with a power-law least squares fit. The resonance decay rate (squares) and gain saturation damping (triangles) are plotted along with linear least squares fits. All data is given in frequencies in this chart, as opposed to the angular rates given elsewhere in the text.

The relaxation resonance frequency, f_r , should scale with the square root of the current level above threshold. From the data and associated power law least squares fitting curve in Figure 38, we see the proper progression to good accuracy. Likewise, the resonance damping rate, g_r , and gain saturation damping, g_p , follow linear curves. The value for g_r at threshold gives g_s , the spontaneous damping. Finally, g_c the photon decay, can be calculated from the other rates. All values from Figure 38 need to be multiplied by 2π to be compared with other data in this section. From the data, we determine that:

1. Linewidth Enhancement Factor (b) = 3.5
2. Ratio Factor for Nonlinear Gain (B) = —
3. Cavity Photon Decay Rate (γ_c) = $5 \times 10^{11} \text{ s}^{-1}$
4. Carrier Spontaneous Decay Rate (γ_s) = $4 \times 10^9 \text{ s}^{-1}$
5. Differential Gain Relaxation Rate (γ_n) = $1.7 \tilde{J} \times 10^9 \text{ s}^{-1}$
6. Nonlinear Gain Relaxation Rate (γ_p) = $5.4 \tilde{J} \times 10^9 \text{ s}^{-1}$
7. Threshold current = 5.4 mA

We were not configured to perform the measurement of the asymmetry of the optical sidebands under current modulation. Therefore, we could not determine b' . Based on the observed nonlinear dynamics under strong optical injection, we estimate that b' must be approximately 50% of the value of b .

E. Characterization Summary

Table 1 summarizes the dynamic parameters determined from the weak optical injection and current modulation measurements. Note that we could not use the usual pump parameter, \tilde{J} , with the MODE VCSEL. Instead the values of γ_n and γ_p are calculated using the output power in (mW). For a rough comparison P is approximately 1 mW when $\tilde{J} = 1$. Accuracy in the table is $\pm 20\%$. While there is a range of parameters across different devices, it is interesting that all parameters, except the threshold current fall within the same order of magnitude even though the device sizes and feedback properties vary significantly.

	SDL High Speed Laser Diode	MODE VCSEL	Honeywell VCSEL	Alcatel DFB Laser Diode
b	5	4.5-7	2.3	3.5
b'	2	3-7	1.7	-
$\gamma_c (\times 10^9 \text{ s}^{-1})$	250	450 (370)	290	500
$\gamma_s (\times 10^9 \text{ s}^{-1})$	1.9	1	4	4
$\gamma_n (\times 10^9 \text{ s}^{-1})$	$1.0 \tilde{J}$	$3.4P (2.2P)^*$	$8.8 \tilde{J}$	$1.7 \tilde{J}$
$\gamma_p (\times 10^9 \text{ s}^{-1})$	$2.8 \tilde{J}$	$24P (16P)^*$	$18 \tilde{J}$	$5.4 \tilde{J}$
I_{th} (mA)	20	5	0.25	5.4

*P in (mW), lower value valid for low power, approximately < 0.5 mW, higher value above.

Table 1. Comparison of device dynamic parameters.

5. NONLINEAR DYNAMICS

In previous work, we have experimentally investigated the nonlinear dynamics that can be generated by injecting a near-resonant optical signal into a semiconductor laser biased above threshold.³ Figure 39 is a map of the experimentally observed dynamics in an SDL 5400 series laser biased at 1.67 times threshold, where the relaxation resonance frequency of the free-running slave laser is approximately 3 GHz. A wide variety of dynamics is observed as the offset frequency of the master laser and the strength of its injected signal are varied. These are labeled in the figure by: S – Stable operation, 4 – Four-wave and multiwave mixing, P1 – Limit cycle, P2 – Period doubling, SR – Subharmonic resonance, P4 – Period quadrupling, M' - Complex multiwave or quasiperiodic, and Chaos – Deterministic chaos. Because the 5400 series lasers are standard, edge-emitting Fabry-Perot laser diodes, they can oscillate in more than one longitudinal mode. In the hatchmarked regions, the M' region and the Chaos regions, a significant fraction of the optical power was emitted in another mode under optical injection. The arrows mark one-way transition boundaries which when crossed in the directions of the arrows induce a mode hop out of the free-running mode but do not have the reverse transition. Because theoretical work has predicted that additional dynamics may occur precisely in the regions that are obscured by mode hops, we wanted to perform a mapping of lasers such as VCSELs or DFB lasers that would not undergo a mode hop. We also wanted to compare the predictions of the model with the observed spectra in the strong injection limit.

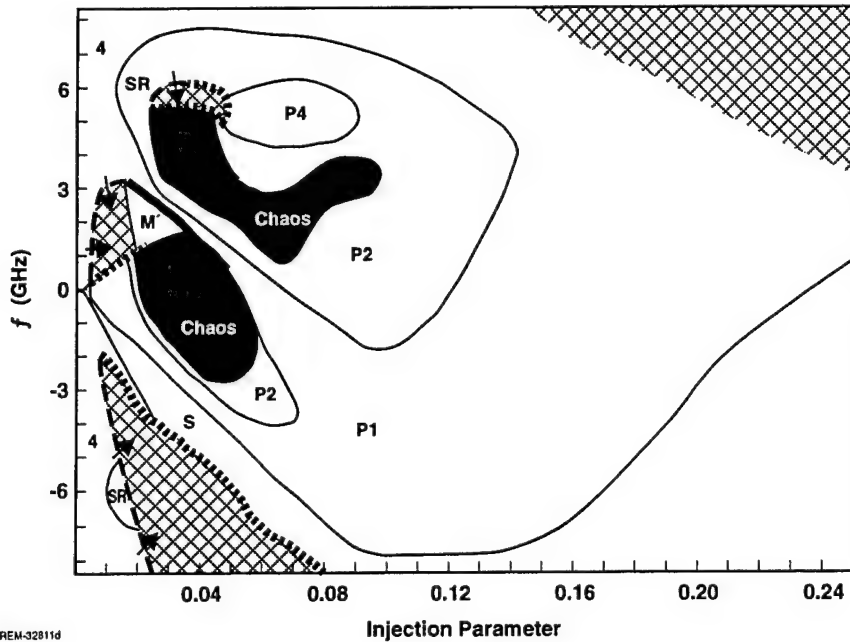


Figure 39. Mapping of the experimentally observed dynamic regions for a conventional edge-emitting semiconductor laser with $\tilde{J} = 2/3$. The dynamics are determined by comparison of observed spectra with calculated spectra with and without noise. Symbols are defined in the text.

A variety of features were observed in the experimentally measured and numerically calculated spectra of the different lasers under external optical injection. A convenient way to consolidate the predictions of the model is through the use of bifurcation diagrams, as we showed in Figure 6. Experimentally measured spectra can be compared with the predicted dynamics of the bifurcation diagram.

A. High-Speed SDL Lasers

Several details of the spectra of the SDL lasers were uncovered in the current program. They relate to the routes into and out of chaos and the continuity of solutions within the different dynamic regions. In our earlier work we showed that the SDL lasers exhibited a period doubling route into chaos with optical injection at the free-running frequency. The period-doubling route was clear in the calculated bifurcation diagrams. However, in the experimental data we only observed the first period doubling, and surmised that the higher order doublings were obscured by the intrinsic noise of the system. Work in the current program showed that the situation is not necessarily that simple.

Figure 40 shows a set of spectra for the route to chaos another SDL laser, biased further above threshold than the original lasers that we investigated. We show a progression of spectra for the optical output and regenerative amplification signal, lower dashed curves and upper solid curves respectively, as a function of injection strength. The spectra are taken with the master laser tuned to the free-running frequency of the slave laser. The signal levels, in dB, are relative to the noise background and frequency offset is relative to the free-running optical frequency of the slave laser, and in this case also the master laser. Each of the spectra is an overlay of two sets of data. The optical spectrum of the free-running laser without optical injection consists of a single narrow feature indicating that the laser is operating in the steady state, Figure 40(a). The regenerative amplification spectrum shows broad, weak, asymmetric sidebands about the central peak with maxima offset by the relaxation resonance frequency. The asymmetry is due to the fact that the free-carrier density modulation induced by the probe laser causes changes in the refractive index, as well as the gain, of the semiconductor medium. Similar features would also be present in the free-running optical spectrum but are obscured by the noise.

Injecting a sufficiently strong optical signal causes the resonance to become undamped. The optical spectrum now consists of a series of peaks offset by approximately the relaxation resonance frequency, as shown in Figure 40(b). This indicates that the intensity and the phase of the laser are oscillating at this frequency as well as higher harmonics. The regenerative amplification spectra shows a similar set of peaks, with the notable exception of a peak at the injection frequency, all riding on a broad, structured background feature. At higher injection levels, Figure 40(c), new spectral components appear at frequencies half way between the resonance frequency lines. The appearance of these features indicates that a period doubling bifurcation has occurred. Increasing the injection level still further causes the features in the spectra to shift out of a period-two progression, Figure 40(d). Frequencies at 1/3 of the fundamental frequency are now present, most clearly in the optical spectrum, suggesting that the attractor is a period three object. Notice also that there are also 2/3 components indicating that a bifurcation diagram should show three distinct crossing of the Poincare section. Except for the peak at the injection frequency there is considerable broadening of the spectral features in the

optical spectrum, including those at multiples of the resonance frequency. The discrete spectral features are also superimposed on a broad background feature. Finally in Figure 40(e) the spectra display various broadened resonance peaks and a strong, structured background signal that is consistent with chaotic dynamics. The spectral peaks that remain are more consistent with a period-two frequency spacing. Therefore, the transition to chaos is more complicated than a simple period-doubling bifurcation sequence.

The path out of chaos is also complex. Figure 39 shows a broad line at the upper transition from chaotic dynamics back to periodic dynamics for optical excitation at the free-running optical frequency. It indicates a discontinuous transition. The laser was simultaneously returning to essentially single mode operation as it returned to periodic dynamics. In the region of chaotic dynamics, a significant fraction of the optical output was transferred to other longitudinal modes. Figure 41 shows the spectral changes that accompanied this transition. All conditions are the same as for the spectra in Figure 40 except that the injected optical power is increased, as indicated in the caption. Figure 41(a) shows a spectrum of chaotic dynamics near the upper boundary. Relative to the spectrum in Figure 40(e), the regeneratively amplified peak at the injection frequency is much weaker and there is no evidence of period-two dynamics. The strongest spectral feature is offset from the injection frequency by approximately 5 GHz. This offset becomes the spacing for a set of spectral features that emerge out of the chaotic continuum as the injection is further increased. As they begin to dominate, however, a second set of features with a larger offset, approximately 7 GHz appears, as shown in Figure 41(b). A further increase in the injected optical signal induces an abrupt transition to a spectrum where only the larger-spaced spectral components are observed, Figure 41(c). This new spectrum shows that a new limit cycle has been established as can be seen by comparison with Figure 40(b). This new limit cycle has a larger resonance frequency than the original limit cycle. This resonance frequency continues to increase as the injection level is further increased.

We also observed abrupt spectral changes away from the region of chaotic dynamics where there was no significant power associated with the side modes. Figure 42 shows a set of optical spectra taken at a constant injection level while the offset frequency of the master laser is continuously made more negative. Figure 42(a) starts off the sequence as a continuation of the sequence in Figures 40 and 41 with optical excitation at the free-running frequency. At this even higher injection level, the laser is making the transition from the limit cycle above chaos to a new period-doubling region. Now, as the master laser is tuned to negative offsets, the laser makes a transition back to limit cycle dynamics, Figure 42(b). This is followed by an abrupt transition to a new limit cycle with a different resonance frequency, Figure 42(c), and Figure 42(d). In the limit cycle region, the laser exhibits essentially single longitudinal mode operation. There is a small change in the output power level, about 1%. These features are consistent with a saddle node bifurcation between two limit cycles. A transition between limit cycles has been observed previously in laser diodes under optical injection. However, this was for much weaker injection levels. The observation of such along with the observation of the period two to period three bifurcation at low injection levels shows that such transitions are possible over a wide range of injection conditions.

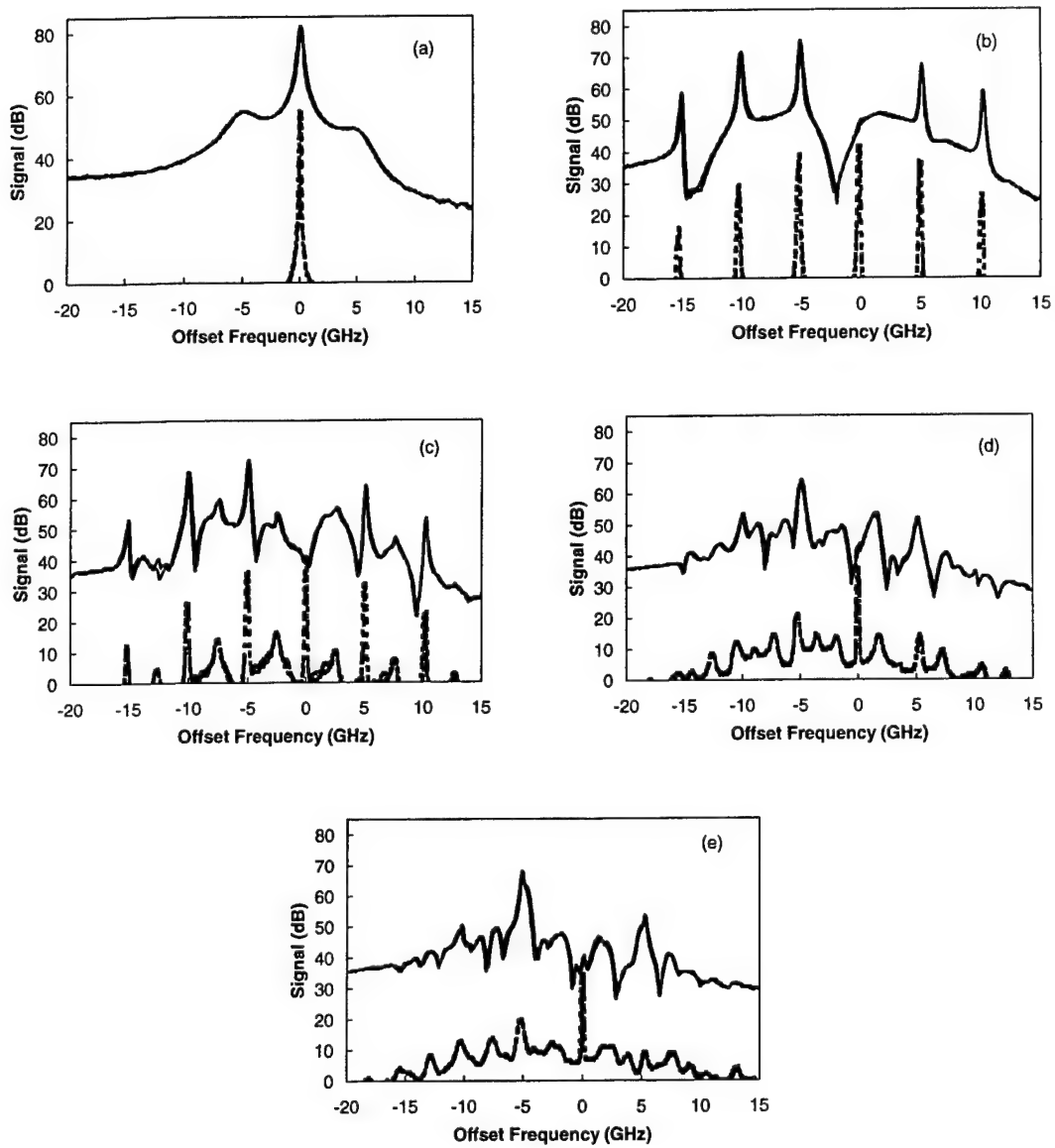


Figure 40. Spectra of the slave laser output (lower dashed curve) and the regenerative amplification of a weak optical probe (upper solid curve) under various injection levels. Frequency is relative to the free-running optical frequency of the slave and master lasers and signal level is relative to the noise background. (a) free-running operation, (b) limit cycle spectra at 5x and 4x the Hopf bifurcation level for the optical and regenerative amplification spectra, respectively, (c) period two spectra at 9x and 11x, (d) period three spectra at 15x and 14x, and (e) chaotic spectra at 17x and 16x.

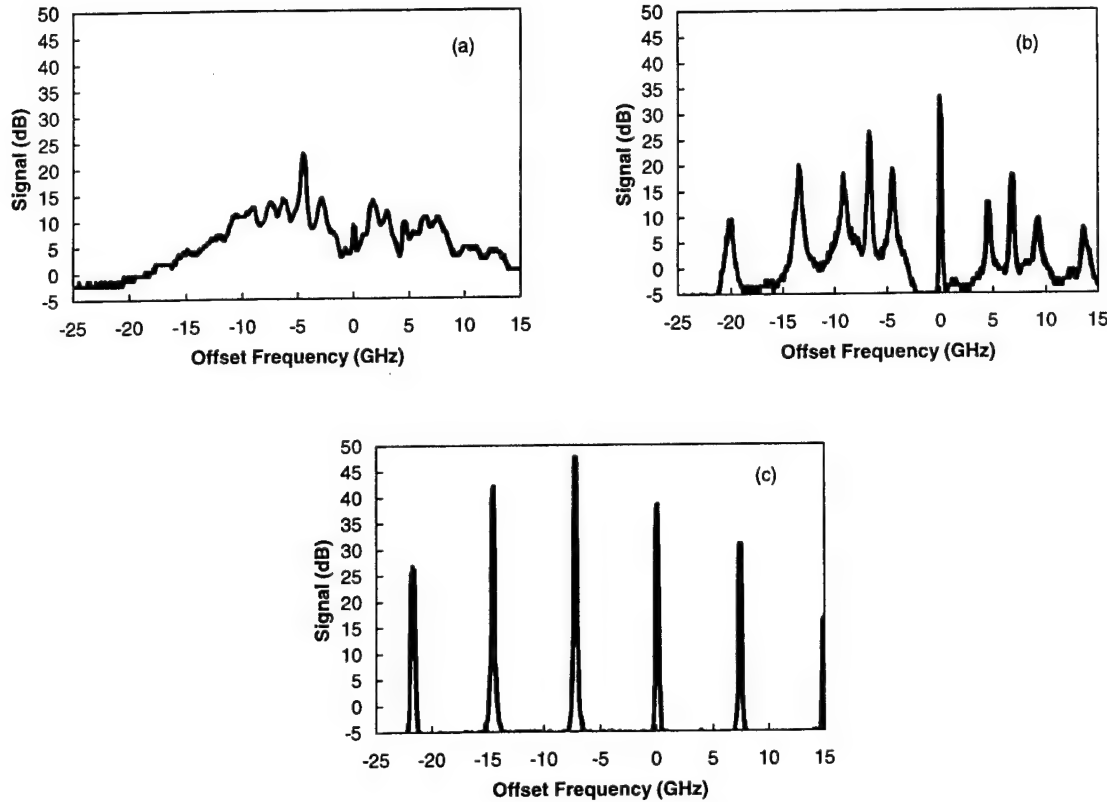


Figure 41. Spectra of the slave laser output under various injection levels. Frequency is relative to the free-running optical frequency of the slave and master lasers and signal level is relative to the noise background. (a) Chaotic spectrum at 32x the Hopf bifurcation level (b) limit cycle competition spectrum indicative of a saddle node of limit cycle bifurcation at 45x, and (c) limit cycle spectrum at 54x.

With reference to Figure 39, the thick solid line separating the chaos and limit cycle regions can be extended to more negative offsets. However, it does not follow the chaos, limit cycle transition line, but extends into the region of limit cycle dynamics. We observed the transition as long as we were operating at injection levels that were above the region of chaotic dynamics for excitation at the free-running frequency, but below excitation levels where period doubling was no longer observed at negative offsets. The bifurcation line appeared to end and it was possible to make a continuous transition from one side to the other by simultaneously changing injection level and offset frequency to trace a path around the transition line.

We confirmed that the abrupt transition out of chaos occurred independent of the existence of side modes by numerically calculating bifurcation diagrams using the experimentally determined laser parameters. Figure 43 shows the calculated effect of a weak side mode when the gain defect is 10^{-1} and 10^{-3} of the gain of the principal mode. With the larger gain defect, the results are essentially unchanged from the single-mode results. The circulating power of the laser remains in the principal mode at all levels of the injection parameter. However, when the gain defect is

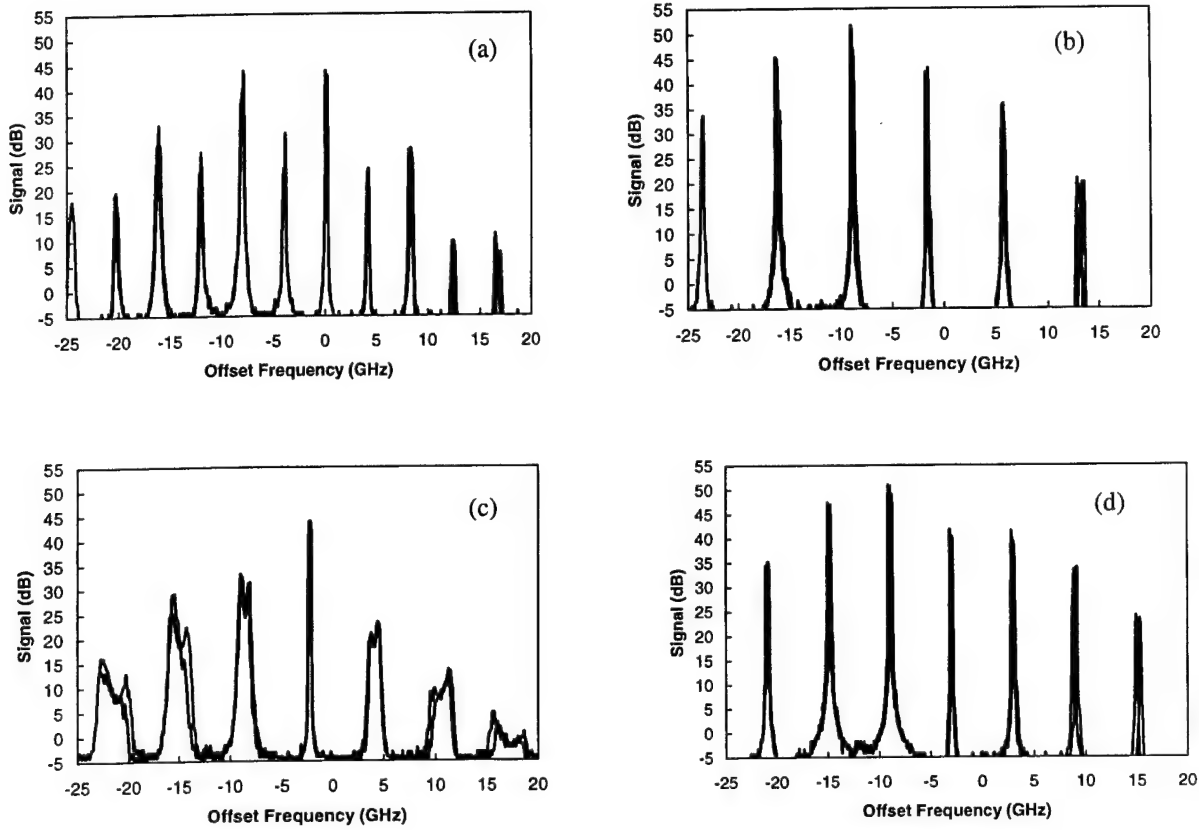


Figure 42. Spectra of the slave laser under optical excitation at the free-running optical frequency with an injection level approximately 70x the Hopf bifurcation level. Frequency is relative to the free-running optical frequency of the slave and master lasers and signal level is relative to the noise background. (a) Period-doubling spectrum with injection at the free-running frequency, (b) limit cycle spectrum with injection at an offset of -1.4 GHz, (c) limit cycle competition with injection at an offset of -2.4 GHz, and (d) new limit cycle with injection at an offset of -3.4 GHz.

reduced, a significant fraction of the output power can leak into the side mode, as we observe experimentally, and the details of the region of chaotic dynamics are significantly changed. The bifurcation diagram shows an induced mode hop for values of the injection parameter near 0.06 – 0.07 . While, we do not observe this with optical injection at the free-running frequency, we do observe this at positive detuning frequencies. Note that the average circulating power in the single-mode model dips below the free-running level over much of the region of chaotic dynamics. This means that the average carrier density is greater than the free-running value. At the higher carrier density the side mode gain is increased so that more power oscillates in that mode. When the average circulating power in the principal mode is greater than the free-running value, the model predicts single-mode operation.

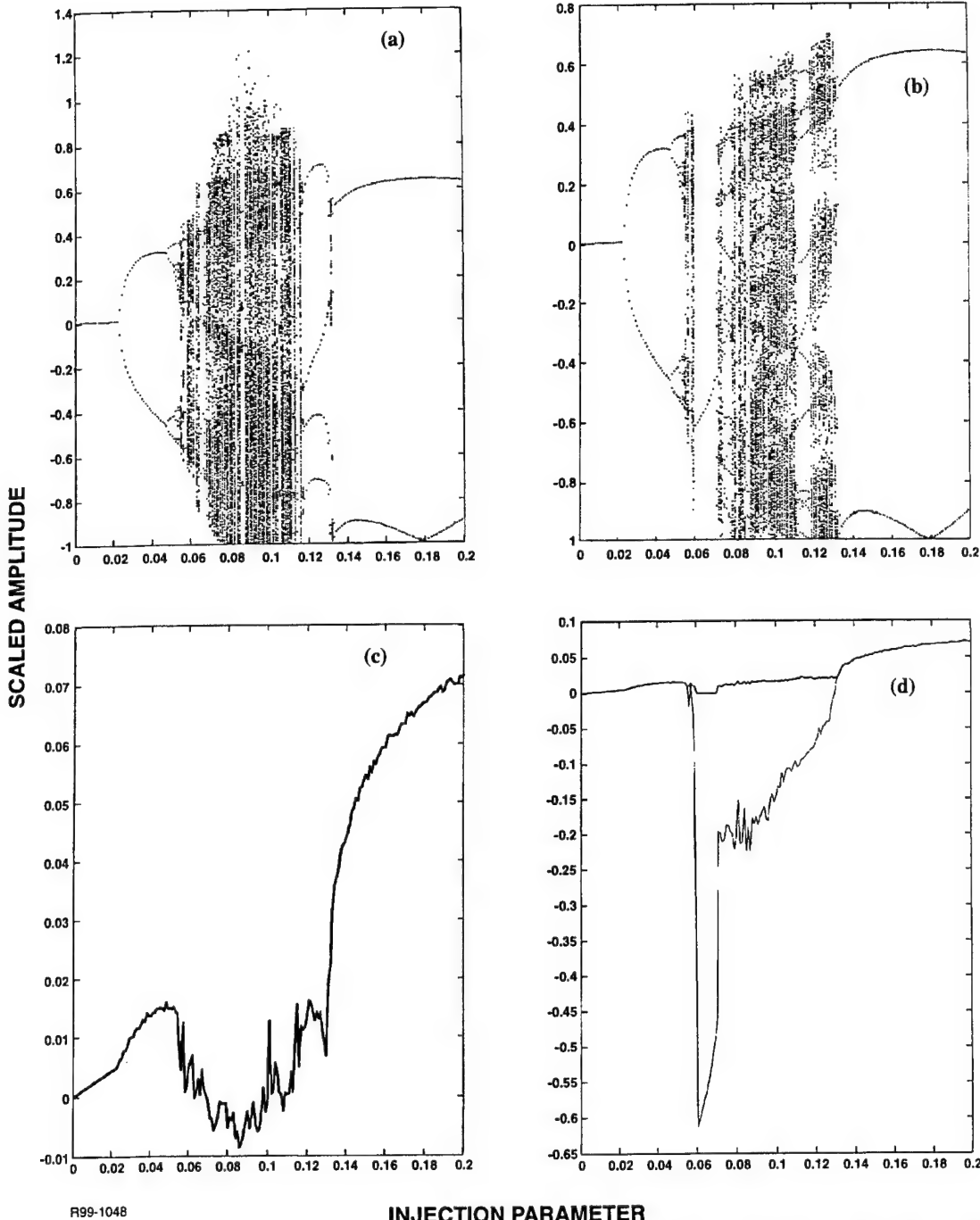


Figure 41. Calculated results when the laser model is modified to include a weak side mode.

Bifurcation diagrams (a) and (b) of the scaled extrema of the principal mode, $(a_x^2 + a_y^2)^{1/2} - 1$, and scaled average amplitude levels (c) and (d) of the principal mode (thin line) and both modes combined (thick line) for the laser with the parameters listed in the text and a pump parameter of 5.4. In (a) and (c) the gain defect of the side mode is 10^{-1} of the gain of the principal mode and the calculated result is essentially the same as the single-mode model. In (b) and (d) the gain defect is 10^{-3} and a significant fraction of the power leaks into the side mode in the region of chaotic dynamics.

With either gain defect, there is an abrupt change of dynamics back to a limit cycle at an injection level of approximately $\xi \approx 0.13$. The model shows only qualitative agreement with the experimental data but there are important similarities. The bifurcation diagram shows approximately a factor of seven increase in the injection parameter between the onset of unstable dynamics at the first Hopf bifurcation, just below 0.02, and the reestablishment of limit cycle dynamics above the region of chaotic dynamics. Because the injected power is proportional to the square of the injected power, this agrees well with the 45x-54x increase in power measured for the same change experimentally. The range of values for the different dynamics on the route into chaos agrees fairly well, too, though no period three dynamics are evident.

B. MODE VCSEL

The MODE VCSEL displayed qualitatively similar spectra under external optical injection. Figure 44 shows a set of spectra that are illustrative of the change in dynamics as the strength of the optical injection is increased. The injected optical power level is referenced to the output power by comparing signals of the collimated beams. This measure will somewhat overestimate the actual power coupled into the mode because the master and slave laser beams are not perfectly matched spatially and there are some losses at the collimating lens. The optical injection is at the free-running frequency of the VCSEL. When free running, the VCSEL shows single-frequency, constant-power operation, Figure 44(a). As the incident optical power from the master laser is increased, the VCSEL passes through a Hopf bifurcation and the output becomes unstable, oscillating at a frequency approximately equal to the relaxation resonance frequency of the free-running laser, Figure 44(b) with a relative injected power of -15 dB. Increasing the injected power further, the unstable output characteristic changes from limit cycle, with frequency components offset by the resonance frequency, to period doubling, with new features appearing at half-resonance intervals, Figure 44(c) with a relative injected power of -13 dB. These features become broadened with further increase in the injected optical power, Figure 44(d) with a relative injected power of -12 dB, until only a structured, broad feature remains, a signature of chaotic dynamics, Figures 44(e) at -11.4 dB and 44(f) at -10.5 dB. Further increasing the injected optical power results in a fairly sharp transition out of chaos back to limit-cycle spectra, Figure 44(g) at -8 dB. Note now that the resonance frequency is larger and that the strongest spectral feature is no longer at the injection or free-running frequency, but is offset by the injection-shifted resonance frequency. Increasing the injected power further results in a further shift of the resonance feature and a relative increase in size of the feature at the injection frequency, Figure 44(h) at -1 dB. Figures 45 and 46 summarize the frequency shift and the change in peak size with increasing injection. Above the region of chaotic dynamics, the resonance feature shifts approximately in proportion to the cube root of the injected optical power. While we did not observe this with the VCSELs, past work and modeling indicate that the VCSEL will re-establish stable, constant power output at injection levels higher than we could achieve. Such stable operation was achieved by detuning the master laser to negative offset frequencies, in agreement with modeling.

Relative to the SDL lasers, the MODE VCSEL shows a similar trend in that the dynamics passes from stable to limit cycle then to period doubling, chaos, and back to limit cycle as the injected power level increases. The range of chaotic dynamics is comparatively small, but the resonance frequency in the range of limit cycle dynamics appears to extend beyond 30 GHz at high

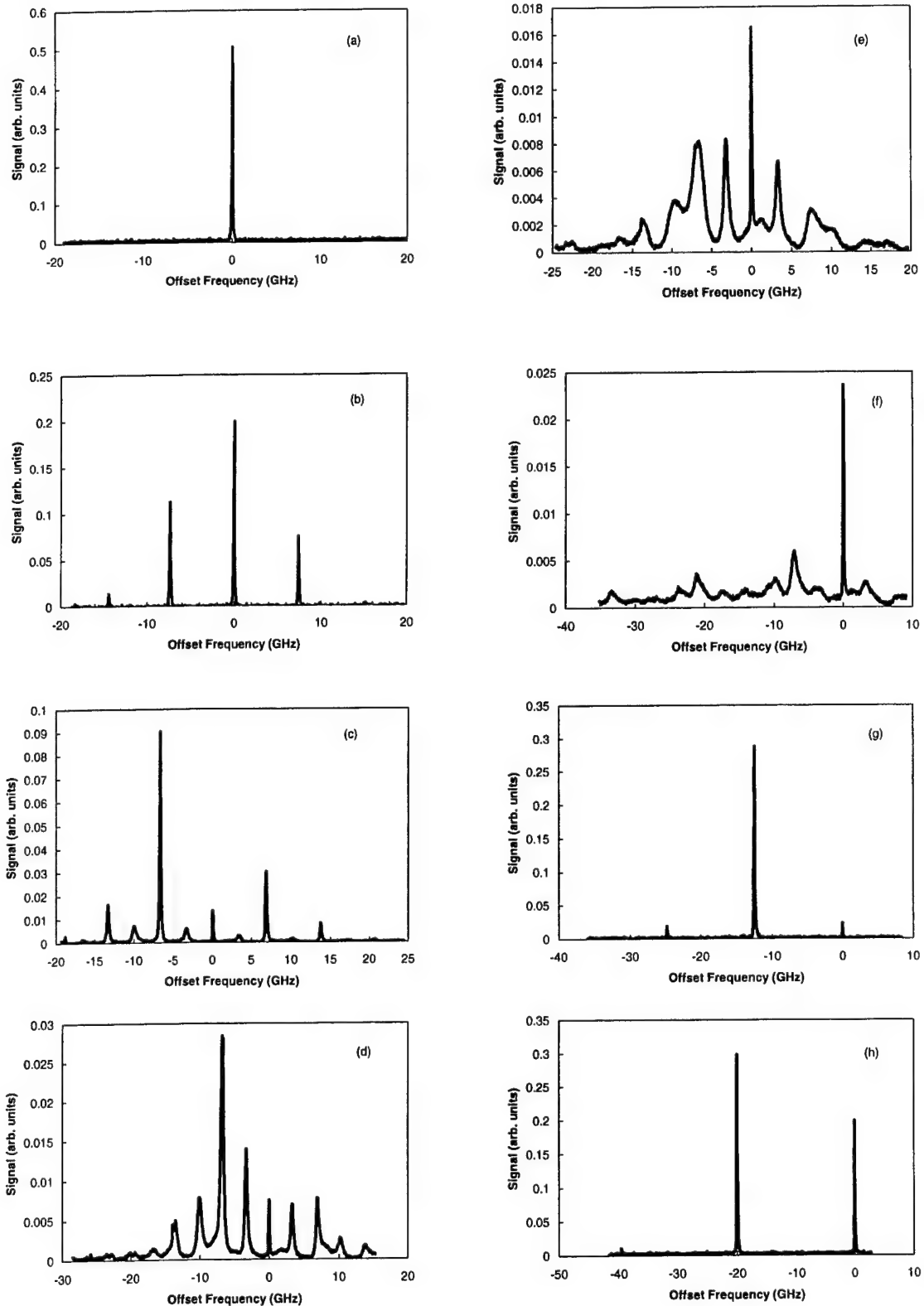


Figure 44. Spectra under strong optical injection (see text).

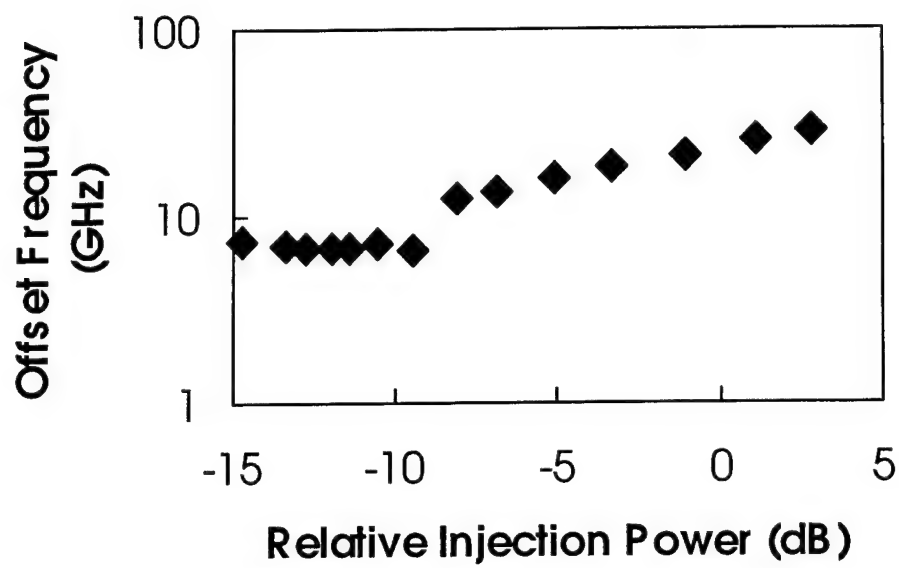


Figure 45. Resonance frequency of the laser under optical injection as a function of injected optical power. The injected power is relative to the output power of the free-running slave laser. The resonance frequency decreases slightly in the period-doubling and chaotic regions, then it increases monotonically at higher injection levels when the laser returns to periodic dynamics.

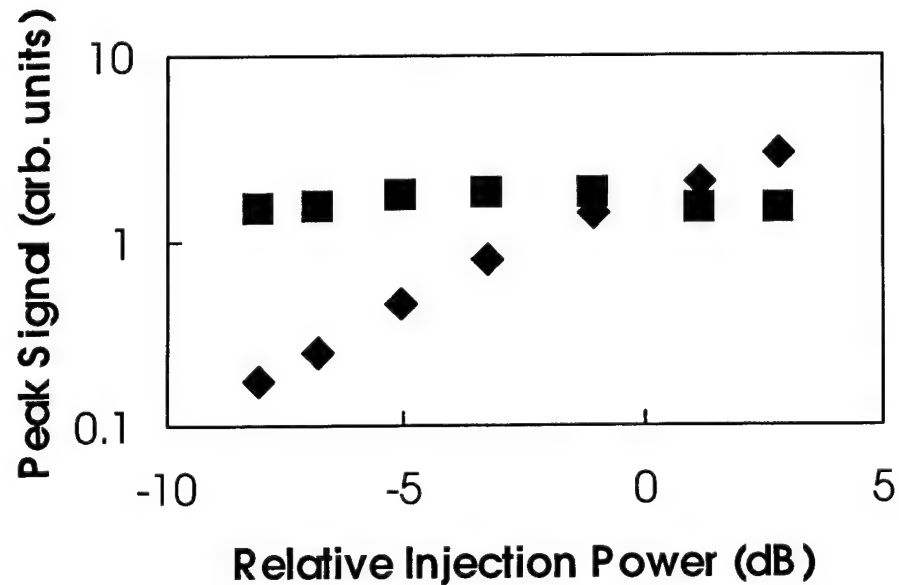


Figure 46. Size of the injection peak (diamonds) and the resonance peak (squares) as a function of injected optical power in the region of periodic dynamics above chaotic dynamics.

injection levels. This is significantly higher than could be achieved with the SDL lasers., and into the range of mm-wave oscillations of the photodetected signal.

C. Honeywell VCSEL

The spectra of the Honeywell VCSELs showed one key difference with respect to the other lasers studied. Under external optical injection, these lasers only displayed stable or limit cycle dynamics. The relatively low value of the linewidth enhancement factor was the key factor in determining this characteristic. To a lesser extent, the large value of the nonlinear gain rate, in comparison with the differential gain rate, also enhanced the stability of the system. The dynamics of the laser under strong optical injection were influenced by the presence of the weak, orthogonally polarized mode that had an optical resonance frequency 10-20 GHz above the lasing wavelength of the principal mode. Figure 47 shows a set of spectra taken as the power in the injected optical beam was increased. In this example, the injected optical beam is at the free-running laser frequency. Also, the polarization of the injected beam is rotated with respect to the free-running output so that a fraction, approximately 10%, is orthogonally polarized. Over two different injected power ranges, a significant fraction of the laser emission shifts to the orthogonally polarized mode. The first range, between 1.6-2.2 times the injected power required to drive the laser to unstable dynamics, occurs when the orthogonally polarized mode is shifted in frequency so that it becomes near resonant with a side peak of the optically injected laser. When there is significant excitation in the orthogonally polarized mode, the side peak or peaks in the original polarization become quite small. Further, there are no new sidebands in either polarization. This indicates that the two polarizations are both lasing in a stable manner. Note that the offset of the orthogonally polarized mode does not match the offset of the sidebands at the lower excitation energy, but becomes similar at the 2.2 times Hopf bifurcation injection level. This polarization first appears when its offset is approximately the same as a minimum in the regenerative amplification spectra of the free-running VCSEL. Therefore, the dynamics may be important in the polarization characteristics of the VCSEL at this excitation level. At higher powers, approximately 3.9 times the power that is required for the Hopf bifurcation, the orthogonally polarized mode has shifted in frequency so that it is near resonant with the injected beam. Again, there are no sideband features. The excitation has induced the VCSEL to lase at a new polarization, nearly orthogonal to the original polarization.

For both the MODE and the Honeywell VCSELs, sufficient optical power could be injected to push the frequency of the limit-cycle dynamics to 30 GHz, and beyond. These large offsets required injected optical power greater than the free-running output. In general, the VCSELs required higher relative input power levels. This is most likely due to the higher output coupler reflectivity of the VCSELs. Because of their short cavity length, on the order of 10 μm , the VCSELs are fabricated with output couplers of less than 2% transmission. The conventional edge emitters, on the other hand, are typically AR coated so that their reflectivity is less than 5%. Therefore, the coupling from the external laser into the gain medium is less efficient with the VCSELs.

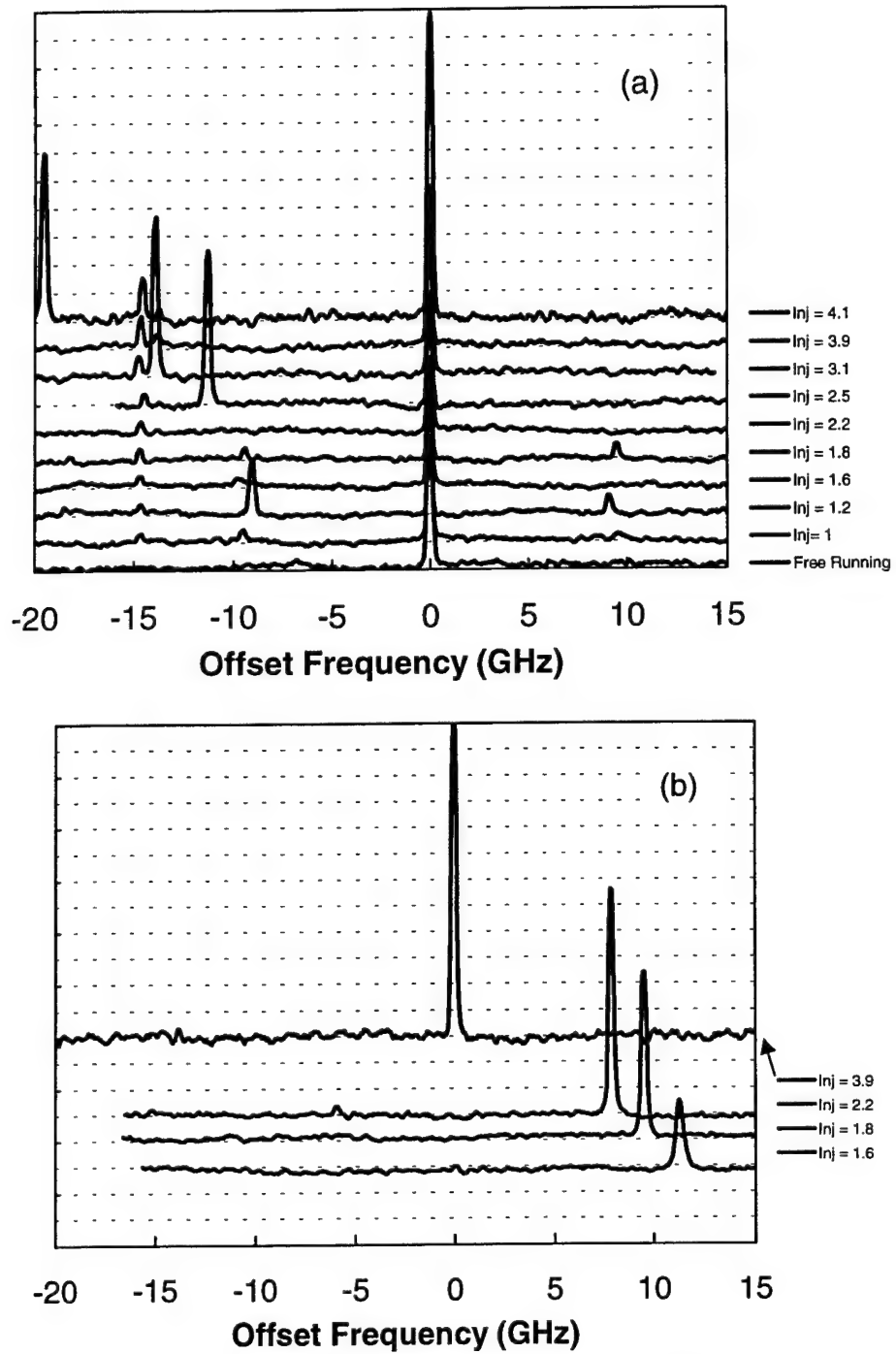


Figure 47. Optical spectra of the output of the Honeywell VCSEL under optical excitation at the free-running optical frequency. In (a) the observed signal is polarized parallel to the free-running mode and in (b) it is perpendicularly polarized. Injected power, relative to the power required to reach the Hopf bifurcation level, is given in the legend. There is a feature approximately 15 GHz below the strong peaks in most of the spectra that is an experimental artifact, a higher order mode of the scanning Fabry-Perot optical spectrum analyzer.

D. DFB Lasers

The last lasers that we investigated, the Alcatel DFB lasers suffered from neither the longitudinal mode hops of the SDL edge emitters or the polarization instability and operating frequency sensitivity of the VCSELs. The fiber-coupled configuration proved to be robust and stable and we were able to make a detailed mapping of the nonlinear dynamics as a function of the detuning and amplitude of the injected optical field. This allowed us to make a more thorough mapping of the nonlinear dynamic of a single mode laser subject to external optical injection. The mapping is made by relating a particular output dynamics to the spectral features displayed at a given injection level and offset frequency. Figures 48-53 show sets of spectra observed at different offset frequencies as the injected optical power is increased. Each set is meant to illustrate the kinds of spectral changes that are observed as the dynamics changes. Each set of spectra consists of optical spectra in the left column and regenerative amplification spectra in the right column, with the two spectra in the same row taken at approximately the same injection level. The injected signal is given in terms of a photodetector voltage that is proportional to injected power. Offset frequency is relative to the free-running optical frequency of the slave laser and output power as a function of offset frequency is shown on a logarithmic scale. Most of the spectra show data from two scans overlaid. Because there is some jitter during a scan, the spectral features do not precisely overlap. For the results presented here, the laser was operated at twice the threshold frequency. Here, the relaxation resonance frequency of the free-running laser is approximately 4.7 GHz.

Figure 48 shows the transition from free-running output to limit cycle dynamics as the injected signal is increased when the master laser is tuned to the free-running optical frequency of the slave laser. Both the free running optical and regenerative amplification spectra show the weak, broad features associated with the relaxation resonance frequency. As the injected optical signal is increased, the damping on this resonance decreases and the sidebands become stronger until the Hopf bifurcation is passed and the laser output becomes unstable. Because there are no absolutely abrupt changes as a parameter is smoothly changed, criteria had to be developed to define a change in dynamics. We noted that in the regenerative amplification spectra that a narrow dip and peak structure developed at the master laser injection frequency. It is clearly visible at the highest injection level and is barely showing at the next lower injection level. The peak and dip reach a maximum in between these two injection levels. Recall that the regenerative amplification spectrum measures the small signal optical gain as a function of offset frequency. A dip and peak around an injection feature indicates that the perturbing probe is having a strong effect on the spectral feature locked to the strong signal from the master laser. This is consistent with a transition in the locking characteristics. Because it is occurring as the optical spectrum is showing a change from weakly damped relaxation resonances to simultaneous oscillation at several optical frequencies, we interpreted the maximum in the peak and dip as the Hopf bifurcation point. Associated with this transition were sidebands approximately 15-20 dB below the resonant, locked feature. Therefore, we used the criterion that a spectral feature had to be approximately no more than 20 dB below the strongest spectral feature for its associated dynamics to be the characteristic dynamics.

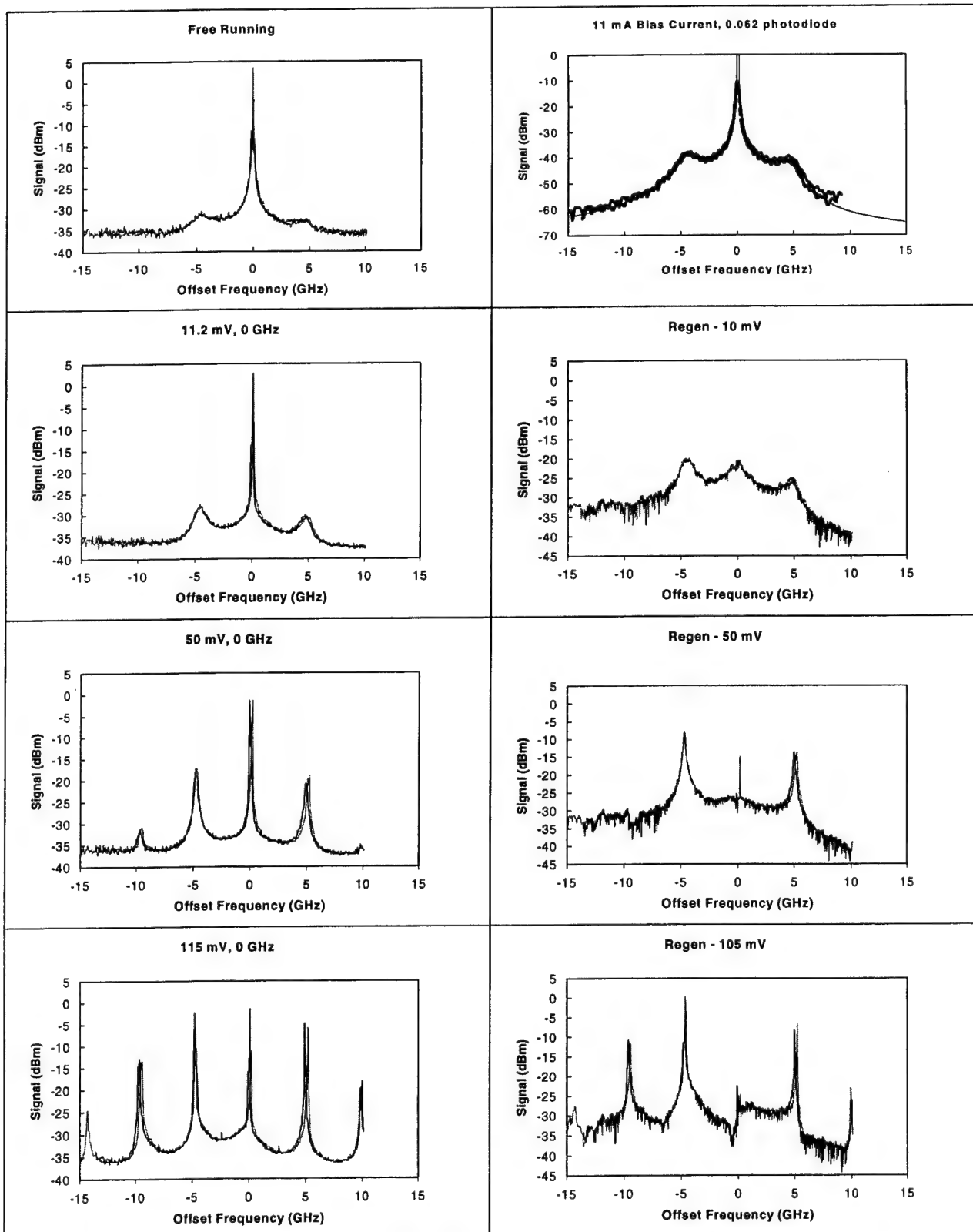


Figure 48. Spectra with injection at the free-running optical frequency showing the transition from stable to limit cycle dynamics.

This criterion can be used to analyze the dynamics associated with the spectra shown in Figure 49. Here, the optical frequency of the master laser is offset by 2 GHz. At the weakest injection level, the optical spectrum shows side peaks due to regenerative amplification of the master laser signal and four-wave and multiwave mixing between the master laser and unlocked slave laser frequencies. The multiwave mixing becomes more pronounced as the injection level is increased, as does the enhancement of the broad features originally associated with the relaxation resonance frequencies. These latter features dominate the spectrum as the laser makes a transition from unlocked to locked but unstable output at the highest injection level. In the unstable locked output, there are weak spectral features around the strongest spectral peaks that indicate that another frequency is present in the dynamics. However, this component is very weak and we use the 20 dB criterion to call this a limit cycle spectrum. Below locking, however, both the frequency associated with the difference between the injection signal and the unlocked oscillation frequency of the slave laser and the frequency associated with the free-running relaxation resonance make strong contributions to the spectral characteristics. This is not the case for an offset frequency of -2 GHz where the enhancement of the relaxation resonance features is considerably less. A spectrum with two incommensurate frequencies is associated with quasiperiodic dynamics.¹⁶ Using the 20 dB criterion, the spectra indicate that below locking the laser is near the boundary of a transition to quasiperiodic dynamics.

Figure 50 continues the progression of Figure 49 to higher injection levels. The weak features about each strong spectral peak become strong and grow in offset as the injection power is increased. The laser, therefore, makes a transition from limit cycle to quasiperiodic dynamics. Eventually, the broad continuum grows until only a few spectral features are evident. This spectrum indicates that a transition chaotic dynamics has probably occurred. This connection can be made firmer by calculating the characteristic exponents that describe the sensitivity of the dynamics to perturbations, the so-called Lyapunov exponents. Past calculations have shown that spectra like those at the highest injection level of Figure 50 are associated with chaotic dynamics.¹⁷ The observation of quasiperiodic motion in Figure 50, and possibly Figure 49, occurs at injection conditions where the SDL laser experienced a mode hop. This will be seen to be consistently true at other injection conditions. At still higher injection levels, the laser makes a transition back to strong, narrow spectral features as shown in Figure 51. The first spectral features to appear to show period two, or perhaps period four, dynamics coexisting with a broad chaotic continuum. Further increase in the injected power causes a change to a spectrum associated with period three dynamics, two equally spaced features between relatively stronger components. The intermediate features gradually decrease and the laser reestablishes limit cycle dynamics. At still higher injection levels, the laser can be expected to reestablish stable, locked operation. However, we feared that we might damage the laser and did not attempt to observe this transition at this offset frequency.

The clear observation of quasiperiodic motion in the spectral characteristics of Figure 50, and possible Figure 49, confirms theoretical predictions and numerical calculations. This motion occurs under optical injection conditions where the SDL laser was induced to hop to a different longitudinal mode. The quasiperiodic motion occurs with an increase in the average carrier density. This allows one of the other longitudinal modes of a conventional edge-emitting, Fabry-Perot lasers to become the dominant mode. With a DFB laser, like the one used here, the loss for each of the side modes is sufficiently enhanced so that the laser threshold is not crossed.

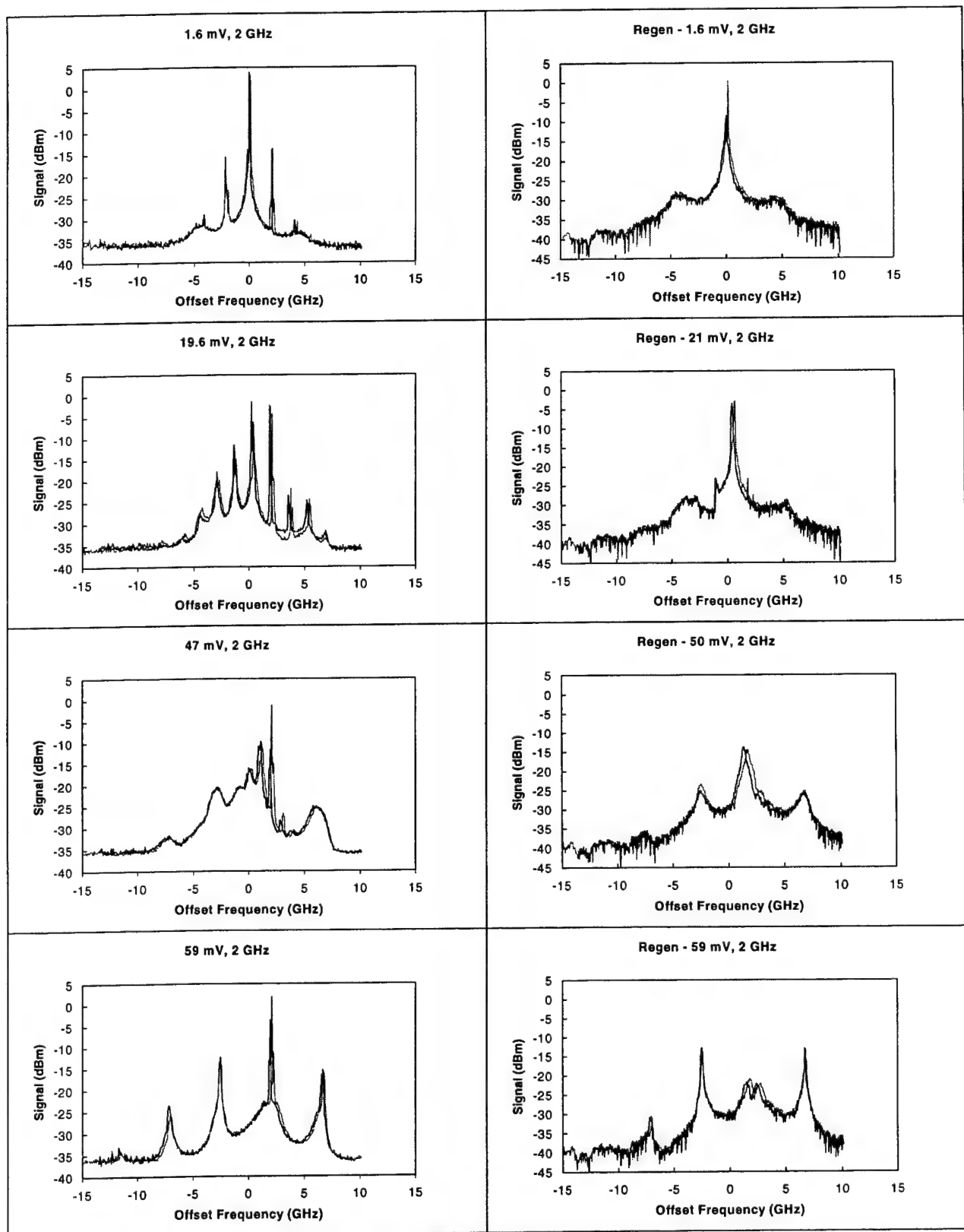


Figure 49. Spectra with injection at an offset of 2 GHz from the free-running optical frequency showing the transition from unlocked to limit cycle dynamics.

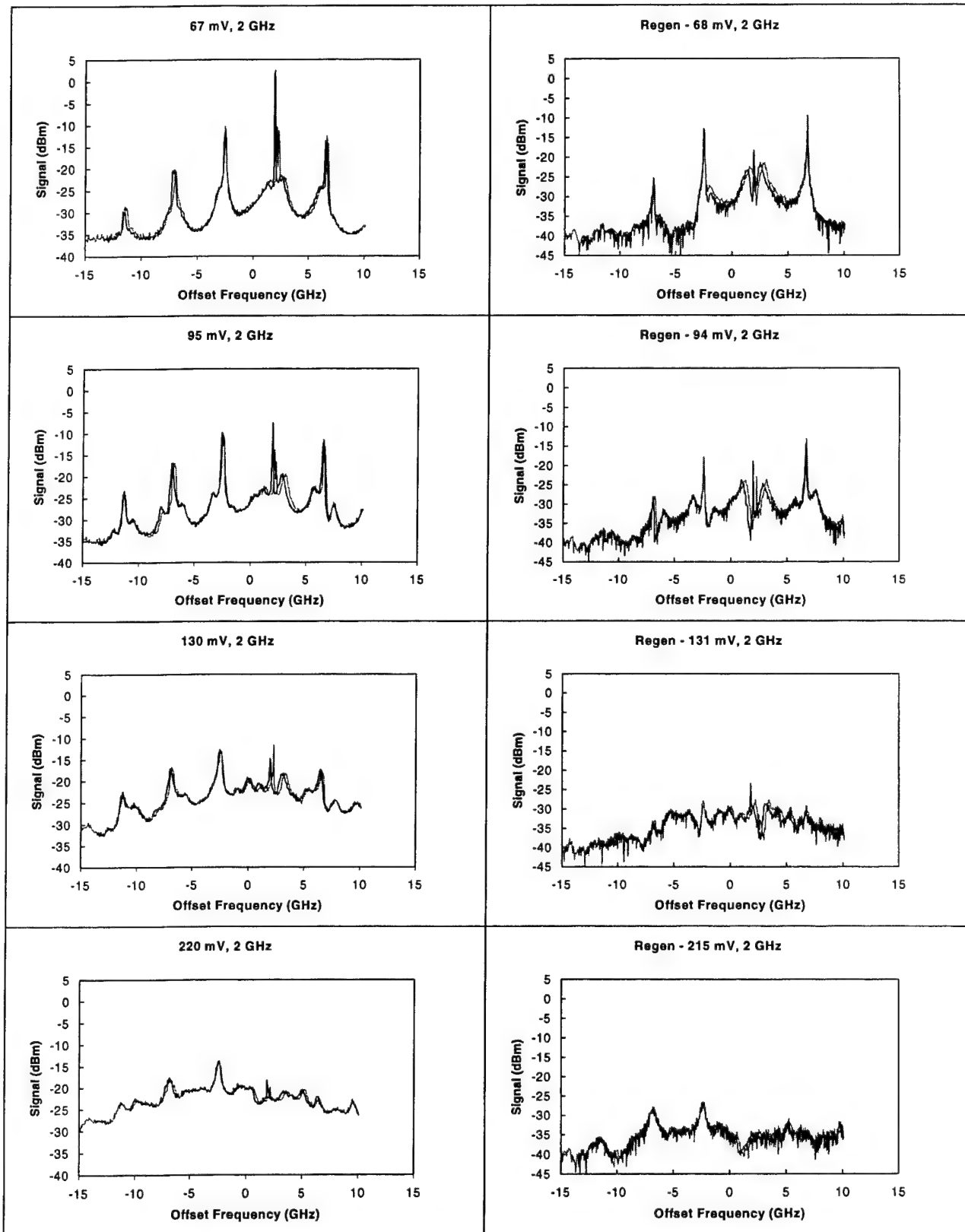


Figure 50. Spectra with injection at an offset of 2 GHz from the free-running optical frequency showing the transition from limit cycle to chaotic dynamics.

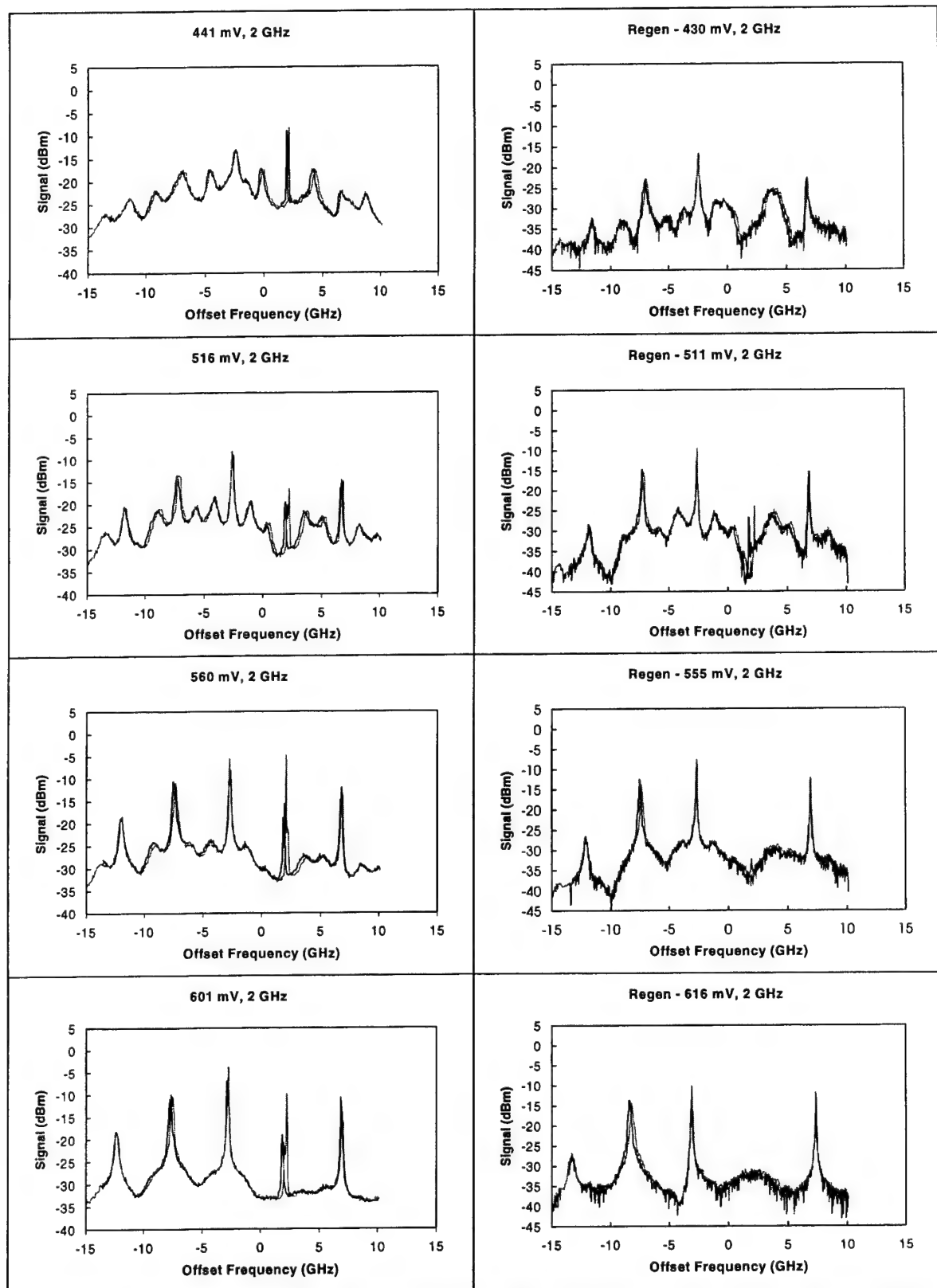


Figure 51. Spectra with injection at an offset of 2 GHz from the free-running optical frequency showing the transition from chaotic to limit cycle dynamics.

The mapping of the SDL lasers in Figure 39 shows another mode hopping region, at negative offset frequencies, for injection levels below the transition to stable, locked dynamics. Figures 52 and 53 show the changes in dynamics as the injection level is increased at an offset frequency of -6.1 GHz. As the optical injection is increased, the oscillation frequency of the unlocked laser is pushed to positive offset frequencies and the features associated with the relaxation resonance frequencies are enhanced as they become sub-resonant with the injection offset. This effect has been termed subharmonic resonance and yields period two dynamics. The locking of the resonance with the offset is broken as the injection is further increased and a spectrum with double peaked features offset from the injection frequency occurs, as shown by the highest injection optical spectrum of Figure 52. The double-peak spectrum becomes a period four spectrum as the injection level is increased further. The periodic features gradually diminish in strength as the spectrum appears to separate into two components at higher excitation levels. One component is a series of equally spaced features that is pulled towards the injection frequency as the transition to stable locked operation is approached. The other is a broad featureless continuum at positive offset frequencies. This feature becomes weaker, but continues to be observed up to the transition point for stable locked operation.

The spectral details in Figures 52 and 53 give clues about the output characteristics. First, the pushing of the unlocked oscillation frequency to positive offsets is consistent with an increase in the average carrier density of the gain medium. The increased carrier density provides added gain to the other longitudinal modes, providing the push for one to cross the lasing threshold. Second, the enhancement of spectral features as the offset between injection frequency and unlocked oscillation frequency becomes commensurate with the frequency associated with the relaxation resonance feature shows that the periodic motion observed in the spectra are special states of the more general quasiperiodic motion. The enhanced features are consistent with resonances between the natural and driving frequencies of the system, called Arnold tongues. Without the resonant enhancement, the quasiperiodic motion is often suppressed as one or the other frequency component dominates. Third, the two component nature of the spectra below the stable locking threshold points to the possible existence of multiple attractors in the region of an operating point. The spectral component consisting of equally spaced features near the injection frequency is consistent with limit cycle motion producing multiwave mixing. The period of the limit cycle increases to infinity as the transition to stable operation is reached. The other spectral component, broad and featureless, is consistent with a chaotic attractor. The existence of multiple attractors has been predicted to be important in the generation of chaotic dynamics in semiconductor lasers subject to external optical injection.

We have combined spectra such as those in Figures 48-53 to produce a mapping of the observed dynamics. While spectra that show stable or periodic dynamics can be interpreted in a straightforward manner, the quasiperiodic and chaotic spectra are more difficult to distinguish. The presence of spontaneous emission noise and, potentially, multiple competing attractors means that broadening is not enough to distinguish between periodic motion on multiple attractors, quasiperiodic motion with broadening due to noise and true chaotic dynamics. Therefore, until detailed numerical work can be done to compare with the experimentally measured spectra, spectra indicating complex dynamics will not be distinguished.

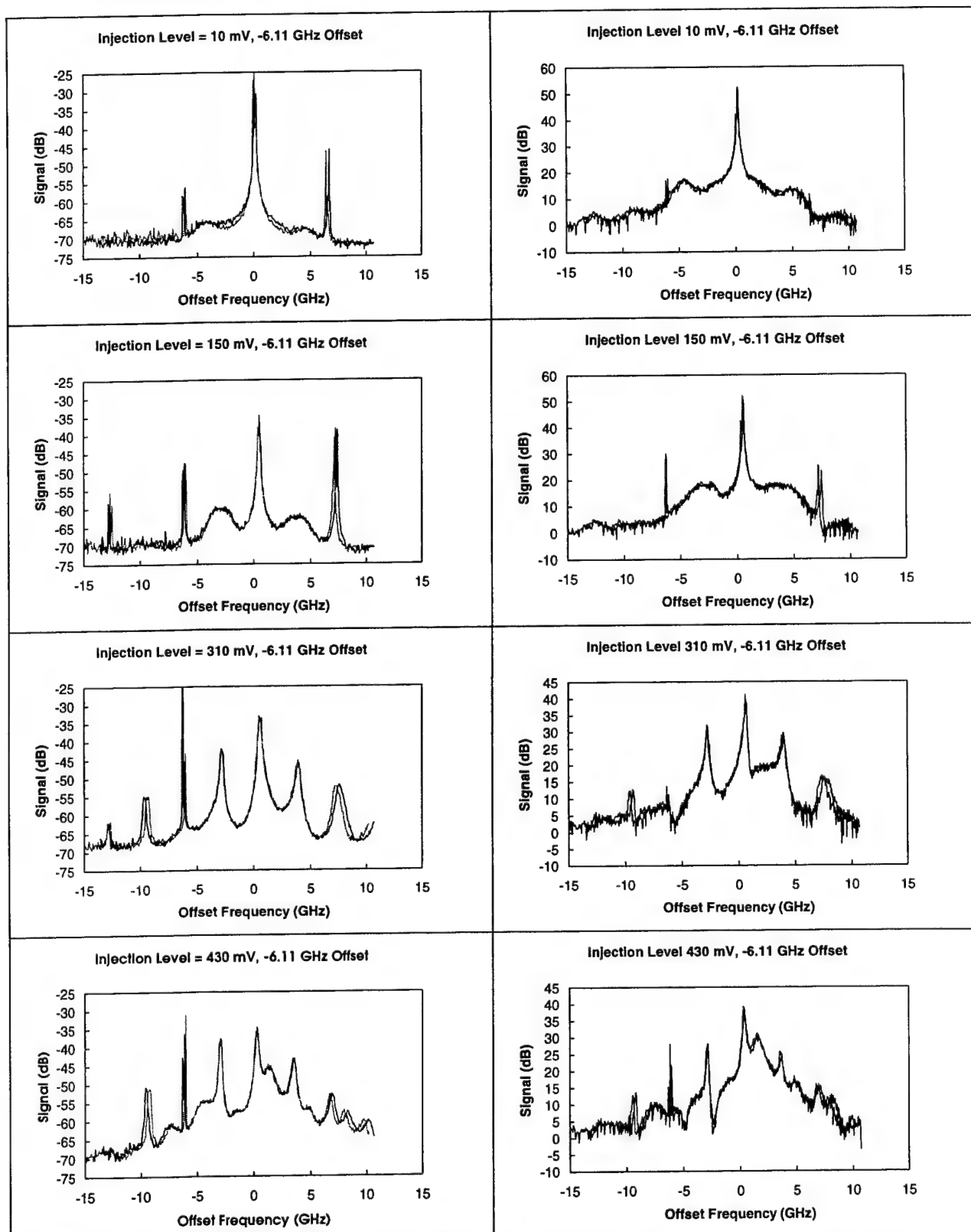


Figure 52. Spectra with injection at an offset of -6.1 GHz from the free-running optical frequency showing the transition to quasiperiodic dynamics.

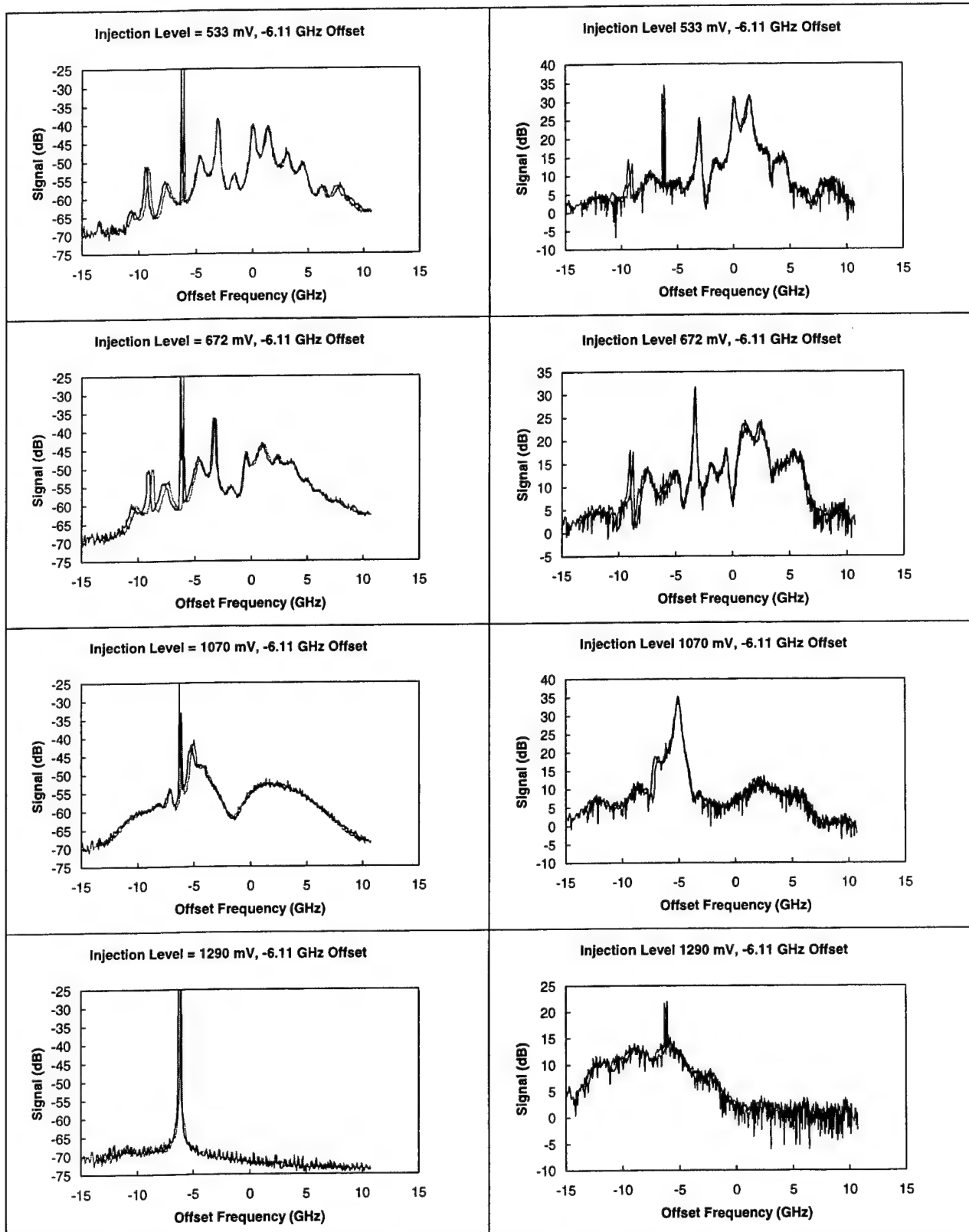


Figure 53. Continuation of Figure 52, with injection at an offset of -6.1 GHz from the free-running optical frequency, showing the transition stable injection locking.

Figure 54 is a mapping of the observed dynamics based on interpretation of spectra like those described above. The ordinate of the map is proportional to the square root of the injected optical power, the injected field amplitude, and the abscissa is the offset frequency of the master laser with respect to the free-running frequency of the slave laser. Boundaries of the regions of stable and periodic dynamics are shown. Diamonds mark the saddle node boundary between stable locked and unlocked dynamics, squares mark the Hopf bifurcation boundary between stable locked and limit cycle dynamics, triangles mark the boundaries of regions of period two dynamics and circles mark the boundary of period four dynamics. The three shaded regions mark the areas where more complex dynamics are observed. Within the regions of complex dynamics are small regions of periodic dynamics that are not marked for clarity. This map bears a strong similarity to the old mapping of dynamics of the SDL laser. As expected, because of the smaller

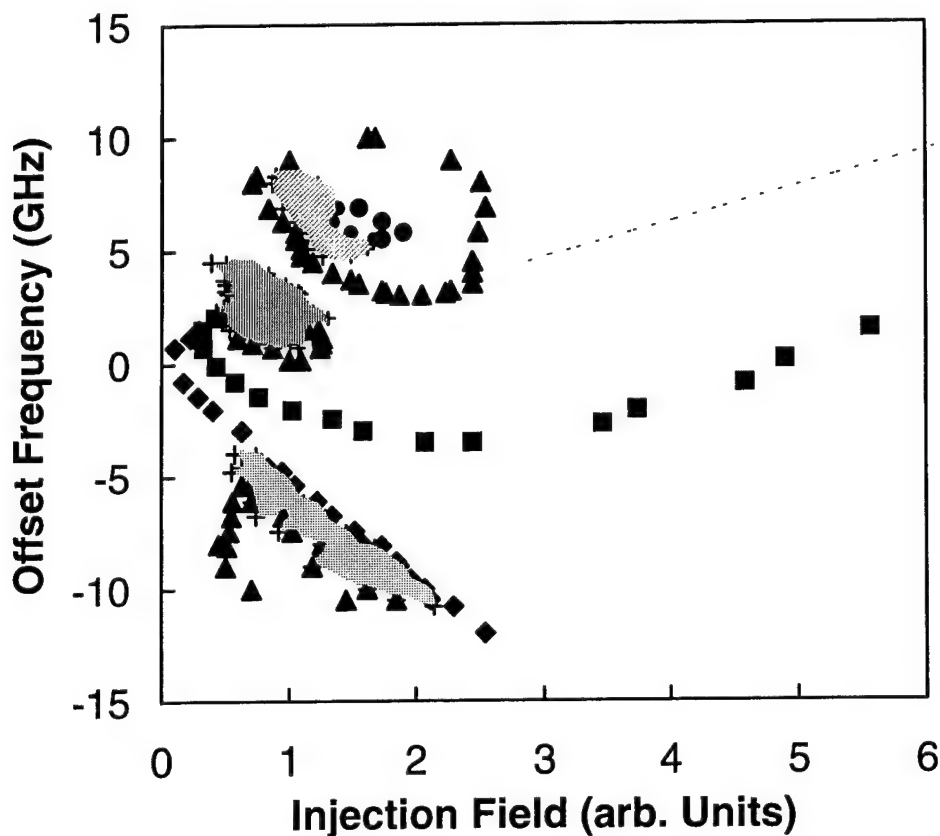


Figure 54. Mapping of the observed dynamics based on the experimentally measured spectra of the DFB laser under optical injection when biased at twice the threshold current. The injection field is proportional to the square root of the injected optical power. The diamonds mark the saddle node bifurcation between unlocked and stable locked operation, and the squares mark the Hopf bifurcation between stable and limit cycle operation. The triangles bound regions of period two operation. Within the period two regions are regions of complex dynamics marked by the shaded lines and crosses and a region of period four operation that is bounded by the circles. The dashed line marks the calculated asymptote of the Hopf bifurcation at high injection levels.

linewidth enhancement factor and larger ratio γ_p/γ_n , the nonlinear dynamics is more tightly bounded. From this map it is clear that all regions of periodic dynamics with period two or larger have an associated region of complex dynamics. The higher period oscillatory dynamics represent resonances of the competing frequencies initially associated with the offset between the master and slave laser optical frequencies and the relaxation resonance frequency. Both the offset and dynamic resonance frequencies change as the optical injection is increased. Therefore, the mapping displays the regions of higher order periodic, quasiperiodic and chaotic dynamics.

We can compare the observed dynamics with calculated dynamics by relating the injected field to the injection parameter, ξ , that we use in the calculations. Note that the saddle node bifurcation line shows a linear dependence with injected field, as expected from both a linearized a full nonlinear analysis. Using this line of data as a reference, the injection field can be related to the injection parameter by multiplying by approximately 0.22. In Figures 55-57 we show bifurcation diagrams calculated for different offset frequencies showing extrema in the field amplitude as a function of the injection parameter. We used the experimentally measured parameters for the calculations, choosing $b = 3$ and, arbitrarily, $b' = 1.2$. The value of b is below the best fit based on the weak injection characterization, but within the experimental uncertainty. The agreement between theory and experiment is very good showing that the model reproduces the experimentally observed characteristics. We should note that we were never able to observe periodic dynamics of period greater than six, a weak period three bifurcation of a period two feature, and were never able to observe period doubling beyond period four. The DFB laser always broke out of the resonance condition back into the more general quasiperiodic, or possibly chaotic, condition. The bifurcation diagrams do show higher periodic dynamics, but these regions cover a very narrow range of injection levels. Possibly the inherent noise in the real semiconductor laser system is sufficient to make these regions indistinguishable from more complex dynamics. Possibly, the noise induces hops between multiple attractors that may occupy different regions of phase space at these excitation levels. Theoretical work has predicted that multiple attractors are an inevitable part of the complicated dynamics of semiconductor lasers around regions of chaotic dynamics.

Three different semiconductor laser types have now been compared with the coupled equation model. All display the dynamic characteristics predicted by the model. Relative to our previous work, the work here shows that, in general, the saturation effects on the complex gain have a different proportionality constant than does the differential gain component, in other words, $b' \neq b$. The influence of non-lasing side modes can be included, qualitatively at least, by the addition of an additional field amplitude equation, with this equation coupled to the original set through the carrier density equation. When such an equation is included with a gain defect that is on the order of 10^{-3} of the gain of the principal mode, we observe leakage of a significant fraction of the laser output to the side mode. The leakage typically occurs when the injection laser induces output characteristics with an average output power below the free running power of the principal mode. This often happens in regions of quasiperiodic or chaotic output. This level of gain defect is consistent with the observed side mode characteristics of the SDL lasers and the orthogonally polarized mode in the VCSEL. In the DFB laser, all side modes are sufficiently suppressed that there is no appreciable leakage out of the principal mode and we were able to produce a mapping of the regions of nonlinear dynamics displayed by a semiconductor laser under optical injection.

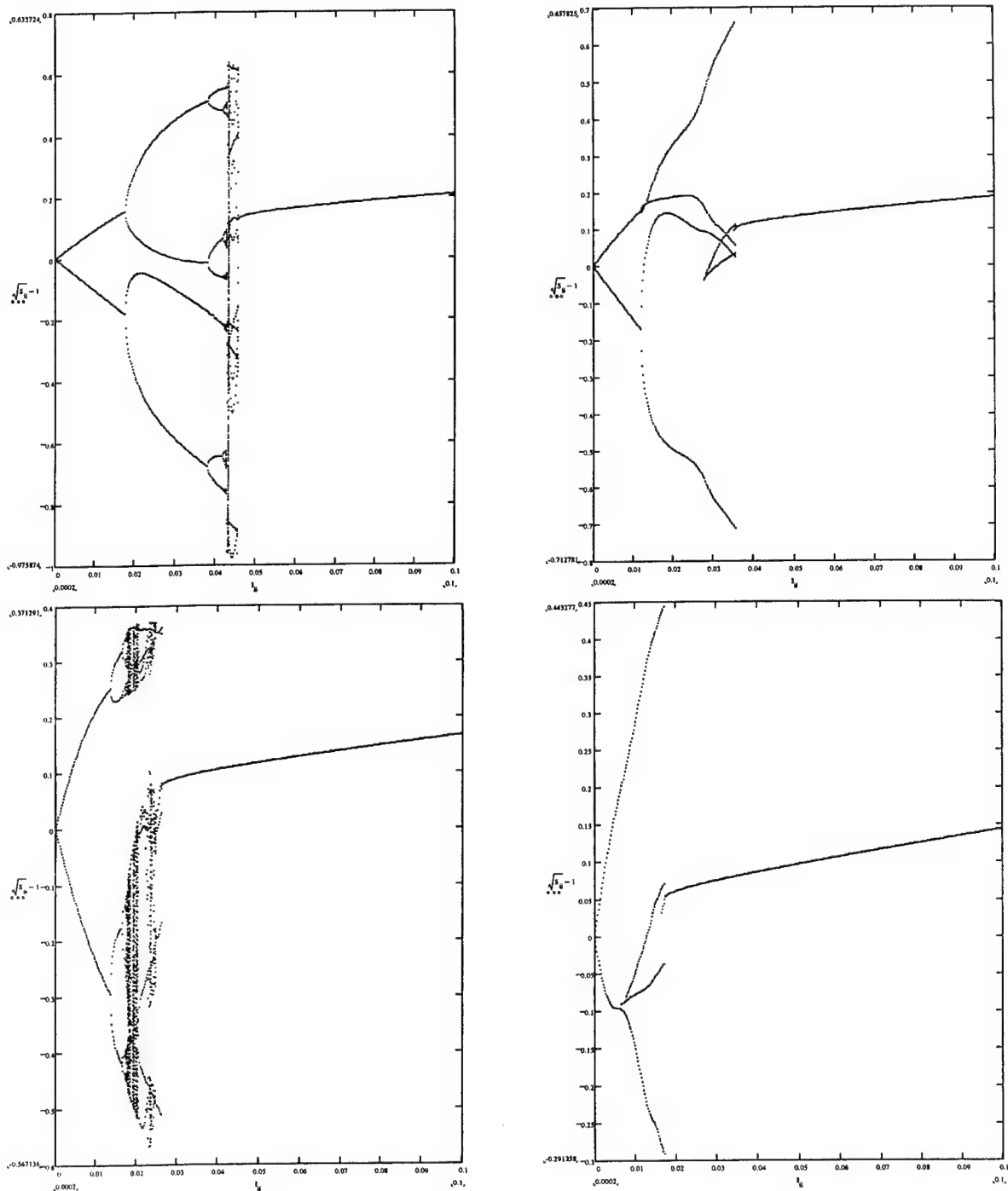


Figure 55. Bifurcation diagrams showing extrema of the optical field as a function of the injection parameter using the experimentally measured values of the Alcatel DFB laser for the dynamic parameters. The offset frequency of the master laser is -10 GHz (upper left), -8 GHz (upper right), -6 GHz (lower left), and -4 GHz (lower right). The injection parameter is varied from 0.0 to 0.1 in the plots. These calculations should be compared with the experimentally measured mapping of Figure 54.

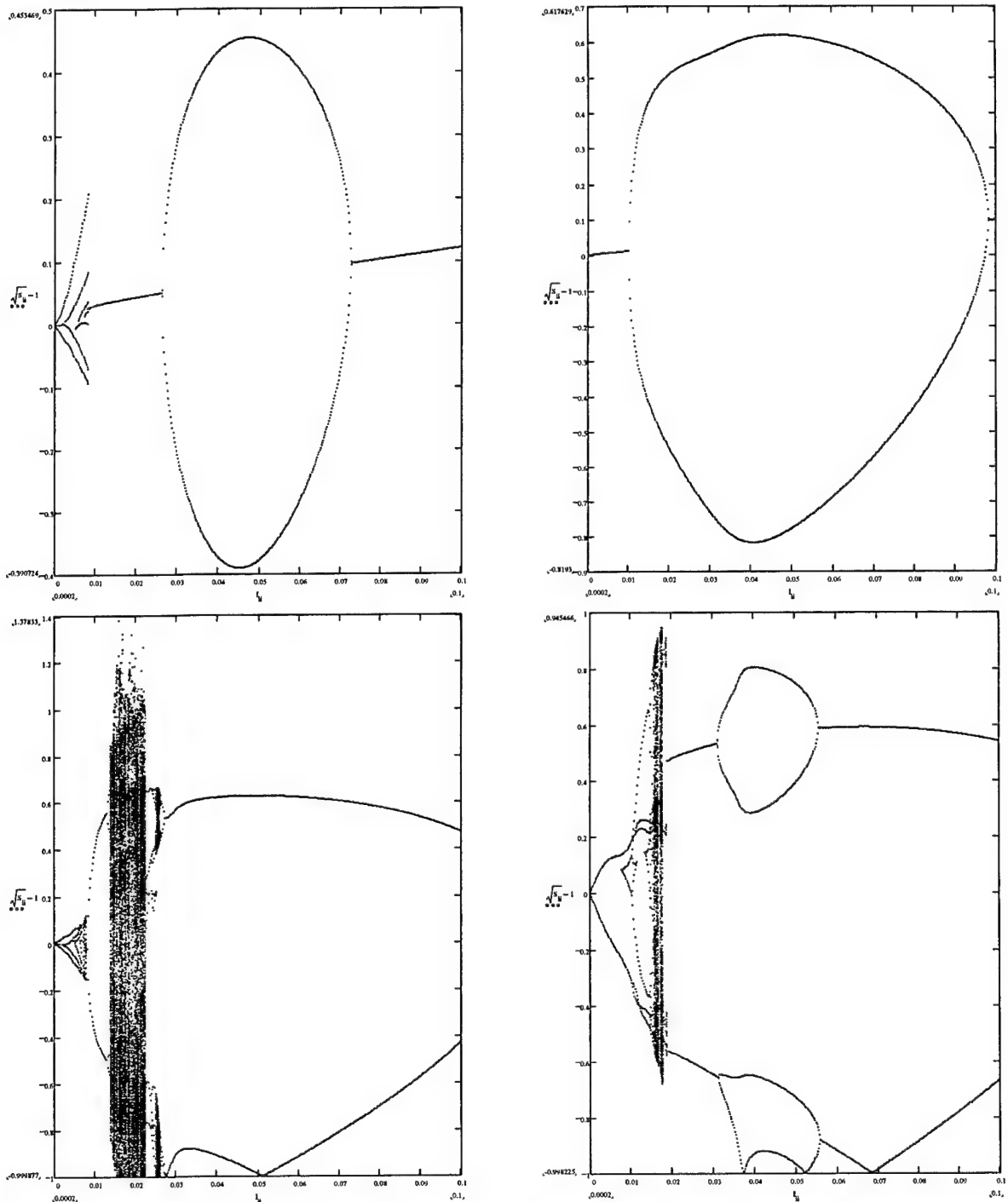


Figure 56. Bifurcation diagrams showing extrema of the optical field as a function of the injection parameter using the experimentally measured values of the Alcatel DFB laser for the dynamic parameters. The offset frequency of the master laser is -2 GHz (upper left), 0 GHz (upper right), 2 GHz (lower left), and 4 GHz (lower right). The injection parameter is varied from 0.0 to 0.1 in the plots. These calculations should be compared with the experimentally measured mapping of Figure 54.

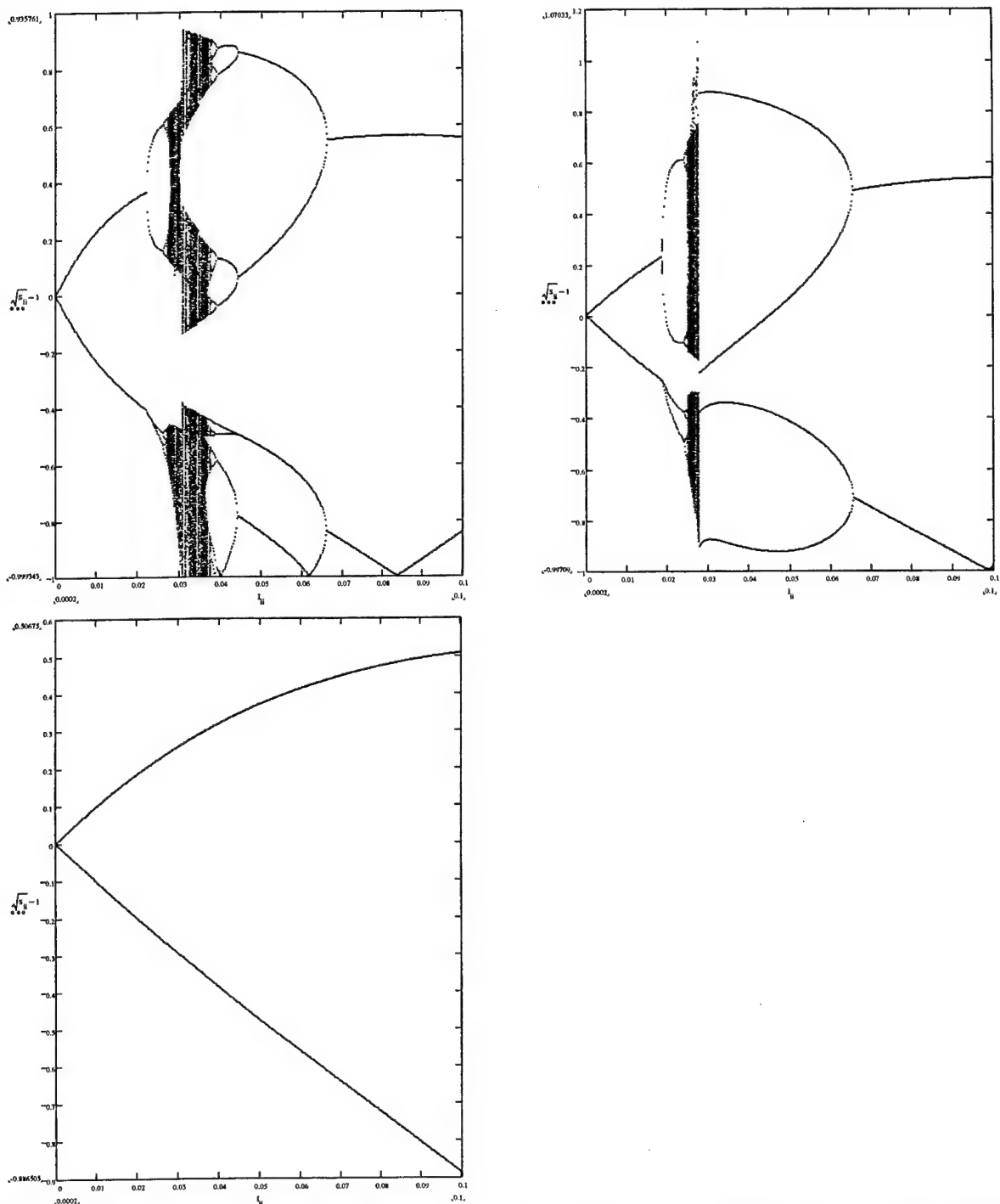


Figure 57. Bifurcation diagrams showing extrema of the optical field as a function of the injection parameter using the experimentally measured values of the Alcatel DFB laser for the dynamic parameters. The offset frequency of the master laser is 6 GHz (upper left), 8 GHz (upper right), and 10 GHz (lower left). The injection parameter is varied from 0.0 to 0.1 in the plots. These calculations should be compared with the experimentally measured mapping of Figure 54.

6. DOUBLE-LOCKED LASER OPERATION

The mappings of the nonlinear dynamics in Figures 39 and 54 show that external optical injection of a semiconductor laser can induce a variety of output characteristics, including oscillatory dynamics due to an induced instability in the coupling between the gain medium and the circulating optical field. For moderate injection levels, above the range where chaotic dynamics is observed but below the level where the system reestablishes stable injection-locked operation, the laser displays periodic dynamics. The resonance frequency of the periodic dynamics depends on the strength of the injected optical beam and the detuning between the optical frequencies of the injected beam and the free-running laser. We demonstrate here that by adding a weak modulation current reference to the bias of a semiconductor laser undergoing such optical injection, the modulation frequency can be locked to that of the current modulation with excellent noise characteristics. Further, we investigate the influence of a more complex waveform for the current reference. Our best results, from the perspective of noise performance, were achieved with the high-speed SDL lasers. However, we were able to operate both sets of VCSELs and the DFB lasers in the double-locked configuration. We configured a compact demonstration unit using inexpensive DFB lasers to demonstrate that the technique had potential beyond the laboratory.

A. SDL Lasers – Double-Locked Laser Implementation

For external optical injection at an optical frequency near the free-running optical frequency of the slave laser, increasing the strength of the optical injection causes the slave laser output to first become injection locked with stable output. Increasing further then causes a Hopf bifurcation to unstable dynamics, followed a transition to chaotic dynamics. Still higher injection induces a new range of periodic dynamics where the characteristic modulation frequencies increase with increasing excitation. Finally, at very high injection levels, the laser reestablishes stable, locked output with increased modulation bandwidth.³ A typical optical spectrum in the periodic dynamics range above the region of chaotic dynamics is shown in Figure 58. Here, the master laser optical frequency is shifted, $v_0 - v_1 = -3$ GHz, relative to the free-running slave laser frequency. The optical power incident on the slave laser output facet is approximately 8 dB below the output power of the free-running slave laser. However, the spatial overlap of the modes is not matched so that less is actually coupled into the oscillating mode. The spectrum shows the regeneratively amplified peak at the injection frequency and the two strongest sidebands. The dominant one, 14 GHz less than the optical injection frequency, oscillates at the injected-shifted dynamic resonance frequency and injection-shifted cavity resonance frequency. These resonance enhancements account for the strong asymmetry in the spectrum. Also shown for comparison is a spectrum of the free-running laser under current modulation, $v_m = 5.5$ GHz. This is approximately the relaxation resonance frequency of the free-running laser where the modulation signal peaks. Note the asymmetry of the peaks in the current modulation spectrum. This asymmetry is a result of the fact that $b' \neq b$.

While the regeneratively amplified peak is locked to the master laser, the sidebands are not in this unstable injection-locking regime. Without locking, there is an intrinsically broad linewidth to the power spectrum. The broadening is enhanced by jitter between the two lasers. Figure 59 shows the power spectrum of the photodetected signal around 14 GHz corresponding to the

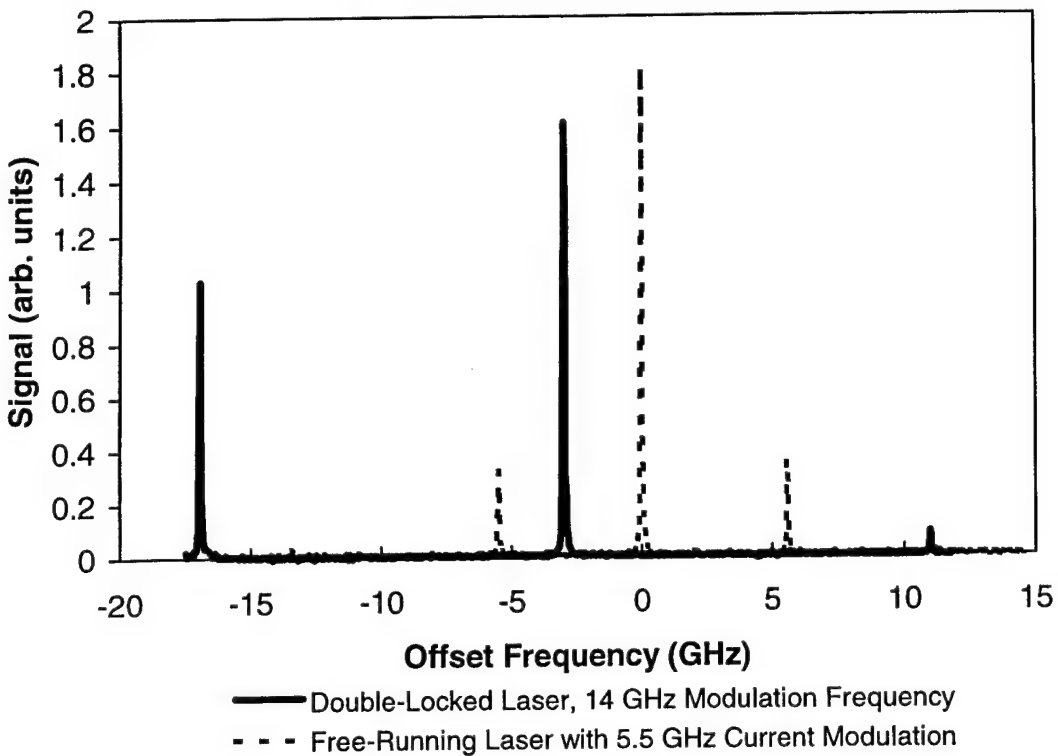


Figure 58. Optical spectra of the slave laser diode measured with the scanning Fabry-Perot optical spectrum analyzer. Frequency is referenced to the unmodulated, free-running frequency of the slave laser. The dotted curve is for the free-running laser undergoing a dc-bias plus a modulated bias current at 5.5 GHz. The solid curve is for the laser under dc-bias plus external optical injection at a relative frequency of -3 GHz which induces an instability generating a strong sideband 14 GHz below the injection frequency.

optical spectrum of Figure 58. The resonance feature jitter is evident as the spectrum analyzer sweeps across the spectrum. Locking the resonance frequency to a fixed reference frequency was readily accomplished by adding a modulation current to the dc bias current of the slave laser with a bias-T. Also shown in Figure 59 is the narrow resonance feature achieved when a 14-GHz current modulation is added. The spectrum of the locked feature was indistinguishable from the 1-kHz resolution bandwidth filter of the spectrum analyzer down to the noise floor more than 80 dB below the signal level. The modulation current used to achieve this locking was the same as used to generate the sidebands of the free-running laser at 5.5 GHz shown in Figure 58, $I_m/I_b \approx 0.18$. However, due to the circuit rolloff at 3 GHz and the reduced modulation response above the relaxation resonance frequency, the free-running laser produced a similarly narrow modulation feature as the locked resonance feature under external optical injection but with a signal level down by 36 dB.

The strong modulation of the optical power at microwave frequencies is readily tuned with only minor changes to the laser operating points. Figure 60 shows the range of locked frequencies achieved when the bias current to the master laser is varied. The principal effect of varying the bias current of the master laser over this range is to shift its optical frequency by -2.8 GHz/mA.

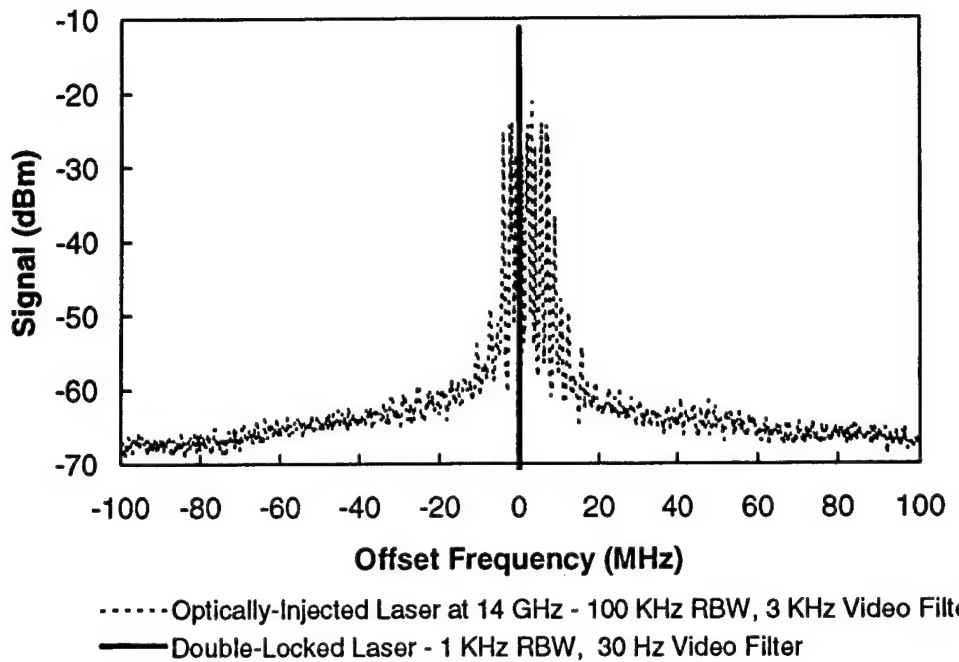


Figure 59. Spectrum of the amplified photodetector signal for the laser under the same external optical injection that yielded the optical spectrum in Figure 58. The dotted line shows the signal jitter without a locking current input to the slave laser and the solid line shows the locked signal. The locked signal is narrower than the 1-kHz resolution bandwidth (RBW) of the spectrum analyzer.

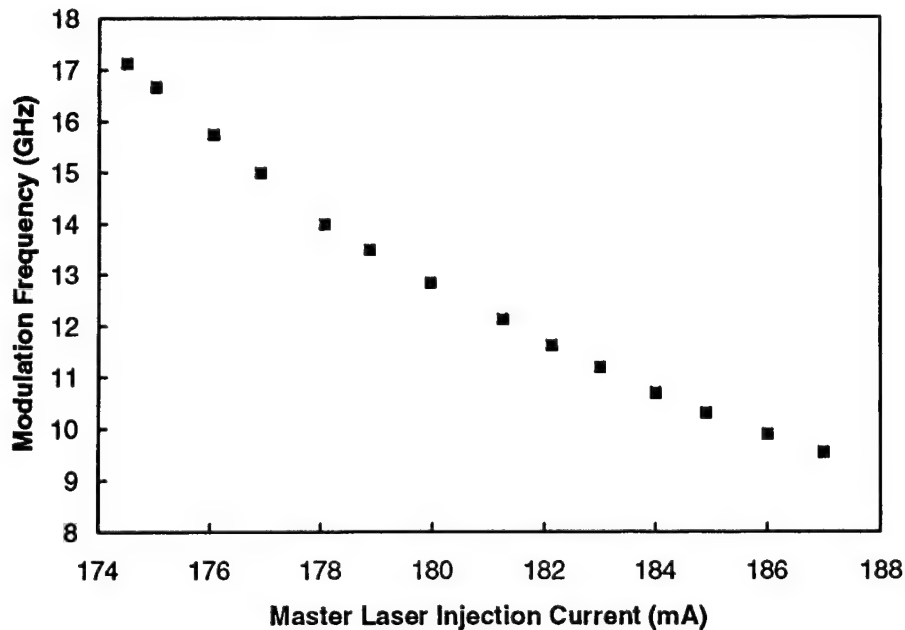


Figure 60. Tuning range of the locked modulation signal when the dc bias to the master laser is varied along with the frequency of the locking current modulation to the slave laser. All other parameters remain fixed. The point at 14 GHz corresponds to the spectra of Figures 58 and 59.

The low frequency end of the range where locking is achieved and a strong modulation signal is produced corresponds to the point where the laser reestablished stable, locked operation under optical injection. Reducing the injected optical power and/or changing the slave laser bias current could lower this boundary. The upper end of the range was limited by the output current from the frequency synthesizer and the rolloff of the modulation signal actually delivered to the laser diode gain medium. The highest locked frequency, 17.1 GHz, is almost six times the circuit rolloff frequency and more than three times the free-running relaxation resonance frequency. This demonstrates how a stable microwave frequency can be generated at frequencies well above those accessible to the free-running laser.

We also investigated the locking characteristics when the laser displayed period-doubling and period-quadrupling dynamics for injected optical powers below those discussed above and greater than required to observe chaotic dynamics. For moderately strong injection, 10 to 20 dB below the free-running output power, a destabilized system is produced where the strongest spectral feature is shifted relative to both the free-running optical frequency and the optical frequency of the injected signal. Figure 61 displays optical spectra for the slave laser when free-running and under two cases of optical injection; one for limit cycle dynamics where the master laser optical frequency is offset by $\nu_0 - \nu_1 = -3$ GHz, and one for period doubling dynamics where the master laser offset is decreased to $\nu_0 - \nu_1 = -2.5$ GHz. For the limit cycle spectrum, the optical power incident on the slave laser output facet is approximately 16 dB below the output power of the free-running slave laser. However, due to imperfect mode matching less is actually coupled into the oscillating mode of the laser diode. The incident power is approximately 50% larger for the period-doubling dynamics.

The strongest peak in the optical spectra of the laser undergoing external optical injection is at the injection-shifted cavity resonance frequency.^{1,3} Figure 62 plots the offset of this peak from the optical frequency of the master laser as a function of incident optical power from the master laser, for $\nu_0 - \nu_1 = -3$ GHz. The lowest output power displayed is where the laser shifts from chaotic dynamics back to periodic dynamics. The laser displays unstable, periodic dynamics over this range of injection with period doubling for injected powers between -15 and -8 dB. Weak period quadrupling is exhibited for injected powers between -13 and -11 dB. The frequency pushing of the cavity resonance increases monotonically, except for a small range within the range where strong period-doubling spectra are observed. There it remains nearly unchanged. If the frequency offset between the master laser and free-running laser is changed, then the offset of the shifted resonance is changed and different dynamics can be induced.¹⁻³

Because of the system instability, only the regeneratively amplified peak at the injection frequency is locked to the master laser. Jitter between the two lasers and intrinsic noise causes a broadening of the other spectral features. However, all the features can become locked with the addition of a weak modulation current at the difference frequency between the injected signal from the master laser and the shifted resonance peak. For the data reported below, comparing the current from the laser diode current supply and the output of the frequency synthesizer yields a modulation depth of $I_m/I_b \approx 0.07$. However, the useful current actually delivered to the gain medium was reduced by the 3-GHz RC rolloff. For example, in the free-running laser an 8-GHz modulation current at this modulation depth produced sidebands in the optical spectrum reduced

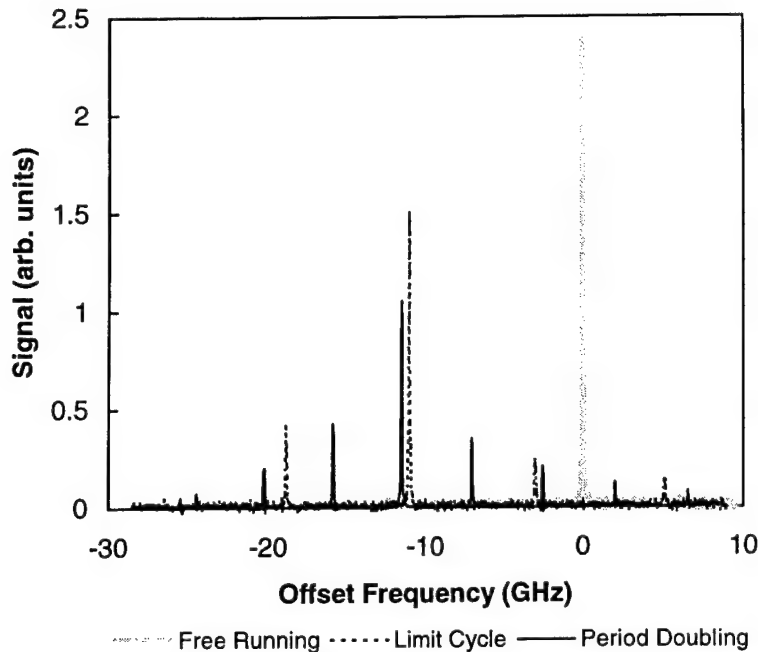


Figure 61. Optical spectra of the slave laser diode measured with the scanning Fabry-Perot optical spectrum analyzer. Frequency is referenced to the free-running frequency of the slave laser. The dotted curve is for the free-running laser. The dashed curve is for the laser under external optical injection at a relative frequency of -3 GHz which induces an instability generating limit-cycle dynamics. The solid curve is for the laser under external optical injection at a relative frequency of -2.5 GHz which induces an instability generating period-doubling dynamics.

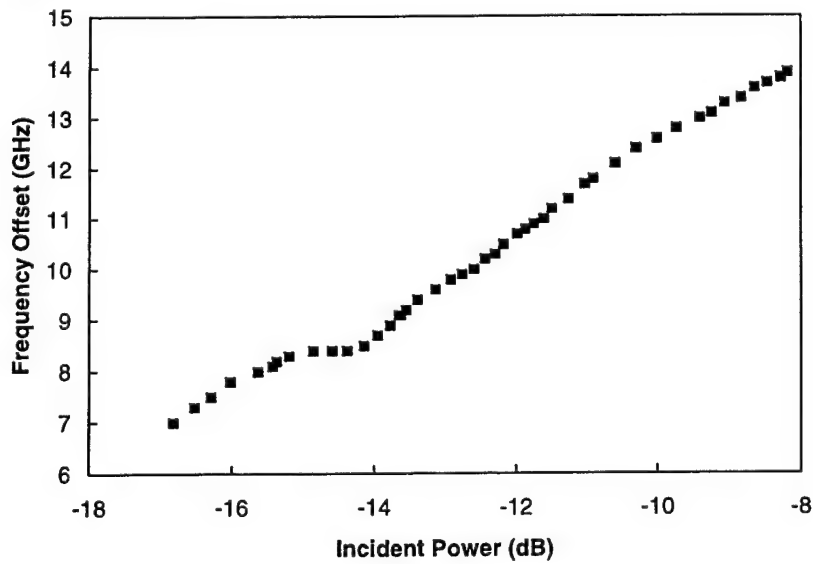


Figure 62. Shift of the resonance frequency offset as the incident optical power from the master laser is increased. External optical injection at an optical frequency 3 GHz below the free-running optical frequency of the slave laser. The incident optical power is referenced to the free-running output power of the slave laser.

by approximately 30 dB relative to the main peak. The modulation response is low because of the RC rolloff and the reduced modulation response beyond the 5.25-GHz relaxation resonance frequency of the free-running laser at this bias. Operating in the regime where optical injection induces the instability overcomes the latter constraint.

The stability of the modulation can be determined by mixing the photodetected signal with the reference current modulation and observing the IF output. Figures 63 and 64 show the IF output as the frequency of the modulation induced by the optical injection is swept through the frequency of the added modulation current. To sweep the modulation frequency induced by optical injection, the bias current to the master laser was swept about a small range. The principal effect of this current sweep is to shift the optical frequency of the master laser by approximately -2.8 GHz/mA. This shift changes the resulting offset of the resonance frequency.¹⁻³

In Figure 63 the current modulation frequency is set at 8 GHz, corresponding to the limit cycle spectrum of Figure 61. Outside of the locked regime the mixer IF voltage, which is proportional to the phase difference between the photodetector signal and the frequency synthesizer output, rapidly oscillates. However, when the modulation is locked, the voltage sweeps through a π -phase shift with the current sweep as the locked region is crossed. The phase follows a nearly linear sweep through the locked region. In Figure 64 the current is modulated at 4.355 GHz, so

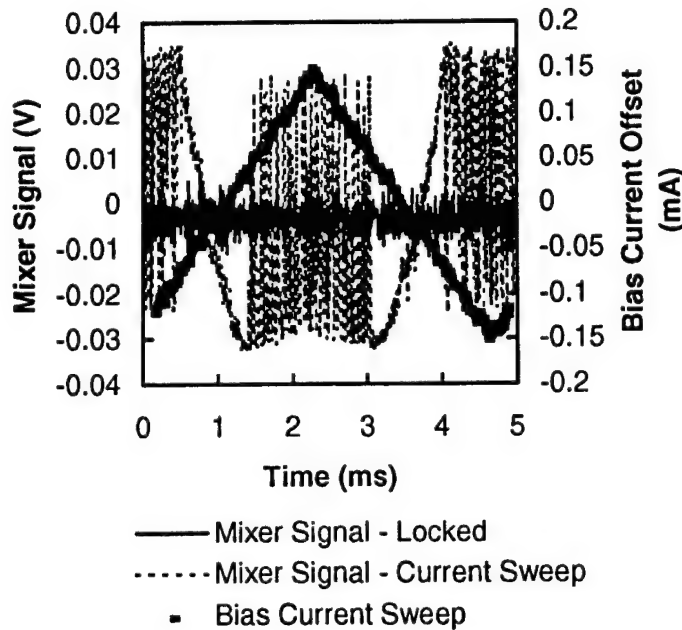


Figure 63. Locking characteristics of the laser under simultaneous external optical injection inducing limit-cycle dynamics and current modulation at 8 GHz. The dotted curve is the measured voltage from the microwave mixer as the current to the master laser is varied and the dashed symbols show the bias current variation (right axis). The solid curve is the measured mixer signal when the mixer voltage is simultaneously used to generate a phase-locked loop by varying the master laser current.

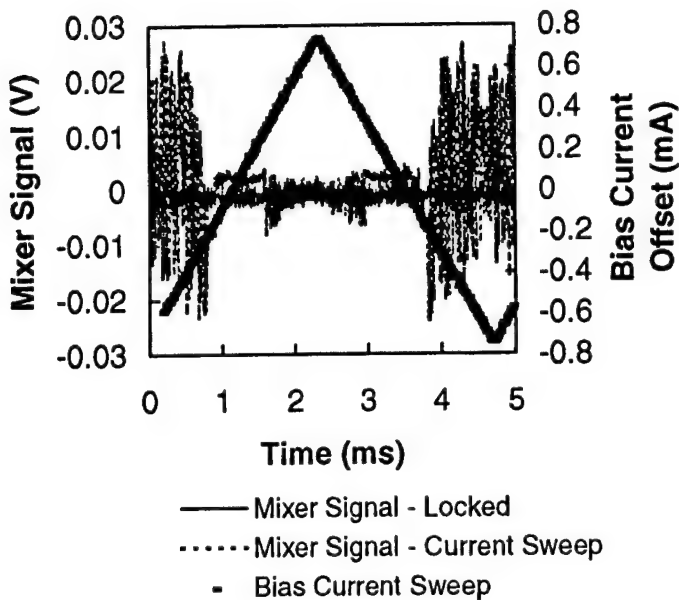


Figure 64. Locking characteristics of the laser under simultaneous external optical injection inducing period-doubling dynamics and current modulation at 4.355 GHz. The dotted curve is the measured voltage from the microwave mixer as the current to the master laser is varied and the dashed symbols show the bias current variation (right axis). The solid curve is the measured mixer signal when the mixer voltage is simultaneously used to generate a phase-locked loop by varying the master laser current.

that a period-doubling condition was locked. Now, there is a region within the locked operating range where the phase remains unchanged as the master laser current is swept just as there was a range of injected powers where the frequency offset of the resonance remained essentially constant.

To show that the induced microwave modulation could be phase locked to the current modulation reference, the IF output from the mixer was fed into the current supply of the master laser without further conditioning. The resulting mixer signal also appears in Figures 63 and 64. The signal corresponds to a total phase variance $\approx 0.015 \text{ rad}^2$ for the limit-cycle condition and $\approx 0.005 \text{ rad}^2$ for the period-doubling condition. Reduced noise in the spectrum of the photodetected signal was observed with a stronger modulation-current input, as will be described below. The residual noise that was not corrected by the OPLL and observed in Figures 63 and 64 was broadband, extending to beyond 100 MHz offset from the carrier.

A second set of measurements was taken to further elucidate the characteristics of the locking region of the laser under double-locked operation. Figure 65 shows representative curves of the locking as the power from the frequency synthesizer is increased by two orders of magnitude. Each operating condition shows two curves, with the direction of the scan reversed for the two curves. There is no obvious hysteresis. For the different modulation power levels, the dc-bias current is adjusted so that the locking range is approximately centered on the sweep. The

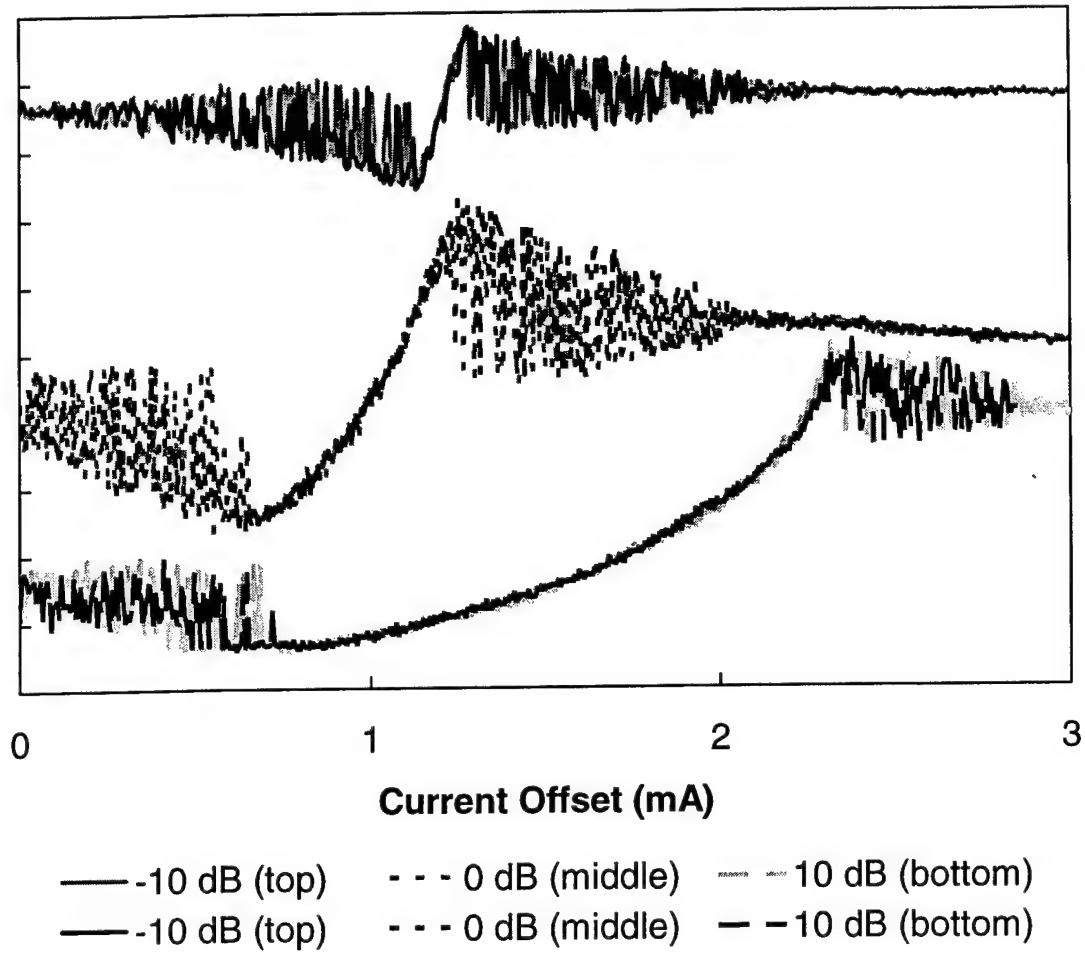


Figure 65. Scans showing the region of double locked operation as the operating point of the slave laser is varied by changing the bias current for three different modulation current power levels. The signal is the output of the microwave mixer when the photodiode output and microwave reference signal are the inputs. The frequency of the microwave reference signal is 14.11 GHz and the 10 dB power level corresponds to a current modulation level at the gain medium of approximately 0.02.

frequency synthesizer is fixed at 14.11 GHz, and the resonance frequency of the slave laser, f_{res} , is varied about this frequency as the bias current is changed. The locking range is the relatively smooth part of each curve in the middle. The higher modulation power levels, where the best phase noise performance is measured, show a voltage (\propto phase) vs. current characteristic that is nonlinear in the locking range. This correlated with a nonlinear resonance frequency vs. current characteristic when there is no modulation input to the slave.

Nonlinear dynamics theory predicts that a nonlinear oscillator can be locked not only to the resonance frequency but also to subharmonics of the resonance frequency. This occurs even though the dynamics of the laser under optical injection is essentially of limit cycle character when the resonance offset is in the range of 14 GHz. Changing the output frequency of the frequency synthesizer to 7.055 GHz $\approx f_{res}/2$ (one half the resonance frequency) also produced a

range of microwave power levels where the resonance frequency could be locked. Figure 66 shows the locking range for a modulation frequency of 7.055 GHz. Note that when the 7.055 GHz power is increased to 10 dB on this relative scale, the locking splits into two ranges offset from each other by about 2 mA. Optical spectra also differed between the two locked regions. This is indicative of two distinct attractors for locked operation.

Locking could also be achieved at $3.5275 \text{ GHz} \approx f_{\text{res}}/4$ and partial locking at $1.76375 \text{ GHz} \approx f_{\text{res}}/8$, but only at the highest power levels. The locking region was very complicated and the distinction between locked and unlocked not as clear because the locking was

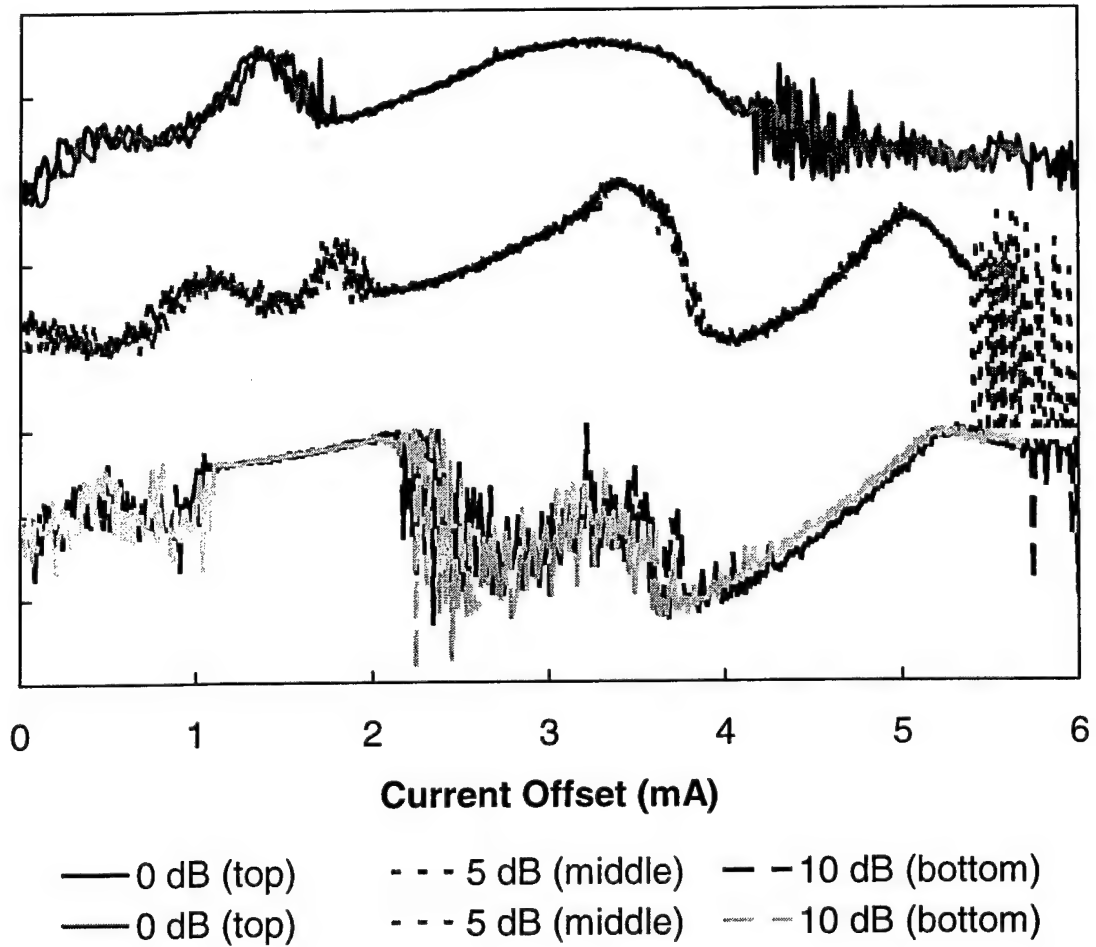


Figure 66. Scans (offset) showing the region of double locked operation as the operating point of the slave laser is varied by changing the bias current for three different modulation current power levels. The signal is the output of the microwave mixer when the photodiode output and microwave reference signal are the inputs. The frequency of the microwave reference signal is 7.055 GHz and the 0 dB power level corresponds to a current modulation level at the gain medium of approximately 0.02.

not as strong. The blurring of distinctions was due, at least in part, to the inability of the microwave mixer, which was rated for operation between 7-19 GHz, to produce a useful error signal. Operating in period-doubling and period-quadrupling regions allows the use of lower frequency current modulations as the reference. This may allow higher frequency modulations to be locked without requiring very wide bandwidth laser diodes.

Figure 67 shows the locking range as a function of the power level of the frequency synthesizer. The locking range is uniformly larger for the 7.055 GHz data than for the 14.11 GHz data. This is at variance with the generic behavior expected for nonlinear oscillators. In part this is due to the circuit parasitics. The modulation power actually delivered to the gain medium is actually 6 dB lower at 14.11 GHz data than at 7.055 GHz, while the chart does not correct for this. Even so, the locking is relatively stronger for the 7.055 GHz modulation than for the 14.11 GHz modulation. With the 14.11 GHz modulation, the laser retained a single locked region up to the highest power. Not plotted in this figure is the high power data above the point where the locked region breaks into two regions for the 7.055 GHz modulation data.

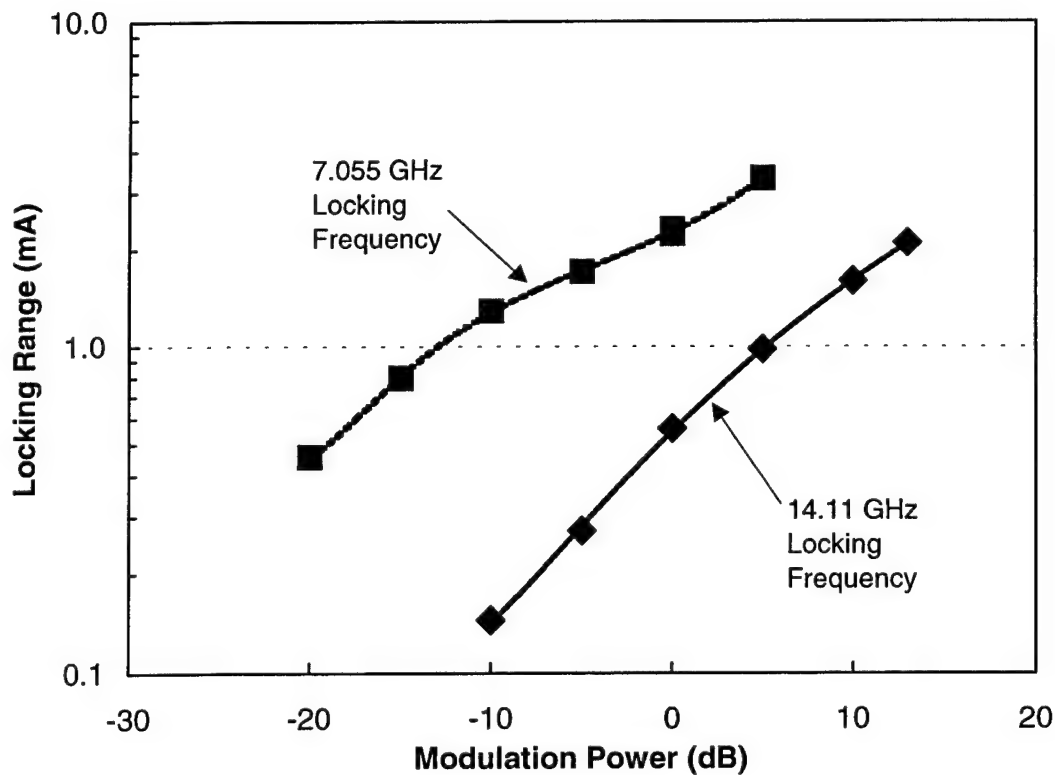


Figure 67. Locking range as a function of the modulation power level (not corrected for circuit parasitics) for modulation frequencies of 7.055 and 14.11 GHz. The resonance frequency of the laser under optical injection is approximately 14.1 GHz.

The fact that the laser does not follow simple trends typically expected of nonlinear oscillators is possibly due to the operating point of the slave laser. There is evidence of weak, broad spectral features at $f_{res}/2$ in the power spectrum measured by the spectrum analyzer. This indicates that the laser operating point is near a region of period doubling dynamics and is not operating a simple nonlinear oscillator with a characteristic resonance frequency. Operating near the region of period doubling dynamics enhances the susceptibility of the system to an external perturbation at the subharmonic resonance and complicates the dynamics by adding the possibility of multiple attractors. The locking characteristics remain relatively "clean" when the locking signal is near the resonance frequency. At subharmonics of the resonance, however, the situation is complex. This complicates the use of subharmonic locking signals as a way of circumventing device parasitics to lock high frequency resonances.

We also investigated the double-locked laser operation near the Hopf bifurcation. To do this, we detuned the optical frequency of the master laser with respect to the slave laser. For a constant injection level, detuning the master to negative offset frequencies brings the two lasers to the Hopf bifurcation. The frequency synthesizer was set to 7.63 GHz to match the resonance frequency at the detuned operating point. The master laser current was then varied to sweep about the operating point. The two plots in Figure 68 show the error signal from the mixer, as the current is swept, for different power levels from the microwave frequency synthesizer. At the high current end the sweep goes into the region of stable dynamics. The dashed line at the bottom of the chart marks this region. The solid line marks the double-locked operating region. Two curves are plotted on each chart. The upper curve is the error signal, similar to the curves shown previously. The lower curve is a plot of the power of the photodetected signal at the microwave reference frequency. When locked this power should be relatively high and when unlocked it should be low. On the upper plot there are labels indicating the difference between the reference frequency from the microwave frequency synthesizer and the unlocked resonance frequency. For difference frequencies above about 200-300 MHz, the oscillation of the mixer signal is beyond the analog bandwidth of the oscilloscope. This explains why the unlocked signal drops away for large offsets between the synthesizer and resonance frequency. At the higher power levels, the laser goes directly from locked operation into an extended stable regime into the double locked region. There is a phase change to the signal when there is a jump between the two locked regions. There is probably a dc amplitude change as well. There appears to be hysteresis at the highest injection level for the transition to/from the double locked to stable operation. It is shown in the last plot. The others showed possible hysteresis but it was within the noise fluctuation limits.

The observation of a phase jump as one moves from double-locked operation into the region of stable, locked operation points to the difference between the double-locked laser and a directly modulated semiconductor laser. In the double-locked laser there is an inherent instability in the optically injected system with a characteristic resonance frequency. This resonance can be locked to an appropriately tuned resonance and the phase can be adjusted by changing the reference frequency. The directly modulated semiconductor laser cannot have its output controlled in this way. Further, for high modulation frequencies, the double-locked laser configuration is more efficient in the coupling of injected microwave power to generated microwave power in the photodetector.

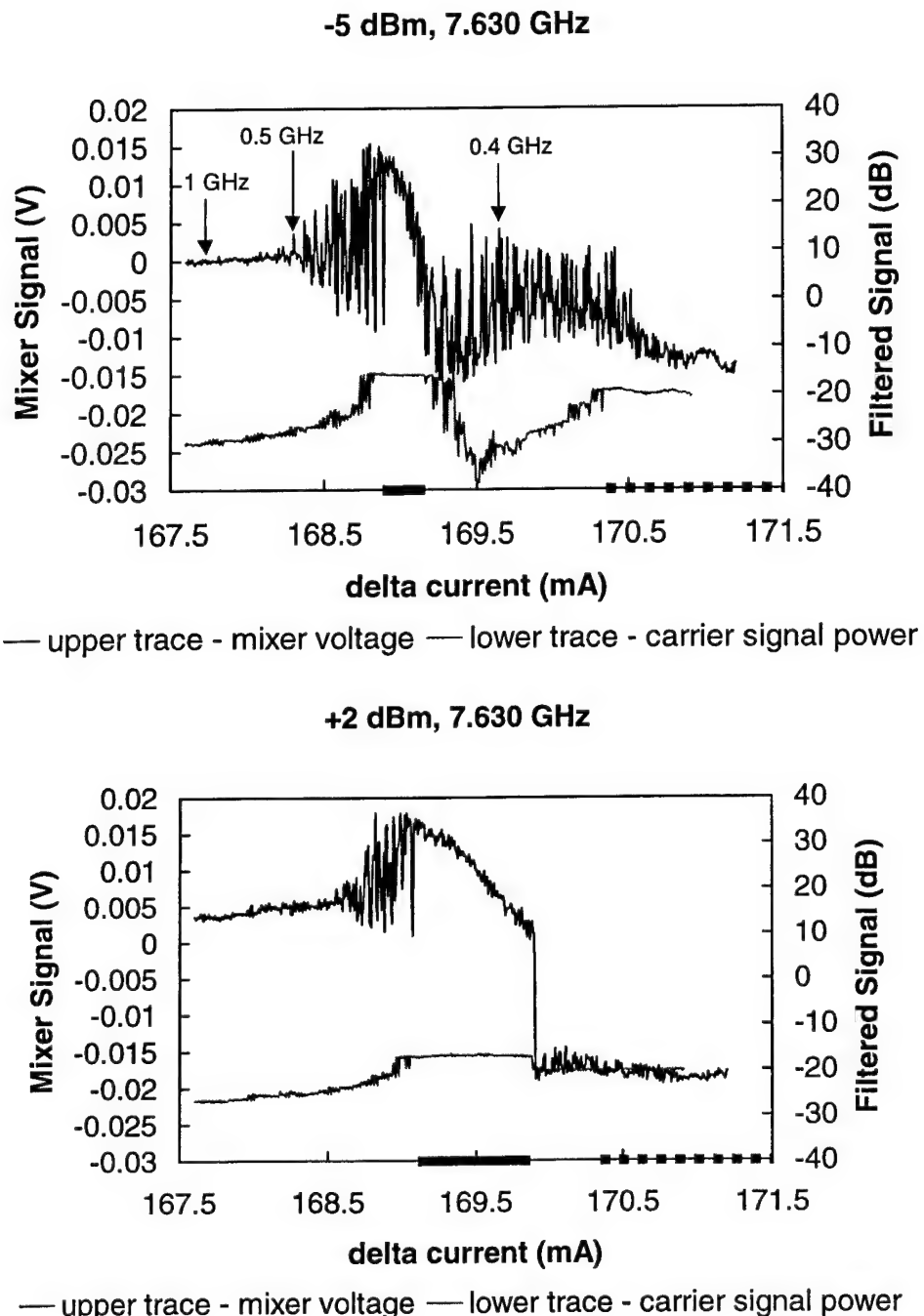


Figure 68. Double-Locked laser characteristics near the Hopf bifurcation. The two figures showed different output power levels from the frequency synthesizer supplying the locking microwave reference, with a 7 dB power difference between the two. In each figure the upper trace is the output voltage from the microwave mixer showing the phase error signal while the lower trace is the measured poser at the reference frequency. The thick solid line at the bottom of each figure denotes the double locked operating range while the dashed line denotes the region of stable, locked operation without the microwave reference.

In a final modification of the locking configuration, we attempted to observe how well the photodetected signal from one double-locked laser diode could be used to lock a second laser diode in the double-locked configuration to a microwave reference. To do this we modified the experimental setup so that a single master laser could pump two slave lasers. We created a second slave laser optical path with the unused port of the beam splitter used to couple the master to the original slave laser and then couple the slave output to the monitoring apparatus. A second beamsplitter was used as a combination beam steering element and as a coupling port to a second fast photodetector. The beam from the second slave laser was slightly misaligned with respect to the optical path to the original fast photodetector so that the detectors measured the optical output of the two slave lasers individually. With this arrangement, there is no direct coupling path between the two slave lasers. The photodiode signal from the photodiode monitoring slave laser #1 was used as the reference modulation input to slave laser #2. The injection level from the master was adjusted to produce a limit cycle condition with the same resonance frequency in the two slave lasers. This resonance was locked to a microwave reference from the frequency synthesizer in slave laser #1. The experiment attempted to measure the fidelity with which the microwave resonance was reproduced in slave laser #2, where, again, the locking reference was the amplified photodiode signal from slave laser #1.

We measured both the temporal and frequency characteristics of the photodetected signals from the double-locked laser diodes. The temporal characteristics were measured with a sampling oscilloscope triggered by the frequency synthesizer signal. Figure 69 shows representative time traces. The trace marked Slave #1 – No Feedback that oscillates smoothly between approximately -1 and 1.8 volts is the photodetector signal of slave laser #1 in the standard double-locked configuration. The optical path to slave laser #2 is also blocked for this trace. When we removed the block in the path to slave laser #2, we observed excess noise in the signal from slave laser #1, as shown by the offset temporal trace marked Slave #1 – With Feedback. We determined that the excess noise arose from minute amounts of optical feedback from slave laser #2 to slave laser #1. Even though there are no direct optical paths between the two lasers, they both must pass through AR-coated optical elements. While the feedback from these optical elements was insufficient to disturb the signal from either laser when operated individually, the mutual coupling caused by the weak feedback between the two lasers was sufficient to produce a detectable change. Nonetheless, we did observe poor locking of the second slave laser to the microwave reference, as shown by the trace labeled Slave #2 - Averaged. We had to use an averaging function on the sampling oscilloscope to correct for noisiness. Nonetheless, the fact that the second slave laser is, on average, locked to the trigger from the frequency synthesizer shows that the photodetected feedback can be used as a reference. Mutual coupling due to spurious feedback from optical elements is, however, clearly a problem.

We also looked at the spectral characteristics of the double-locked output from the two slave lasers. Figure 70 shows how the mutual coupling changes the locked spectral feature from slave laser #1. When the path to slave laser #2 is blocked, one observes an essentially instrument-limited resolution peak at the locking frequency. When mutual coupling is present, this feature is corrupted. The corruption is essentially the same for the two lasers, as shown in Figure 71. The weak optical feedback is sufficient to change the locking characteristics caused by the signal from the photodetector monitoring slave laser #1.

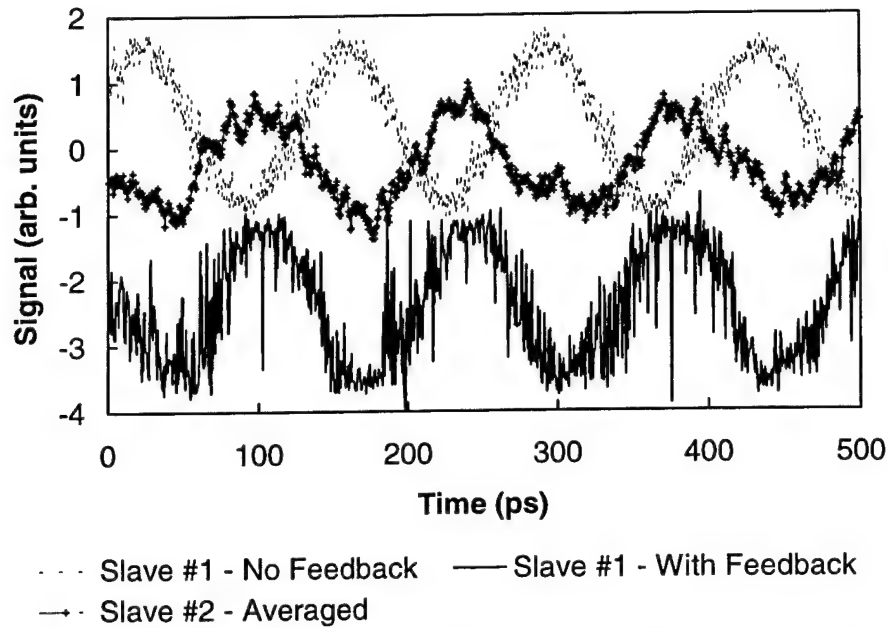


Figure 69. Sampling oscilloscope traces of the locked resonance signals from the two photodiodes. Slave #1 – No Feedback is the signal when the path to slave #2 is blocked. Slave #1 – With Feedback is the signal measured from #1 when the path to #2 is unblocked. Slave #2 – Averaged is the signal (offset) from #2 when locked by the reference from #1 photodetector.

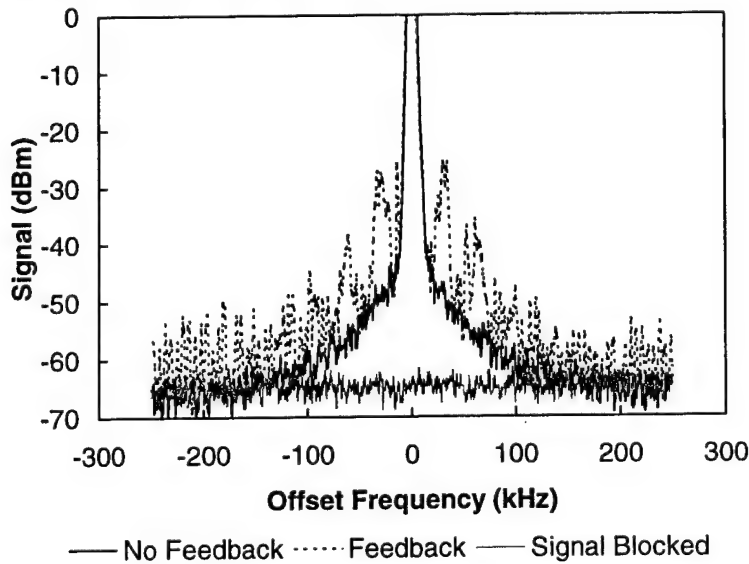


Figure 70. Spectra of the double-locked resonance feature of slave laser #1. The trace labeled Signal Blocked gives the background noise level when no signal is present. The trace labeled No Feedback gives the shows the locked resonance feature, with resolution of the central peak limited by the spectrum analyzer. The trace labeled No Feedback shows the changes caused when the optical path to slave #2 is unblocked. The peak signal is 10 dBm, so that the strongest feedback induced sideband is down by approximately 40 dB.

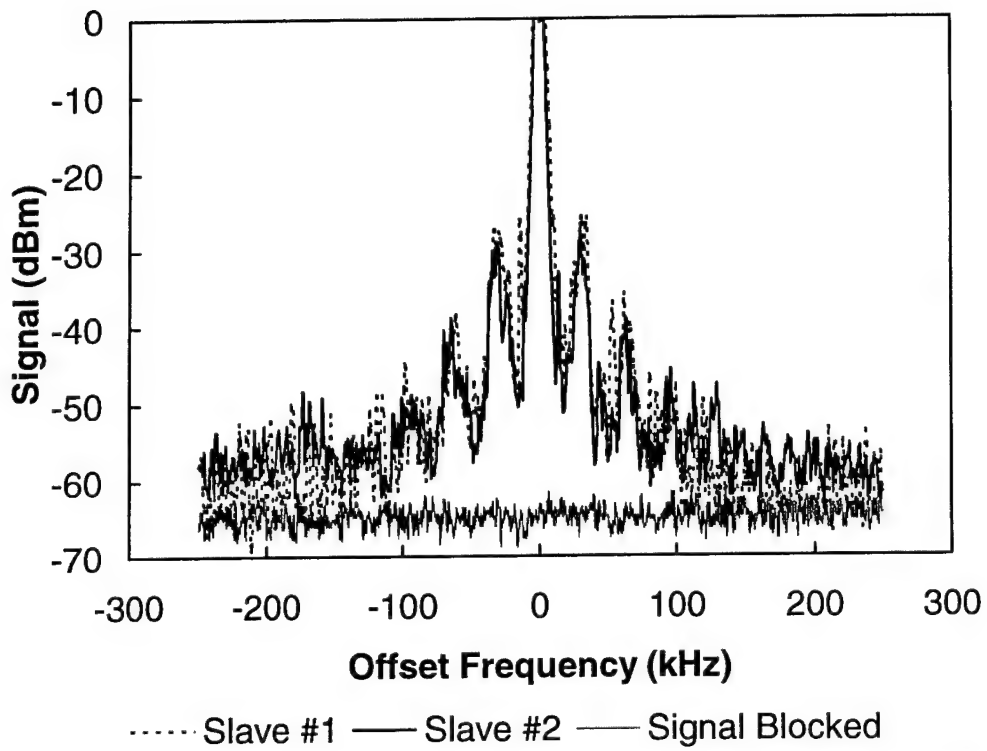


Figure 71. Spectra of the double-locked resonance feature of slave lasers with weak optical feedback. The trace labeled Signal Blocked gives the background noise level when no signal is present. The traces from the two slave lasers are identical, within experimental accuracy, showing the weak optical feedback is still locking the two lasers, but reducing the fidelity of either to the original microwave reference. The peak signal is 10 dBm, so that the strongest feedback induced sideband is down by approximately 40 dB.

The fact that the resonance spectra from the two lasers is identical, to within experimental accuracy, shows that the weak optical coupling adds a second, unwanted locking characteristic to the two lasers. Because of this additional locking, the fidelity of either laser to the original microwave reference signal is reduced. This occurred with a optical coupling signal that was too small for us to measure. It was down by at least 50 dB relative to the output signals of the slave lasers. This level of sensitivity may be difficult to overcome in any realistic optical system where a single master laser is meant to optically inject several slave lasers without mutual coupling. However, the results presented above should be considered preliminary. We had hoped to return to this configuration and make a more concentrated attempt to reduce coupling between the lasers, but time constraints did not allow us to do this.

B. SDL Lasers – Double-Locked Laser Low Frequency Phase Noise

To get a more quantitative understanding of the noise characteristics, we performed two additional sets of measurements. In the first, we added a very low frequency, on the order of Hz, current modulation to the dc bias of either the master or slave laser. An additional low frequency current modulation is induced in the slave laser by applying the output from a signal generator to a current-modulation input on the bias control of the slave laser. The slave laser current controller had conversion gain of 40 mA/V for the modulation signal from the signal generator. The output from the fast photodiode monitoring the slave laser is amplified and sent to a microwave mixer where the signals riding on the microwave carrier are downconverted. Low frequency signals (<1 kHz) are the error signals that are fed back to the master laser current control to generate a phase-locked loop to lock the phase of the resonance oscillation of the optical power to the phase of the frequency synthesizer reference. The open loop gain on the phase locked loop is approximately 130 mA/mA. No detailed effort was made to optimize the phase-locked loop.

The output signal from the microwave mixer gives the information about the stability of the output power modulation of the laser diode. Here, we are specifically interested in the low frequency characteristics. The mixer output was passed through a preamplifier with adjustable gain and high-frequency rolloff before being measured with a digitizing oscilloscope. Data records of 1,024 points were stored, and then the time-traces were Fourier to produce a low frequency spectrum. The modulation signal from the signal generator into the slave laser provides a means of calibrating the noise spectrum to a known current modulation. A 2 Hz triangle wave was used as the reference. The amplitude was adjusted to provide a useful current modulation level.

Data was taken with the double-locked laser operating with a resonance frequency of approximately 14 GHz, where the two main peaks of the optical spectrum are of similar amplitude. Figure 70 shows the measured input signal from the signal generator and the resulting error signal. The sampling rate for the data is 48.8 Hz and the low pass filter of the preamplifier is 10 Hz. The fractional current modulation corresponding to the signal generator input of $\pm 5 \times 10^{-4}$. Even when the signal generator voltage is reduced by a factor of 25, the modulation is still visible on the error signal.

Fourier transforming the time traces allows us to compare the modulation with the noise spectrum. Spectra are shown in Figure 71. There is a strong peak at the frequency of the triangle wave modulation and a weaker peak at the third harmonic. For frequencies above about 4 Hz the noise floor of the detected signal and the signal generator signal are identical, showing that we are again instrument limited. However, for lower frequencies the noise of the photodetected signal starts to rise while that of the signal generator does not, indicating that we are observing the fluctuations of the photodetected signal. Comparing the modulation peaks with the noise background, we can estimate that the carrier to noise level is approximately 95 dB/Hz at 1 Hz and > 105 dB/Hz above 4 Hz. From our previous measurements we know that it is > 110 dB/Hz at frequencies beyond 250 kHz, again with our measurement apparatus noise floor masking the true noise level of the device.

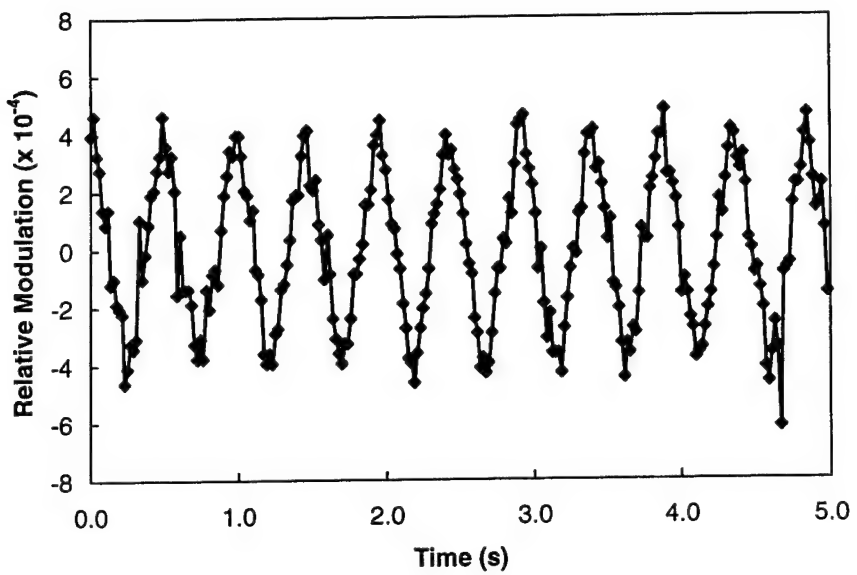


Figure 72(a)

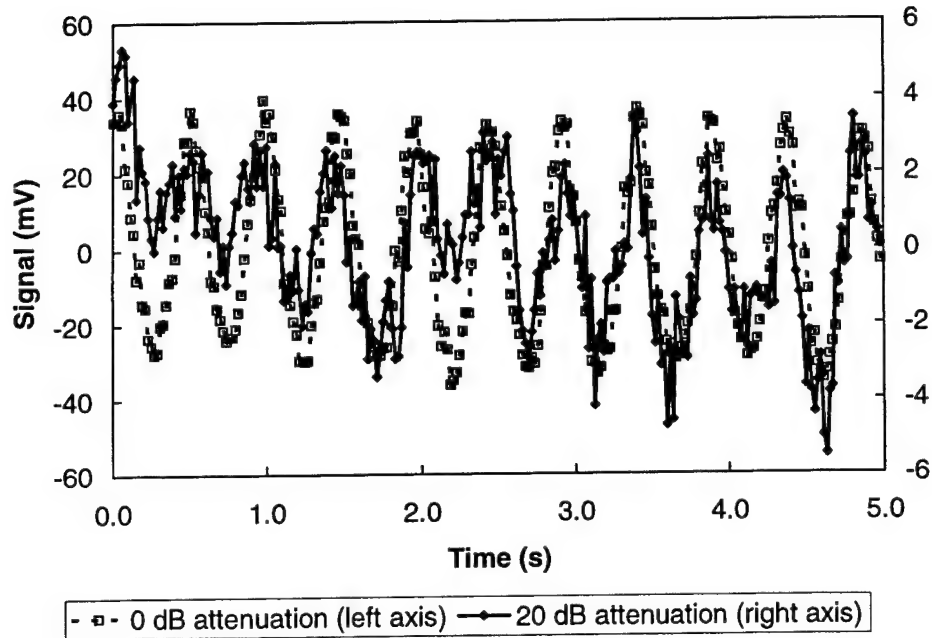


Figure 72(b)

Figure 72. Measured signals used in the slow modulation experiments to determine the stability of the locked microwave resonance. (a) The input signal to the slave laser current driver used to impose the slow phase modulation. (b) The measured signal at the output of the microwave mixer showing the recovery of the downconverted signal, and the recovered signal when the input signal voltage is reduced by a factor of 10.

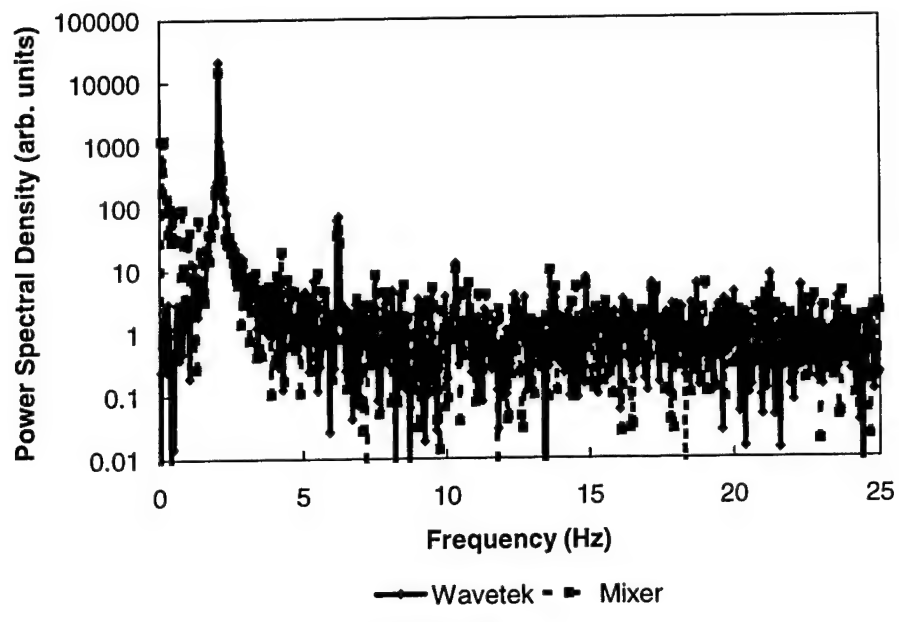


Figure 73(a)

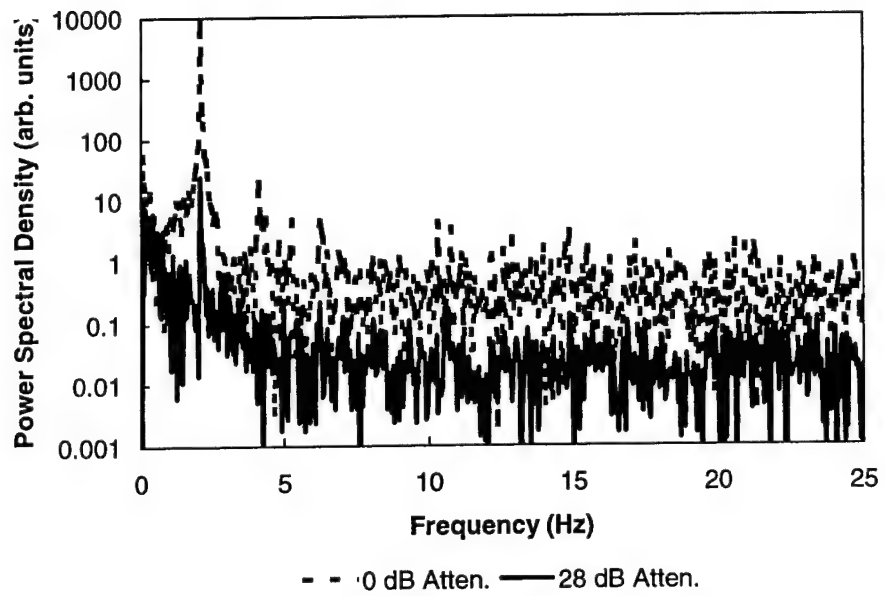


Figure 73(b)

Figure 73. Fourier transforms of the low frequency modulation data. (a) An overlay of the signal generator (Wavetek) and mixer spectra. Below 4 Hz, the mixer output deviates from the instrument-limited background. (b) Two different mixer output spectra with the dotted curve corresponding to a current modulation index of 5×10^{-4} and the solid curve corresponding to 2×10^{-5} .

Finally, we built upon the previous tests at single Hz frequency offsets from the microwave reference by conducting true phase noise tests of the photodetected signals. The tests showed that the lasers could achieve excellent phase noise performance levels, both absolute and residual, with absolute phase noise limited by the noise characteristics of the microwave frequency synthesizer used in the tests, and residual phase noise in the -125 dBc/Hz range when the laser was operated in the optical phase-locked loop configuration. Data was taken with the double-locked laser operating with a resonance frequency of approximately 14 GHz, where the two main peaks of the optical spectrum are of similar amplitude.

Phase noise measurements were made using a phase noise test set supplied and operated by Prof. Paul Yu and Mr. Dongsoo Shin of the University of California, San Diego, Department of Electrical and Computer Engineering. The test set consists of a highly stable microwave frequency reference, a dynamic signal analyzer and a phase noise measurement unit. Figure 74 shows the phase noise measured when the HP 8673C microwave frequency synthesizer used as the input reference for the double-locked laser is used as the device under test. This can be considered the absolute phase noise of the synthesizer because independent tests of the microwave reference used in the phase noise test set show a noise level that is consistently at least an order of magnitude lower. The absolute phase noise of the photodetected signal from the double-locked laser diode is the upper curve shown in Figure 73. Within the reproducibility of the measurement, the absolute noise is the same as that measured directly from the frequency synthesizer. No OPLL was required to achieve this level of performance.

The phase noise test set could be reconfigured to use the HP 8673C as the input, allowing residual phase noise tests to be made. Measurements of the residual phase noise required that the OPLL be engaged. After generating an error signal for the OPLL by mixing the amplified photodiode signal with the microwave reference using a broadband microwave mixer, the error signal was amplified and low pass filtered using a PAR Model 171 preamplifier. Further filtering is provided by a 1 kHz low pass filter in the analog modulation input to the bias current supply. Figure 75 shows two residual phase noise measurements. In the middle curve of the figure the PAR preamplifier is set to a gain (voltage) of 50 and a low pass filter frequency of 100 Hz while the lower curve was made at a gain setting of 5000 and 10 Hz frequency rolloff. The gains chosen were the highest that allowed stable operation at the low-pass filter frequency setting. The open loop gain for the OPLL was approximately 100 mA/mA and 10 A/mA for the low and high gain conditions, respectively.

While we could not measure the phase noise at higher offset frequencies directly, we could measure the signal-to noise ratio in the region of the carrier frequency with the microwave spectrum analyzer. Figure 76 shows a measured spectrum under double locked operation. Such spectra were independent of whether the OPLL was engaged or not. The wideband noise of the double-locked laser lies just above the system background noise for offset frequencies within 2 GHz of the carrier. The carrier signal is offscale and was measured at 4.4 dBm. The resolution bandwidth of the spectrum analyzer was set to 1 MHz. When the background noise power is subtracted from the power measured under double-locked operation, one calculates a noise level of approximately -130 dBc/Hz outside of the central peak, consistent with the -125 dBc/Hz residual phase noise measured at 100 kHz offset frequencies in Figure 75. Note that the high

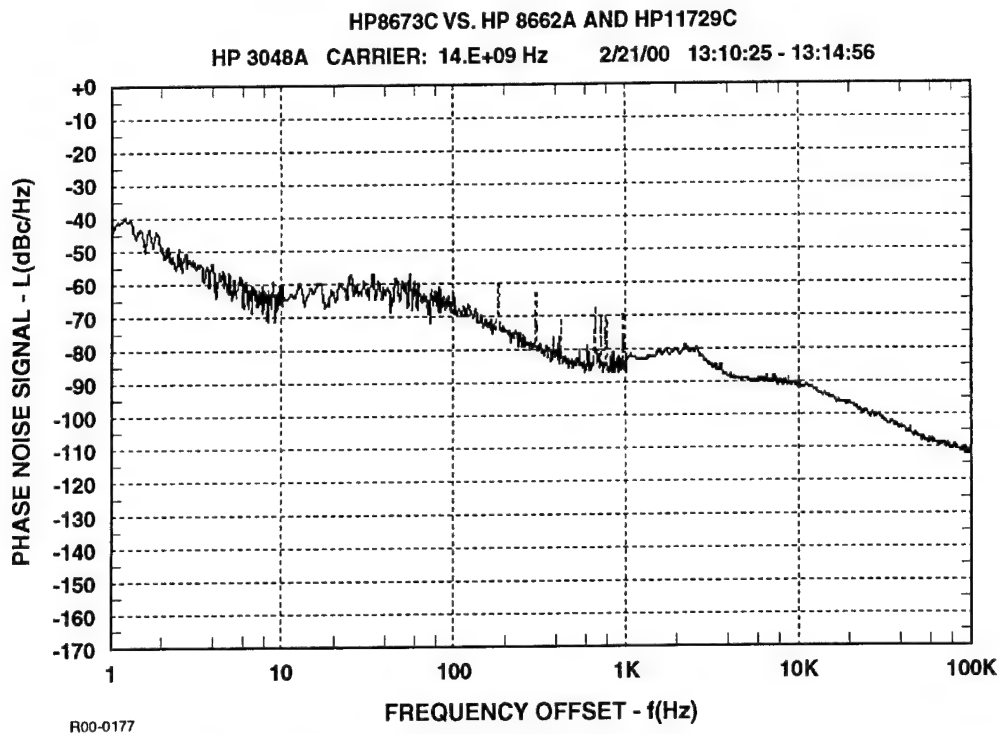


Figure 74. Absolute phase noise of the HP 8673C that is used as the reference oscillator for the double-locked laser diode.

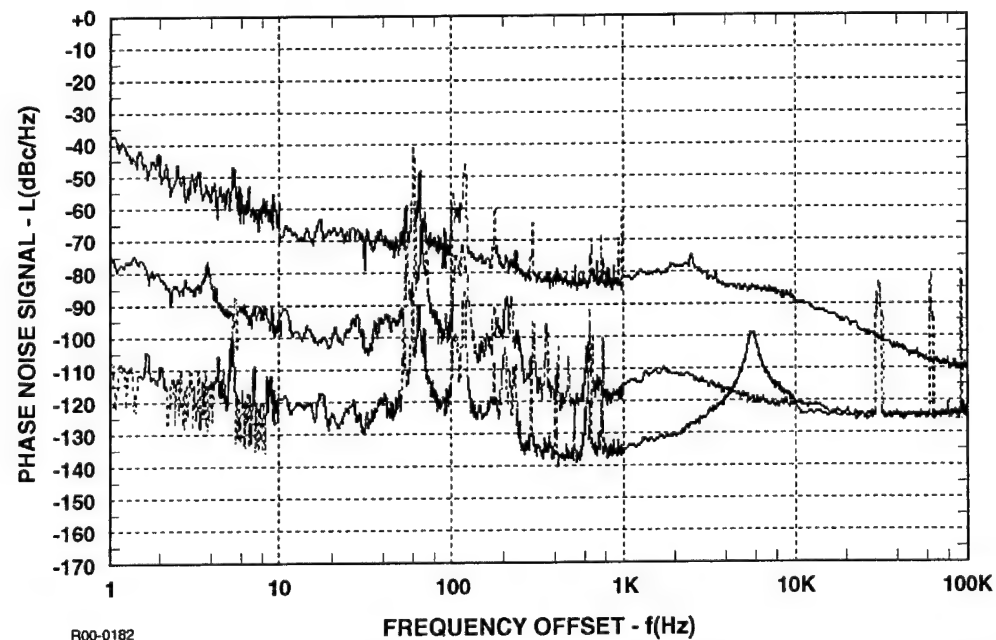


Figure 75. Phase noise of the photodetected signal of the optical output from the double locked laser diode. The upper curve is the absolute noise level. The two lower curves are the residual phase noise levels using two different gain levels and low pass filter frequencies for the OPLL.

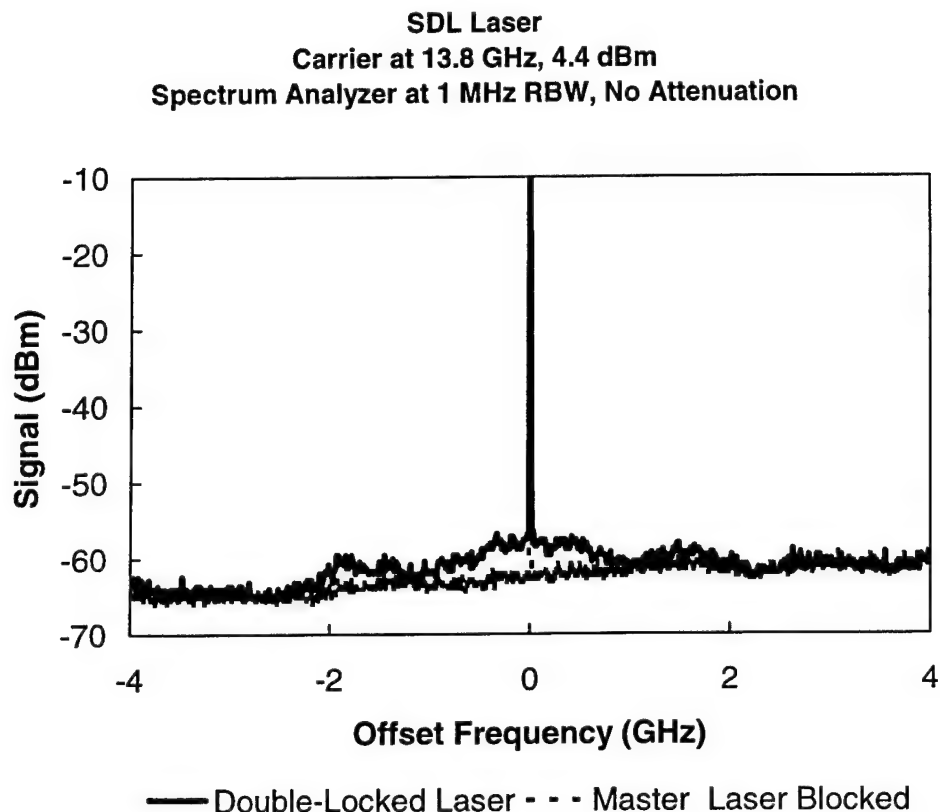


Figure 76. Microwave spectrum of the photodetected signal in the frequency region near the microwave carrier frequency of 13.8 GHz. The double locked laser and free running laser spectra are shown. The double-locked laser carrier signal is off-scale at 4.4 dBm. When the master laser is blocked, the free-running laser carrier signal is -14.8 dBm.

frequency residual phase noise was independent of the OPLL gain condition. Therefore, the double-locked laser diode shows excellent noise characteristics, both narrow band and broadband.

Figures 75 and 76 represent the best noise performance that we measured under double-locked operation. Compared to published data in the literature, the phase noise characteristics of the double-locked laser diode are excellent. The residual phase noise data shows superior performance to published data using sideband injection locking,¹⁸ a technique where the master laser is modulated and the slave laser is locked to the master laser sideband.¹⁹ Performance is also superior to phase locked performance of two external cavity laser diodes.²⁰ Further, the sideband injection locking technique has been implemented within a single laser device, a multisection DFB laser, with good phase noise.²¹ Such a device should be able to show improved performance using the double locking technique that we have developed. Multisection DFB laser devices will soon be commercially available products.²² The noise characteristics of the detected modulation signal also compare favorably with those of two free-running laser diodes locked

with a very fast optical phase-locked loop.²³ Here, however, a slow, simple loop was sufficient. Use of external cavity semiconductor lasers eases the high-speed loop requirement,^{20,24} but at the expense of a greatly complicated laser configuration.

C. SDL Lasers – Double-Locked Laser Modulation Characteristics

We also investigated the locking characteristics of the new technique in the presence of additional RF and microwave modulations of the master and slave laser bias current. The microwave modulation generated by this technique can be further amplitude and phase modulated by adding another, lower frequency modulation to the input current. These modulations represent some information-bearing signal to be placed on the subcarrier. They might represent the modulation of a radar waveform to be carried on the optical carrier to a remote antenna, or a data stream carried on the sub-carrier for multiplexing purposes. Due to the nonlinear interaction between the optical field and the injected carriers in the gain medium, the amplitude and phase modulation can be added at baseband and is then upconverted to the microwave region in the double-locked laser diode. The lower frequency modulation appears as sidebands to the microwave modulation frequency signal. Figure 77 shows an example of a 475-MHz current modulation added to an 8-GHz locking frequency. Strong sidebands, offset by 475 MHz, and weaker sidebands at harmonics, are produced. These sidebands also retain good spectral characteristics and show that an information-bearing signal can be imposed on the microwave modulation, but only if the amplitude of the lower frequency modulation is not too strong. As can be observed in Figure 77, modulation peaks reduced by 10 dB relative to the carrier induce harmonics that are reduced by only an additional 15 dB. Further, there is a rise in the broadband noise background near the central peak. This indicates that the presence of the 475 MHz modulation is starting to weaken the locking characteristics.

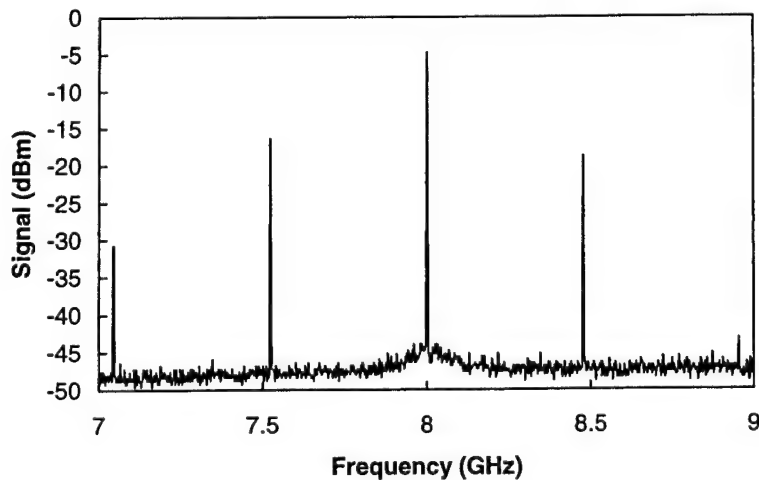


Figure 77. Spectrum of an optically-induced resonance feature which is locked to an 8 GHz current modulation. A second current modulation at 475 MHz appears as sidebands of the locked frequency showing the upconversion due to the nonlinear interaction within the laser diode. Resolution bandwidth for this spectrum is 1 MHz, accounting for the higher noise floor. Also, locking was not complete, so that the central peak sits on a pedestal.

The signal modulation can be added to the optical output in a variety of ways. Perhaps the simplest ways are to add the modulation to the bias current of either the master or slave lasers. The optical spectra showed significant differences depending upon whether the signal modulation was added to the slave or master laser bias currents. A comparison is shown in Figure 78. For this example, the master laser was operated at an optical frequency approximately 1-3 GHz below the free-running optical frequency of the slave laser. The two lasers slowly drifted in frequency with time and the exact offset was not continuously monitored. The spectra are referenced to the frequency of the master laser. The amplitude of the injected optical signal was adjusted so that the resonance peak was approximately the same as the peak at the injection signal. The spectra in Figures 78(a) and (b) were taken with a weak modulation current from the network analyzer added to the bias of the slave laser. Figure 78(b) is an expanded scale version of 78(a). Gaps in the spectral curves contain spectral features that are experimental artifacts of the scanning Fabry-Perot optical spectrum analyzer. They were removed for clarity. The locking frequency of the signal from the frequency synthesizer is 13.7 GHz and the modulation frequency of the signal from the network analyzer is 5 GHz. Sidebands of the three main peaks offset by 5 GHz are clearly visible in Figure 78(b) with the strongest sidebands on the resonance feature. Note the asymmetry of the sidebands and the reverse of the asymmetry on the central peak relative to the two side peaks. In Figures 78(c) and (d) the signal modulation from the network analyzer now is injected into the master laser and the frequency of the locked resonance is 15 GHz. Now the dominant sidebands are on the central peak, corresponding directly to the regeneratively-amplified locking signal from the master laser. The sidebands of the resonance peak are quite weak. In Figures 78(e) and (f) the modulation frequency from the network analyzer is reduced from 5 GHz to 1 GHz where there is a stronger signal. Also, the locked frequency is 12.7 GHz. Now the weaker sidebands on the resonance peak are more clearly visible. Again, note the reversal of the asymmetry of the central peak with respect to the two side peaks.

Using the network analyzer, we could observe the frequency dependence of the modulation signal response. First, it was necessary to correct for the parasitic spectrum due to the overall electronic circuit. Figure 79(a) shows the response of the free-running lasers to a weak current modulation. Superimposed on the data are calculated curves using the single-mode model, corrected for the simple RC-response of the cable and laser diode package. The fit to the data is good. Therefore, we used the deviation of the free-running data from the uncorrected model curve as the measure of the total system parasitics. Figure 79(b) shows the modulation response under optical injection that generated a resonance frequency of 15 GHz and the network analyzer modulation current injected into the slave laser. This locking frequency was at the highest injected optical power level. Shown are the raw data, the corrected data, and the model calculation for the free-running laser. At this operating point the frequency dependence of the response of the double-locked laser is similar to the response of the free-running laser, with a stronger peak near 5 GHz.

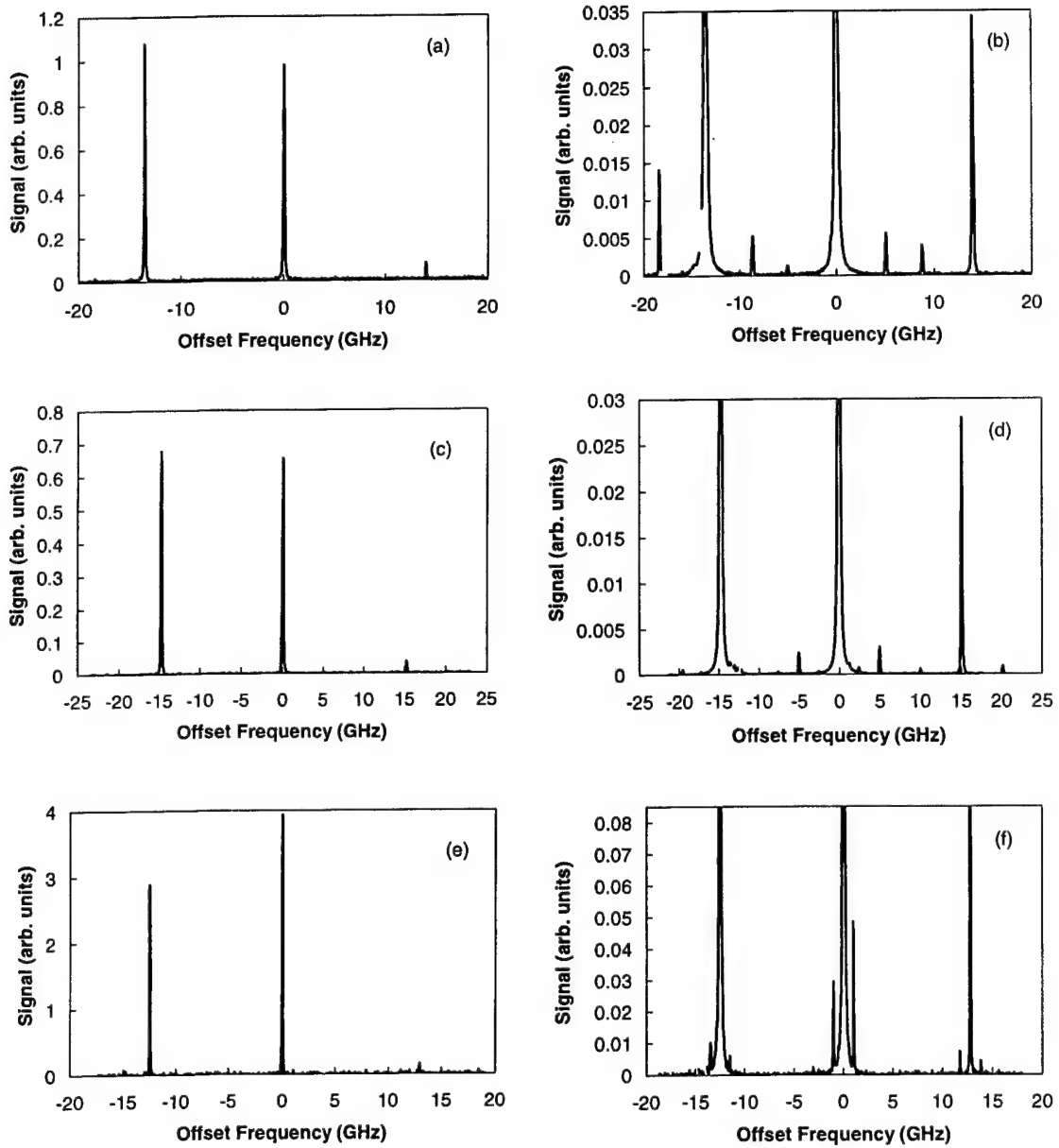


Figure 78. Optical spectra of the slave laser under optical injection and signal modulation.
 The spectra in the right column are vertically expanded views of the spectra in the left column. The frequency is referenced to the master laser optical frequency so that the peak at zero offset corresponds to the regeneratively amplified master laser frequency. In (a) and (b) the locked resonance frequency is 13.7 GHz and a 5 GHz current modulation is added to the slave laser. In (c) and (d) the locked resonance frequency is 15 GHz and a 5 GHz current modulation is added to the master laser. In (e) and (f) the locked resonance frequency is 12.7 GHz and a 1 GHz current modulation is added to the master laser.

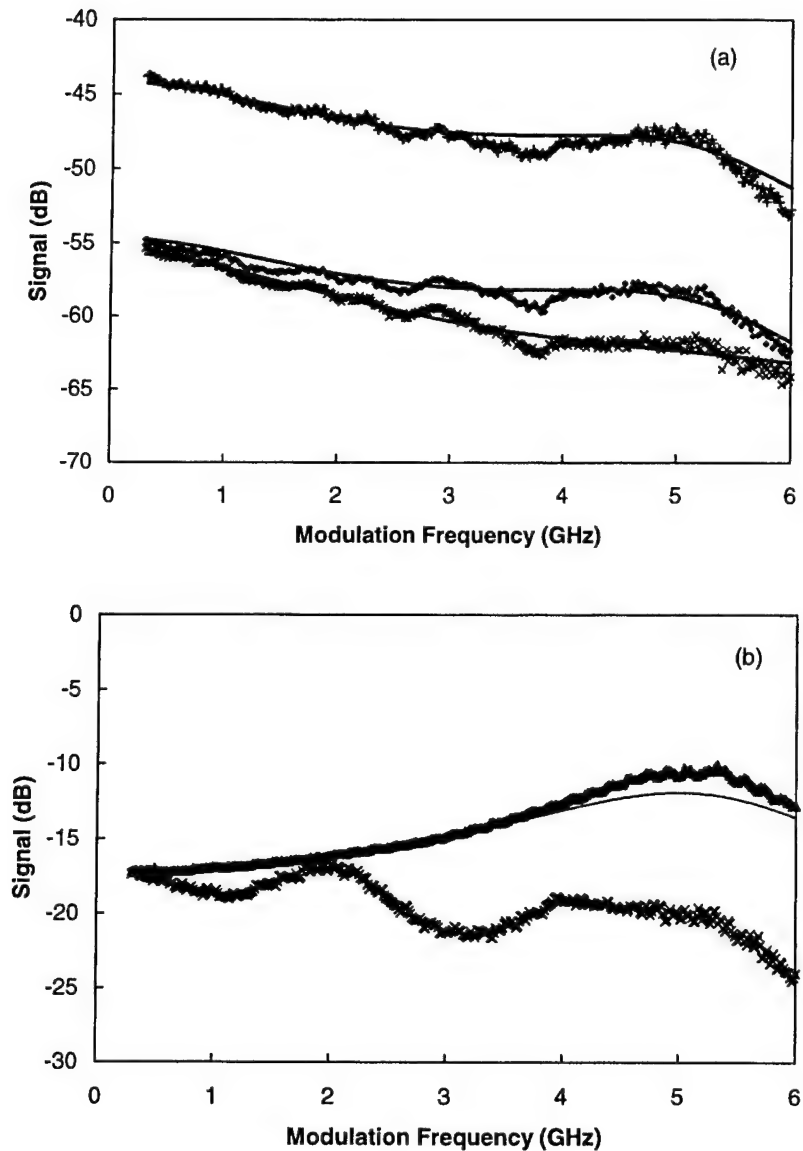


Figure 79. Calibration curves used for the modulation spectra. In (a), there are three sets of data and associated model curves of the photodetected signal from the free running lasers under current modulation. The top curve is for the free-running slave and the bottom two curves are the modulated output of the master laser at two different bias currents. The model curves take into account a simple RC-rolloff due to circuit parasitics. In (b), the bottom data set is the raw data from the network analyzer for the slave laser under optical injection at a resonance frequency of 15 GHz. Using the deviation of the free-running data from the calculated curves, as in (a), an overall circuit parasitic response is calculated and taken out of the data. The resulting data, upper set, is similar to the parasitic-free calculated curve for the free-running laser, also shown.

With this data correction procedure, Figures 80 and 81 show the different modulation response spectra as the strength of the injected optical signal is changed and different resonance frequencies are generated. The corrected 15 GHz spectra is repeated in Figure 80 from Figure 79(b), the calculated free-running spectra is repeated in both Figures 80 and 81 and the spectra corresponding to the resonance at approximately 11 GHz is also shown in both figures. As the injected optical signal is reduced, the locked resonance frequency decreases. Simultaneously, the optical spectra show a period-doubling feature which increases in amplitude with decreasing injection until it reaches a maximum at a locked resonance frequency of approximately 9 GHz. The spectrum associated with the 7-GHz resonance corresponds to the limit-cycle operating point just above the region of chaotic dynamics.

The optical spectra of Figures 78(a) and (b) and the 14 GHz modulation spectra are taken at approximately the same operating point. The modulation spectra consist of the sum of the beat signals between the main peaks and their respective sidebands. With optical injection to the slave, the dominant contribution to the signal is from the injected-shifted resonance peak and its two sidebands. Several interesting features are evident in the spectra. First, the period-doubling feature is clearly evident in the signal modulation spectra. The nonlinear dynamics has a strong influence on the signal modulation characteristics. Second, the period-doubling feature notwithstanding, there is very little variation in the response for frequencies below 2.5 GHz, except at the weakest optical injection level. This suggests that signal modulations with bandwidths up to 2.5 GHz can be placed on a variety of microwave subcarriers. More work will be required to substantiate this point, however.

When the signal modulation from the network analyzer is added to the master laser current bias, the modulation spectra are quite different. Using the optical spectra in Figures 78(c)-(f) as a reference, it can be seen that the modulation spectra will result primarily from the beat signal between the feature at the optical injection frequency and its two sidebands. There was considerably more variation in this data across the entire modulation spectrum, and the variations between the different operating points do not correlate well with the expected resonance and sub-resonance frequencies. Additional work will be necessary to get qualitative understanding of these modulation spectra and to separate real variations from experimental artifacts.

The signal modulation spectra shown in Figures 79-81 represent baseband conditions, the beating of the modulation signals with their respective central peaks. Of great interest to the current program is the nature of the modulation signal on the microwave subcarrier. This requires a downconversion of the detected optical signal by mixing it with the reference frequency generated by the frequency synthesizer. The frequency synthesizer provides the locking microwave current modulation while the network analyzer adds the signal modulation over a frequency range up to 6 GHz. The detected signal from the photodetector is amplified and then split. One leg of the splitter is sent to either a spectrum analyzer or a sampling oscilloscope. The other leg is passed through a microwave mixer to down convert the modulation signal, using the frequency synthesizer output as a reference. The slave laser is phase locked to the synthesizer reference using a simple feedback loop to the master laser current supply. Ideally, this feedback loop allows the phase of the sub-carrier to be adjusted over a range of π , one-half cycle, though, as reported below, the ideal condition is not always met. In addition to providing the error signal

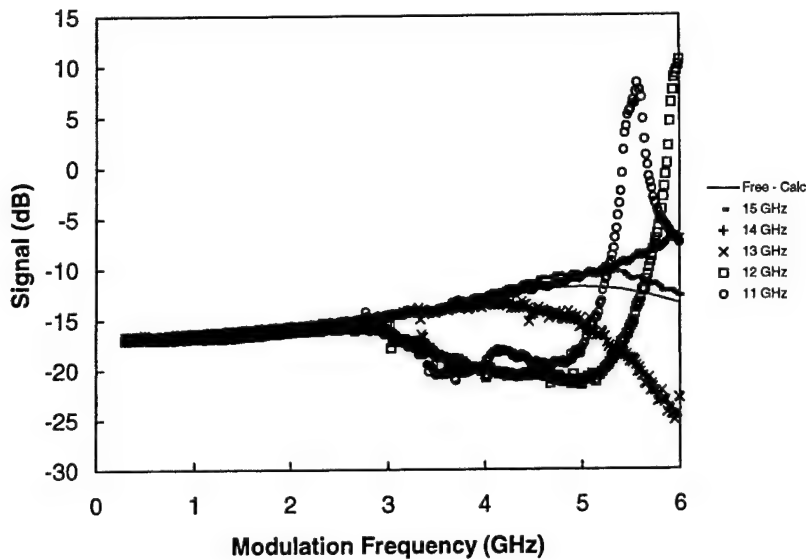


Figure 80. Network analyzer measurement of the photodetected signal component at the modulation frequency for several different operating points. The data is corrected for the parasitic losses of the electronic signal paths. Also shown for comparison is the calculated curve for the response of the free-running laser. The data is labeled by the resonance frequency with increasing frequency corresponding to increasing injected optical power from the master laser.

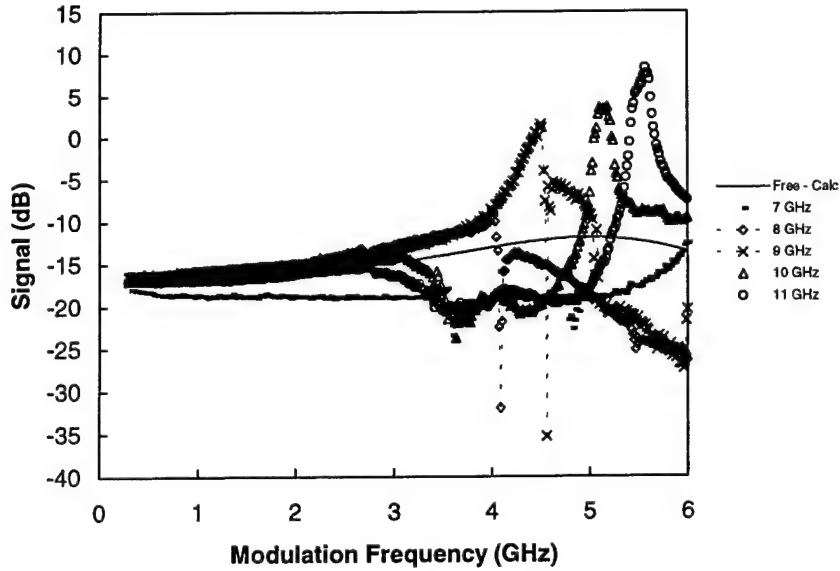


Figure 81. Network Analyzer measurement of the photodetected signal component at the modulation frequency for several different operating points at lower optical injection levels than in Figure 80. The strongest period doubling resonance optical spectrum occurs at approximately the 9 GHz locked resonance condition.

for the feedback loop, the output of the mixer also can be compared with the modulation signal using the network analyzer. In the results reported next, the slave laser was double locked with the frequency synthesizer and the modulation current from the network analyzer was added to the master laser.

An important reason for measuring the phase of the modulation signal is the interest in timing control. For the locked, microwave sub-carrier, phase shifts translate directly into time shifts. As we reported above, when the bias current to the master laser is swept, there can be a range where the reference signal from the synthesizer locks the dynamic resonance frequency of the slave laser. The voltage change that we measure as the bias current is swept through the locking range represents a phase, or timing, offset between the reference signal from the frequency synthesizer and the measured signal from the photodetector. Figure 82 shows the maximum time shift measured for the locked resonance frequency. The time shift corresponds to a phase shift of approximately 0.36π . We were never able to measure a full π -phase shift because of triggering problems associated with the sampling oscilloscope used to record the signals.

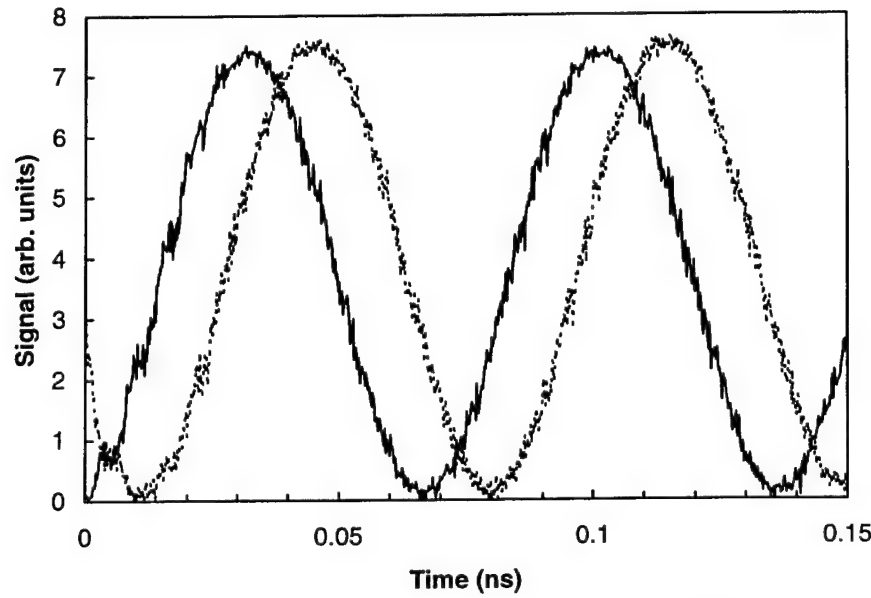


Figure 82. Maximum measured temporal shift of the 14.01 GHz sub-carrier.

If a broadband modulation signal is to be added to the sub-carrier reference, then a simple phase shift does not correspond to a time shift. To produce an equal time shift of all frequency components in a broadband signal, one must impose a linear phase shift. Such a phase shift occurs in the region of a resonance. Because the double-locked laser operates near the dynamic resonance of the optically injected slave laser, one can use the resonance imposed phase shift to produce the proper time-shifted characteristic. With a network analyzer one can measure the phase and amplitude changes. The network analyzer output is used to add a modulation to the locked resonance oscillation of the optical power. When the photodetected signal is down-converted at the microwave mixer, the output is the phase and amplitude shifted replica (with noise) of the network analyzer output. Feeding this signal back into the network analyzer allows

the spectrum of phase and amplitude changes to be measured as the slave laser is locked at different phase values relative to the sub-carrier reference.

The results for phase and amplitude are shown in Figures 83 and 84. Here, the frequency synthesizer was operated at 12.3 GHz and produced the sub-carrier reference. Shown in Figure 83 is the measured phase of the return signal to the network analyzer at one end of the locking range with the measured data given by the small squares and the dashed line giving a running average. The other five curves give the phase offset from this curve as the master laser current is adjusted across the locking region. The structure in the absolute curve includes the effects of all the elements in the electrooptic path. There is a roughly linear shift with frequency out to approximately 3 GHz, indicating that the resonance acts to control the timing of the signal. Figure 84 gives a similar record for the amplitude. Note that the amplitude spectra show considerably more variation but that there are reasonably steady amplitude characteristics over a wide intermediate frequency range.

The general variations in the phase between approximately 300 MHz and 2.5 GHz is consistent with a pi phase shift of the sub-carrier as the master laser is tuned across the double-locked operating condition. Therefore, there is a fairly broad bandwidth about the sub-carrier where timing control can be achieved. The variations of the amplitude characteristics show that there will be signal distortion.

The situation is different when the "information" signal is added to the slave laser instead of the master laser. Again, the frequency synthesizer provides the locking signal to establish double-locked operation. Because of the nonlinearities of the laser diode, the "information" signal is upconverted to become a modulation of the locking signal upon photodetection. The "information" signals are fed back to the network analyzer where phase and amplitude characteristics are measured. Data was taken with the double-locked laser diode operating with a dynamic resonance frequency of approximately 14 Ghz. Here, the laser is operating with limit cycle dynamics and the two dominant optical peaks are similar in amplitude. We found that there is an upper bound to the strength of the microwave signal that can be used to achieve double-locked operation. The upper signal level corresponded to a fractional modulation current $I_m/I_b \approx 0.26$. However, due to the parasitic capacitance of the laser, mount and cable, the actual current modulation seen by the laser gain region is reduced by an order of magnitude to about 3%. This is about a factor of 2-3 larger than the range of dc-bias currents that can sustain locked operation for a given optical input. When the modulation signal is larger, the optical and microwave spectra first starts to show a period doubling of the oscillatory nonlinear dynamics along with an increase in the level of the broadband noise, followed by an abrupt loss of locking. When the modulation signal is decreased, the range of dc currents where locking is sustained is reduced proportionately.

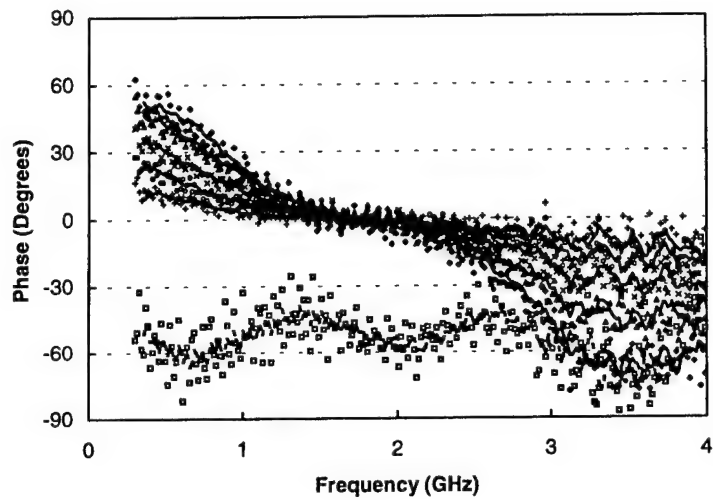


Figure 83. Network analyzer measurement of the phase of the photodetected signal component that is imposed on the sub-carrier and then demodulated at the mixer. The data is corrected for the parasitic losses of the electronic signal paths. The sub-carrier frequency is 12.3 GHz. The small squares are the absolute date, as measured by the network analyzer for data at one end of the locking range. The other curves are relative to this data and represent operating points as one crosses the range of injection-locked operation.

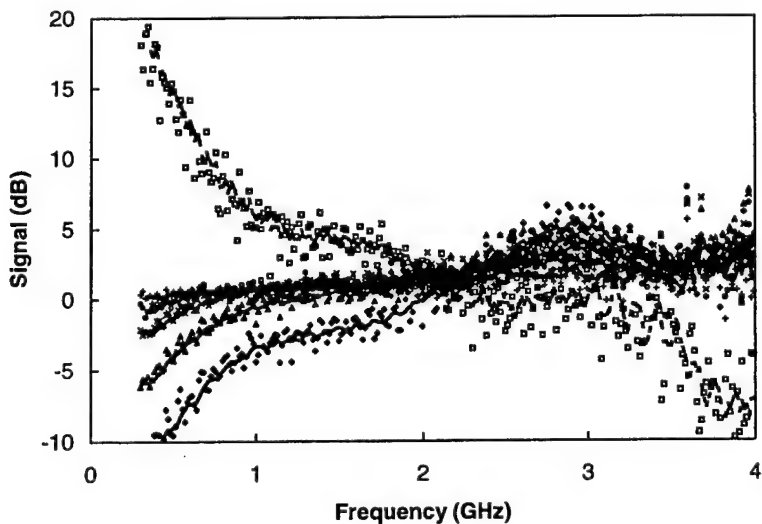


Figure 84. Network analyzer measurement of the amplitude of the photodetected signal component that is imposed on the sub-carrier and then demodulated at the mixer. The data is corrected for the parasitic losses of the electronic signal paths. The sub-carrier frequency is 12.3 GHz. The small squares are the absolute date, as measured by the network analyzer for data at one end of the locking range. The other curves are relative to this data and represent operating points as one crosses the range of injection-locked operation.

The key measurement for timing characteristics is the phase of the signal received at the network analyzer. Figure 85 gives the phase offset of the signal at either end of the locking range. However, the key point is that there is no linear variation of the slope with the frequency, a linear variation that changes as the operating point is moved across the locking range. This indicates that time delay cannot be imposed on broadband signals injected into the slave laser as they can for signals injected into the master laser. There is a phase delay on the microwave reference as the locking region is crossed, but the “information” signals do not experience the additional phase delay that is required for timing control of signals. Therefore, one must inject the “information” signal into the master laser to get the timing control.

We also attempted to determine the response characteristics of the double-locked laser when a high-speed digital modulation signal was used. The system was configured with a high-speed, up to 3.5 Gbit/s, data generator for the information input and a communications analyzer to record the photodetected signal. A combination of equipment problems and apparent limitations on the performance of our apparatus prevented us from taking useful quantitative measurements, though we were able to make some qualitative conclusions. First, the amplitude of the information signal is limited to a few percent modulation of the locked sub-carrier signal. Larger modulation caused the laser to become unlocked. Therefore, high-speed modulation of the locked microwave sub-carrier is limited to small signals. Our apparatus limited us further. The cable attenuation and dispersion, and the variations of gain with frequency of the microwave components distorted our signals so that it was difficult to determine the underlying response of the laser directly from the time traces.

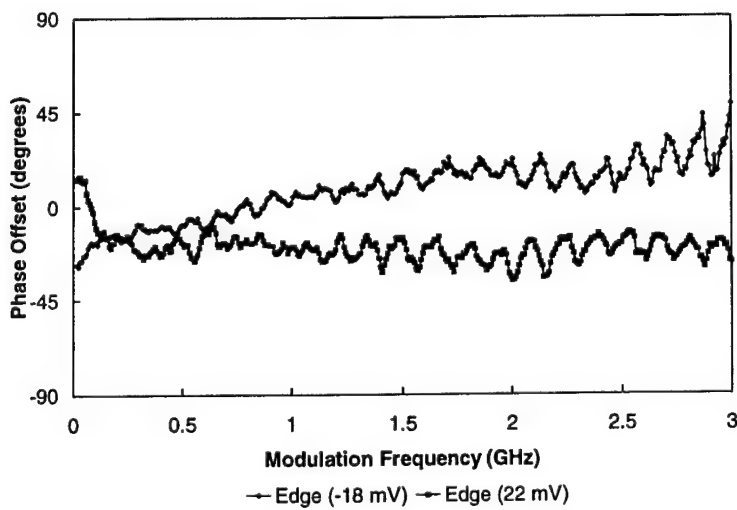


Figure 85. Phase of the received modulation signal, relative to the phase of the received signal when the laser is operated at the center of the locking range, at the two extrema of the locking range. The modulation signal is downconverted at a microwave mixer before measurement with the network analyzer.

D. Honeywell and MODE VCSELs

The data from the SDL lasers gave a fairly complete picture of the characteristics of the laser under double-locked operation. We then measured the output from the other lasers to compare with the performance of the SDL lasers. Emphasis was placed on the noise characteristics as these are of key interest in photonics applications. As we have pointed out earlier, the VCSELs are extremely sensitive to current and temperature fluctuations. The optical frequency of the Honeywell and MODE VCSELs shifted by on the order of -100 GHz/mA, most likely due to heating effects. The active area of the laser is so small that even small fluctuations can have a big effect. Because of this, the optical frequency of the VCSELs was not as stable as with the SDL edge emitters. In addition, the VCSEL arrays were not designed for high frequency current modulation. Even with the special packaging, the modulation characteristics were not as good as they were for the SDL lasers. For these reasons, the double locked operating characteristics were not as good.

Figure 86 shows the improvement in spectral characteristics of a double-locked Honeywell VCSEL. The narrowing of the spectral peak when the microwave modulation is added to the dc bias is apparent. Under double locked operation the carrier-to-noise ratio is approximately 100 dB/Hz, > 20 dB below the SDL lasers. Also, the increase in modulation amplitude is only

**Honeywell VCSEL - Carrier Frequency is 10.8 GHz
Resolution Bandwidth is 1 MHz**

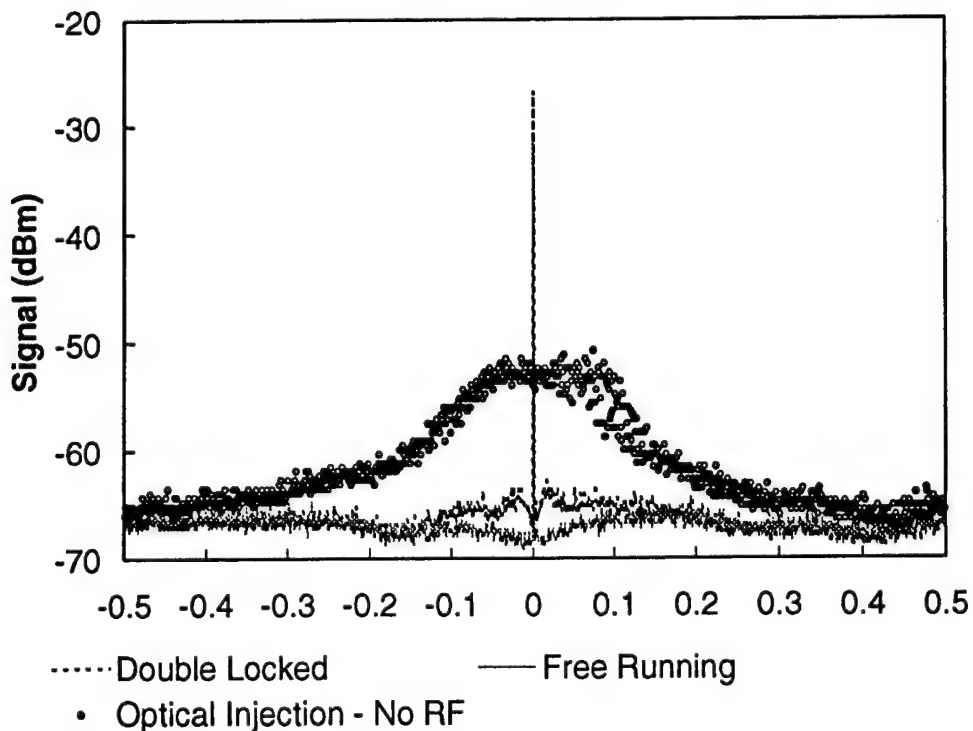


Figure 86. Microwave spectra of the Honeywell VCSEL, comparing the double-locked output with the free running output and the output under optical injection alone.

about 10 dB relative to the free-running laser to achieve this noise level. In part, the signal at the free running condition is large due to the fact that the relaxation resonance frequency approximately the same as the resonance frequency under optical injection. With the Honeywell VCSELs, the performance benefits under optical injection are relatively modest compared to the SDL lasers. In part this is due to the relatively poorer current modulation characteristics of the array packaging. The useful signal delivered to the gain medium is much reduced relative to the SDL lasers.

With the MODE VCSEL, a greater range of nonlinear dynamics is displayed and one observes a greater range of accessible resonance frequencies in the limit cycle regime. We investigated the phase noise characteristics using the phase noise test set. Figure 87 shows the observed absolute and residual phase noise characteristics of the double-locked MODE VCSEL and Figure 88 shows the locking characteristics measured with the spectrum analyzer. These should be compared with Figures 75 and 76. The absolute phase noise curve deviates from that of the frequency synthesizer for offset frequencies above approximately 1 kHz. Due to the sensitivity of the VCSEL to current noise and jitter, we could not use as high a loop gain with the OPLL as was possible with the SDL lasers. The residual phase noise curve should be compared to the residual phase noise curve taken with the lower OPLL loop gain in Figure 75. The VCSEL displays excess noise and the extra noise is clearly evident in the spectra measured by the spectrum analyzer.

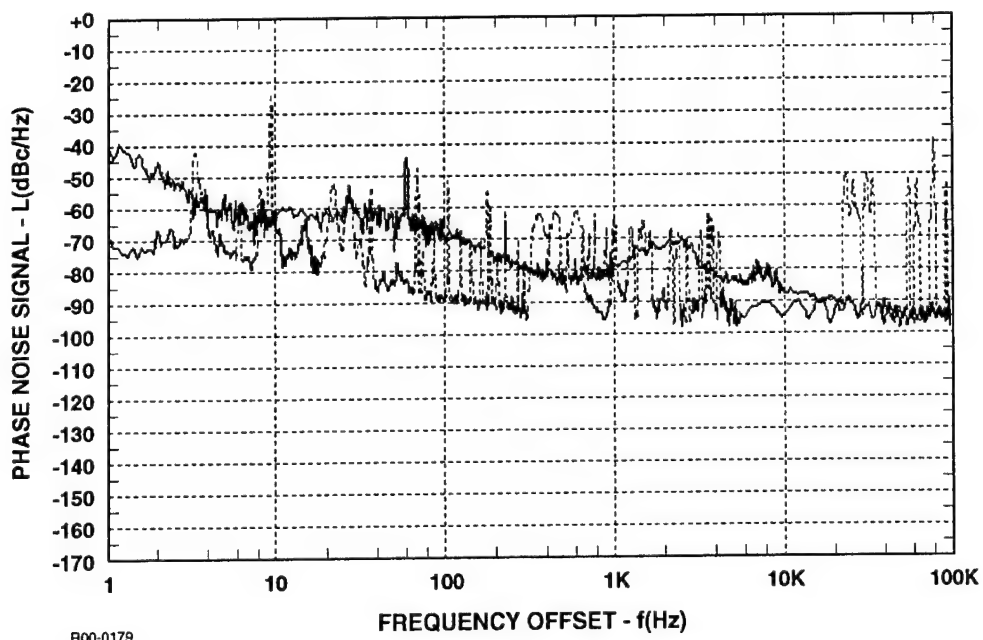


Figure 87. Phase noise of the photodetected signal of the optical output from the double locked laser diode. The upper curve is the absolute noise level. The lower curve is the residual phase noise.

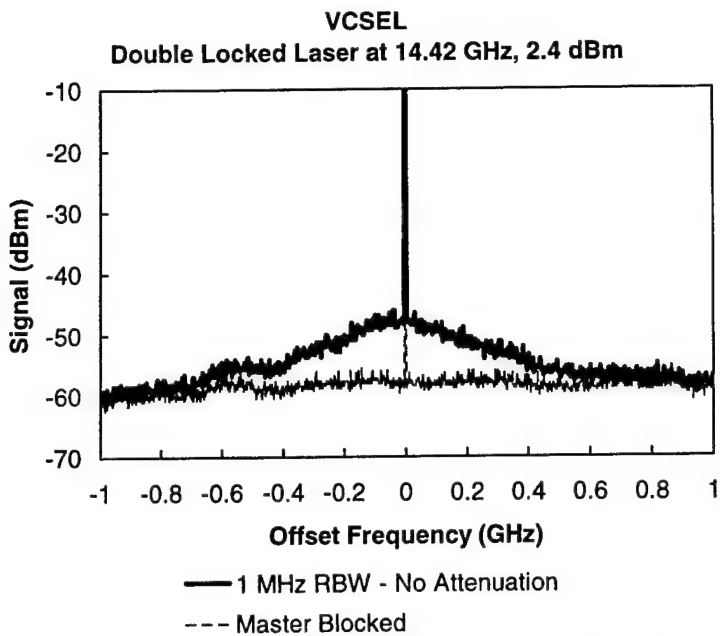


Figure 88. Microwave spectrum of the photodetected signal in the frequency region near the microwave carrier frequency of 14.42 GHz. The double locked laser and free running laser spectra are shown. The double-locked laser carrier signal is off-scale at 2.4 dBm. When the master laser is blocked, the free-running laser carrier signal is -30.4 dBm. The noise floor (master blocked) is higher in this measurement than in Figure 76 due to higher gain following the photodetector.

E. DFB Lasers – Compact Double-Locked Laser Implementation

To demonstrate that the double-locked configuration can be constructed in a compact package, using relatively inexpensive, commercially available optical components, we constructed a demonstration apparatus using DFB lasers. The packaged optical components are shown in Figure 89. Two Alcatel Model 1902 LMC DFB laser packaged in standard 5.6 mm transistor cans are used as the master and slave lasers. These lasers appeared to have similar characteristics to the Alcatel laser that was characterized in the fiber-coupled set-up. The lasers are used as they were commercially packaged, with the optical window that hermetically seals the package and transmits the laser output left in place. These lasers cost less than \$100 each. Both lasers are mounted with thermoelectric coolers. Wires for the laser bias and the thermoelectric cooler and temperature sensors can be seen on either side of the picture. The laser output is collimated by 5 mm AR coated barrel lens purchased from Edmund Scientific. The collimated master laser light passes through a micro-optical isolator. The laser and isolator are oriented so that they will be transmitted through a polarizing beamsplitter cube that acts as the coupling element. The cube face is 0.5 inch. A micro-Faraday rotator is placed between the slave laser collimating lens and the beamsplitter cube. The slave laser is oriented so that the light from the master laser will be transmitted to the slave laser but the output from the slave laser will be reflected at the polarizing beamsplitter and directed out in the direction of the camera taking the picture. Light was

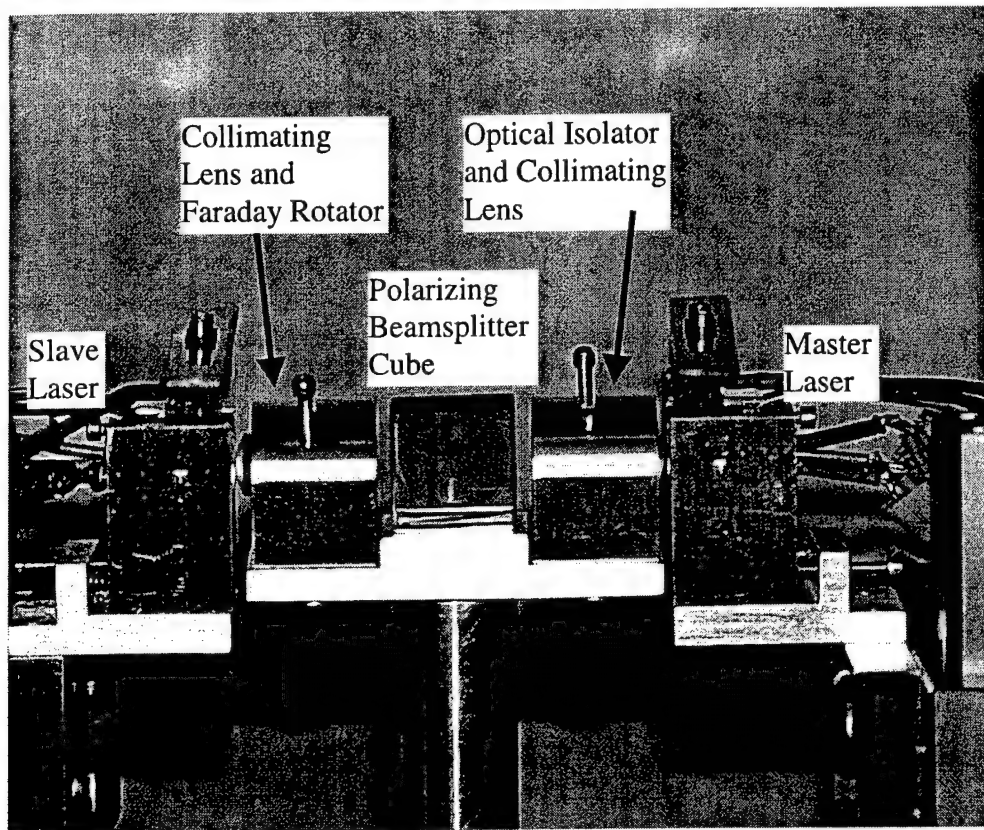


Figure 89. Compact demonstration package of the double locked laser using DFB lasers and miniature optical components available in the $1.55 \mu\text{m}$ spectral region. Scale of the device can be estimated by using the 0.5-inch side length of the face of the polarizing beamsplitter cube.

collected using a fiber-optic collimator, not shown, and routed to the fast photodetector. The seven optical components have a total cost of less than \$1200, with the optical isolator being the most expensive component. The train of elements occupies less than three inches along its optical axis.

Double locked operation was achieved using this configuration. Figure 90 shows the narrowing of the photodetector signal when the microwave reference is applied to the slave laser operating under optical injection and Figure 91 shows the best noise characteristics that we achieved. We wish to emphasize that we conducted only preliminary tests with this configuration and believe that better performance should be possible. These initial tests were merely meant to demonstrate the concept in this compact configuration. Noise levels are comparable with those measured with the VCSELs. Like the VCSELs, these DFB lasers are not packaged for high frequency current modulation and we simply coupled a piece of coaxial cable to the proper pins from the 5.6-mm can. Further work will be necessary to properly characterize the full capabilities of the DFB lasers in this configuration.

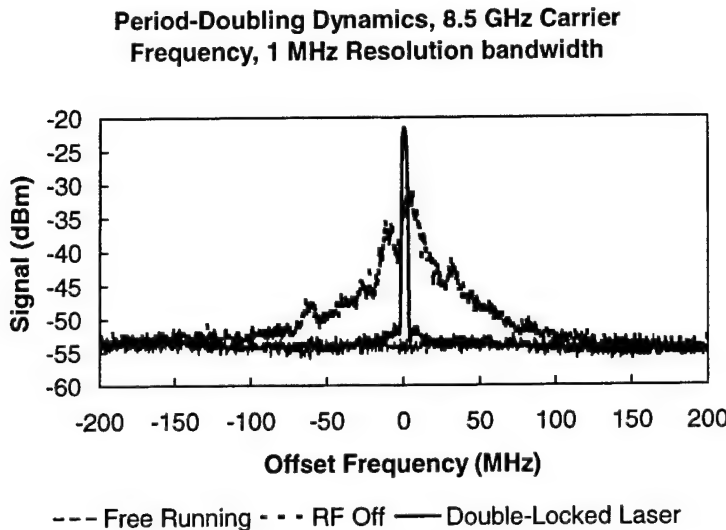


Figure 90. Noise characteristics of the compact, double-locked DFB laser configuration. The free-running curve gives the noise background. The RF off curve gives the photodetector signal spectrum near the resonance frequency when the laser is subject to optical injection. In this case the optical injection induces period-doubling dynamics with an 8.5 GHz resonance frequency. Adding the microwave reference double locks the laser, sharpening and enhancing the resonance signal.

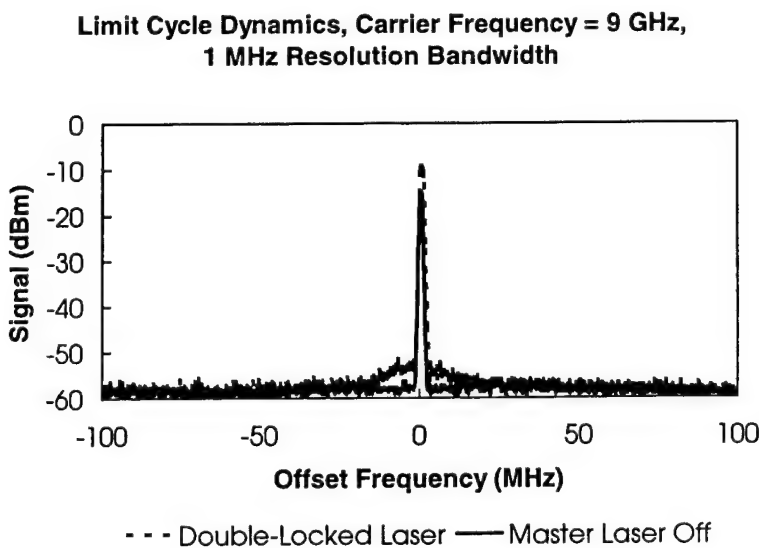


Figure 91. Resonance frequency signal of the compact, double-locked DFB laser configuration. The laser is now locked at an operating point with a 9 GHz resonance frequency and limit cycle dynamics. A strong microwave reference is used so that the modulation peak of the laser free of optical injection is only a few dB below the double-locked laser signal. Also, the double-locked laser displays a noise pedestal about the locked peak.

7. CONCLUSIONS

The nonlinear dynamics displayed by a semiconductor laser subject to external optical injection can be used to generate novel optical output characteristics that have RF photonics applications. In this program we have demonstrated how the model of the nonlinear interaction in semiconductor lasers can be improved to achieve excellent agreement with observed experimental data. We have also devised a new and simpler test for measuring the linewidth enhancement factor of a semiconductor laser. Further, we mapped out the different regions of nonlinear dynamics displayed by a semiconductor laser subject to external optical injection. Finally we have demonstrated a novel laser configuration, the double-locked laser diode, and performed a wide variety of tests on its operational capabilities.

We have demonstrated that a wide range of semiconductor lasers that operate in a single optical mode can be used to implement the double-locked laser. This configuration has excellent noise characteristics and can be implemented in a compact configuration. The noise characteristics compare favorably with other laser techniques used to generate a microwave and millimeter-wave sub-carrier. We have demonstrated double-locked performance over a wide range of microwave frequencies and have shown that high periodicity nonlinear dynamics can be used to lock the resonance frequency to a microwave reference that is a subharmonic.

Timing control of the microwave signal was demonstrated by using the change in phase of the locked signal as the locking range is scanned. Timing control of more complex signals was indicated by the phase characteristics of modulation signals added to the microwave carrier. However, the modulation signals could only be added to the master laser for the double-locked laser to show timing control. Further, the modulation signals must be limited to the small signal regime and the nonlinear interactions within the double-locked laser would tend to distort the transmitted signal. In general, the double-locked laser did not appear to have good broadband, i.e. GHz, modulation characteristics. Therefore, this technique will most likely have to be combined with another if it is to be used to carry wideband signals. For instance, the double-locked laser can be used to generate the sub-carrier and an external modulator can generate the "information" modulation. In this way, the requirements on the external modulator are reduced as it does not have to generate both the sub-carrier and the modulation signal. The applicability of such a configuration will depend on microwave/millimeter-wave system requirements. At this time, we have not been able to find a good match for the techniques that we have developed in this program and a military or civilian application.

In this program we have demonstrated that one should be aware that the linewidth enhancement factor, b , cannot, in general, be applied to the gain saturation terms of the coupled equation model. The gain saturation terms have a different proportionality factor between their imaginary and real parts, b' . This proportionality factor is not negligible, as it has sometimes been modeled, but usually of the same order of magnitude as the linewidth enhancement factor. The fact that $b' \neq b$ can be used to advantage to determine b , a parameter that is difficult to measure. When $b' \neq b$ there is an asymmetry of the

sidebands of the optical spectrum of a semiconductor laser under weak current modulation. This asymmetry has a distinct characteristic that depends only on b and not laser circuit parasitics that often mask the intrinsic laser characteristics. Therefore, one can determine b by observing the asymmetry as a function of modulation frequency even if the parasitics are strongly distorting the modulation response.

We have also shown that a simple modification of the coupled equation model, the addition of a nonresonant mode amplitude equation is sufficient to produce a qualitative understanding of the tendency of some semiconductor laser to undergo a mode hop under external optical injection. The nonlinear interactions within the semiconductor laser can cause an external signal to reduce the average output power from the free-running condition. This is accompanied by an increase in the average carrier density. This increase can be sufficient to overcome the gain defect of side modes and induce them to cross the laser threshold and become responsible for a significant fraction of the output power.

Using a new, fiber-coupled experimental configuration and DFB laser diodes, we have been able to fully map out the regions of nonlinear dynamics of a semiconductor laser subject to external optical injection. This mapping demonstrated that the periodic dynamics that are clearly evident in the optical spectra are special cases of a more general quasiperiodic interaction. The two key frequencies for this quasiperiodic interaction are the offset frequency between the injected optical signal and unlocked optical resonance frequency and the dynamic or relaxation resonance frequency. Both of these frequencies change with the strength of the optical injection. The optical spectra also showed evidence of multiple attractors for the laser, with the intrinsic laser noise causing the laser to sample more than one attractor at some operating points.

Two other points have shown themselves to be important for the optical injection configuration. Over the course of this research the VCSELs have displayed several characteristics that need to be addressed for optimal deployment. First, the small size of the VCSELs makes them susceptible to frequency jitter due to thermal fluctuations. These thermal fluctuations can arise directly due to changes in the environment, or they can arise from fluctuations in the bias current. The small mode volume of the VCSEL accounts for the temperature sensitivity. These effects will become more pronounced as even smaller devices are fabricated. Indeed, the Honeywell VCSELs that have 2- μm apertures showed greater sensitivity to current and temperature fluctuations than the 8- μm MODE VCSELs. Further, the arrays that have been studied in this program showed minor but significant device-to-device variations, particularly with respect to the emission wavelength in the case of the Honeywell VCSELs, but also the optical power vs. current characteristic and the variations of b' and b in the MODE VCSELs. The other point is the well-known sensitivity of semiconductor lasers to unwanted feedback. Even when there is a strong optical locking signal, the presence of optical feedback can significantly corrupt the output of the semiconductor laser. If a single master laser, for instance, is to be used to inject multiple slave lasers, then there must still be excellent optical isolation between the slave lasers. Further work is required to determine if the

novel capabilities that can be achieved with semiconductor laser subject to optical injection can meet performance requirements of RF photonics applications.

REFERENCES

- 1) T.B. Simpson, J.M. Liu and A. Gavrielides, *IEEE J. Quantum Electron.* **32**, 1456 (1996).
- 2) T.B. Simpson and J.M. Liu, *IEEE Photonics Technol. Lett.* **9**, 1322 (1997).
- 3) T.B. Simpson, J.M. Liu, K.F. Huang and K. Tai, *Quantum and Semiclassical Optics* **9**, 765 (1997).
- 4) J. Sacher, D. Baums, P. Panknin, W. Elsässer, and E.O. Göbel, *Physical Review A* **45**, 1893 (1992).
- 5) T.B. Simpson and F. Doft, *IEEE Photon. Technol. Lett.*, vol. 11, pp. 1476-1478 (1999).
- 6) T.B. Simpson, *Opt. Commun.* **170**, 93 (1999).
- 7) J.M. Liu and T.B. Simpson, *IEEE J. Quantum. Electron.* **30**, 957 (1994).
- 8) G.P. Agrawal, *IEEE J. Quantum Electron.* **9**, 1901 (1990).
- 9) W.H. Press, S. A. Teukolsky, W.T. Vetterling and B.P. Flannery, *Numerical Recipes in FORTRAN* (2nd Ed.), Cambridge University Press, 1992.
- 10) T.L. Riggs and C.L. Phillips, *Simulation* **48**, 11 (1987).
- 11) E. Helfand, Bell Labs. Tech. J. **58**, 2289 (1979), and H.S. Greenside and E. Helfand, *Bell Labs. Tech. J.* **60**, 1927 (1981).
- 12) T.B. Simpson, J.M. Liu and A. Gavrielides, *IEEE Photonics Technol. Lett.* **7**, 709 (1995).
- 13) B. Li, W. Sha, S. Yeh, R. Nagarajan, and R.R. Craig, *Proc. SPIE* **3266**, 49 (1998).
- 14) S. Jiang, M. Dagenais, and R.A. Morgan, *Appl. Phys. Lett.* **65**, 1334 (1994).
- 15) J. Foresi, MODE Inc., private communication.
- 16) J.M.T. Thompson and H.B. Stewart, *Nonlinear Dynamics and Chaos*, John Wiley and Sons, 1986.
- 17) T.B. Simpson, J.M. Liu, A. Gavrielides, V. Kovaris and P.M. Alsing, *Phys. Rev A* **51**, 4181 (1995).
- 18) C. Walton, A.C. Bordonalli, and A.J. Seeds, *IEEE Photon. Technol. Lett.* **10**, 427 (1998).
- 19) L. Goldberg, H.F. Taylor, J.F. Weller, and D.M. Bloom, *Electron. Lett.*, **19**, 491 (1983).
- 20) Z.F. Fan, P.J.S. Heim, and M. Dagenais, *IEEE Photon. Technol. Lett.*, **10**, 719 (1998).
- 21) C. Laperle, M. Svilans, M. Poirier, and M. Têtu, *IEEE Trans. Microwave Theory Techniques* **47**, 1219 (1999).
- 22) Alcatel has announced that a two-section DFB laser will soon be available. It has been developed as a tunable source for wavelength division multiplexing applications.
- 23) U. Gliese, T.N. Nielson, M. Brunn, E.L. Christensen, K.E. Stubkjaer, S. Lindgren, and B. Broberg, *IEEE Photon. Technol. Lett.* **4**, 936 (1992).
- 24) A.C. Davidson, F.W. Wise, and R.C. Compton, *IEEE Photon. Technol. Lett.* **10**, 1304 (1998).